STUDIA UNIVERSITATIS
BABEŞ-BOLYAI

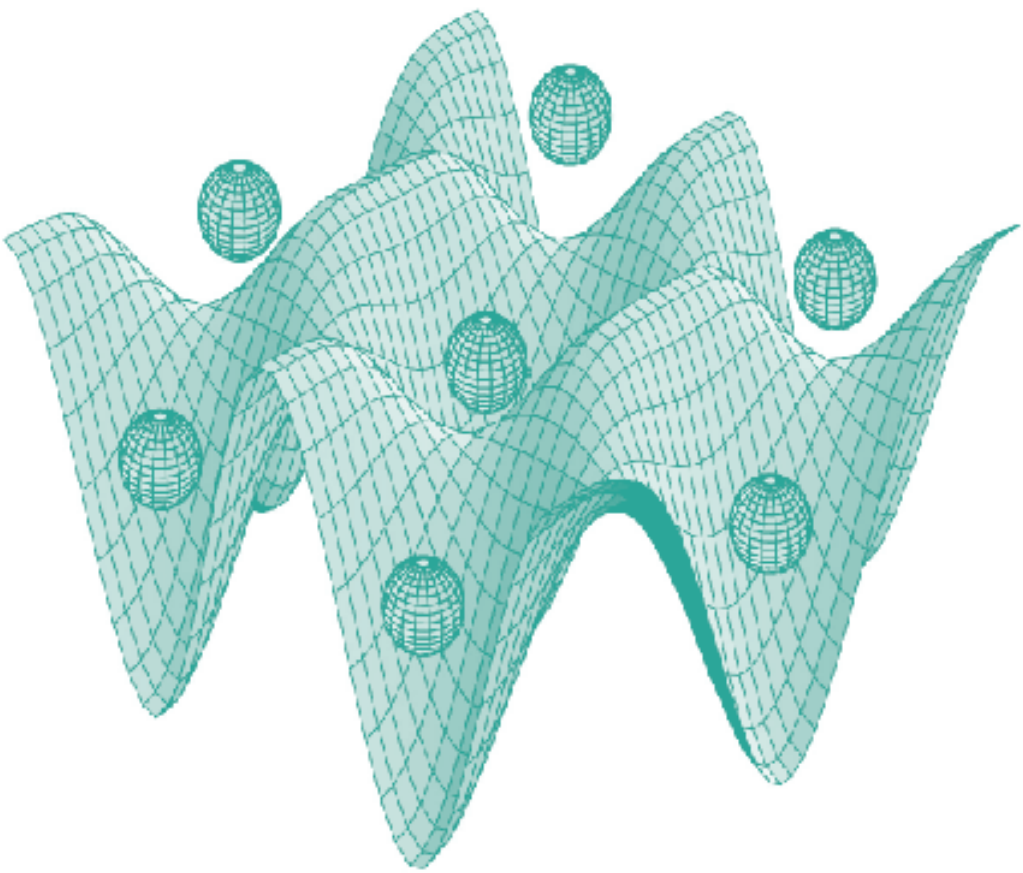

PHYSICA

1/2014

STUDIA
UNIVERSITATIS BABEŞ-BOLYAI
PHYSICA

1/2014

June

EDITORIAL OFFICE OF STUDIA UBB PYSICA:
1, M. Kogălniceanu St., Cluj-Napoca, ROMANIA, Phone: +40 264 405300
http://www.studia.ubbcluj.ro/serii/physica/index_en.html

YEAR **Volume 59 (LIX) 2014**
MONTH **JUNE**
ISSUE **1**

S T U D I A
UNIVERSITATIS BABEŞ–BOLYAI

PHYSICA

1

DEDICATED TO PROFESSOR VASILE CRISAN ON HIS 65th ANNIVERSARY

STUDIA UBB EDITORIAL OFFICE: B.P. Hasdeu no. 51, 400371 Cluj-Napoca, Romania,
Phone + 40 264 405352

CUPRINS – CONTENT – SOMMAIRE – INHALT

AUREL POP, *Foreword* 5

D. BENEA, S. MICAN, M. COLDEA, V. POP, Magnetic Properties of the τ-Phase of MnAl Alloy Doped with Zn 7

VOICU POPESCU, ALEX ZUNGER, Alloy Microstructure as Reflected by the Effective Band Structure: Partially Ordered In0.5Ga0.5P and In0.5Ga0.5As 13

R. DUDRIC, C. HIMCINSCHI, C. RUSU, I. GR. DEAC, R. TETEAN, Electronic Structure and Magnetic Properties and of $La_{1.2}Nd_{0.2}Ca_{1.6}Mn_2O_7$ and $La_{1.2}Sm_{0.2}Ca_{1.6}Mn_2O_7$ Compounds 31

I. GROSU, Conductance of a Quantum Wire-Side-Coupled-Quantum Dot System 39

M. POP, D. FRUNZA, A.V. POP, Numerical Investigations on Influence of Die Geometry and Ram Speed on the Hot Extrusion of Aluminium Alloy 47

AMIR JAVAD AHRAR, MOHAMAD HASSAN DJAVARESHKIAN, VALI KALANTAR, Investigation of Handmade Ferrofluids' Motion in a Ventilated Cavity Using Computational Fluid Dynamics 59

Ş. ONȚANU-CRĂCIUN, A. MARCU, N. MAGYAR**,** Macroscopic Analysis of the Interiors of Two Neutron Stars 73

S. MICAN, R. C. GAVREA, B. V. NEAMȚU, M. COLDEA, V. POP, Structural and Magnetic Properties of the $Mn_{50}Al_{46}Ni_4$ Alloy 83

GHEORGHIEŞ OANA, LIVIU DĂRĂBAN, Measurement of Thermal Neutron Cross-Section for the $^{174}Yb(n, \gamma)^{175}Yb$ Nuclear Reaction by Using Isotopic Neutron Source 91

STUDIA UBB PHYSICA, Vol. 59 (LIX), 1, 2014, pp. 5-6
(RECOMMENDED CITATION)

FOREWORD

Professor *Vasile Crișan* was born in 1949, February 2, Cluj-Napoca.

He graduated Babeș-Bolyai University Cluj-Napoca in 1972. Between 1972-1990 he worked as assistant professor at Faculty of Physics.

Since 1990 Prof. Crișan worked at Babes-Bolyai University first as associate professor (1990-1996) and later as professor (1996-present) at Department of Condensed Matter Physics and Advanced Technologies.

He held also administrative positions as Dean of the Faculty of Physics and Head of Department.

Prof. Vasile Crișan earned his PhD in Physics with the "Elementary excitations in magnetic solid", in 1972, under the guidance of Prof. Iuliu Pop. In the PhD thesis, the characterization of complex intermetallic compounds was done, in terms of electronic structure calculation by using an original program based on plane wave method associated (APW) and also through a scheme interpolation. Some of the topics addressed in the thesis were initiated during an internship specialization in Amsterdam, in the between 1974 - 1975 under the leadership of Prof. Dr. PF Chatel.

From 01.02.1997 until 1.2.2002 prof. V. Crișan worked in Germany at University Ludwig Maximilian in Munich with Prof. Dr. Hubert Eberth and Gerhard Mercator, and in Duisburg with Prof. Enthel, as visiting researcher.

The scientific activities of Prof. V. Crișan were focused on:

a) Experimental research and modeling of the crystal structure of intermetallic compounds and alloys with rare earth transition metals.

b) Theoretical Research on the properties of compounds and alloys by calculating the electronic structure at T = 0 K and at finite temperatures.

Prof. Vasile Crișan obtained significant scientific results concerning synthesis of materials, physical properties of new materials, the nature of magnetic interactions, local environment effects, the connection between local structure and magnetic properties, spin and ordered structures in glasses and ceramics.

Prof. V. Crișan scientific results were published in 50 papers, 25 in ISI quoted journals.

Around 40 papers were published in Proceeding of International Conferences. The scientific results of Prof. V. Crișan are frequently cited in literature, particularly for their rigorous presentation of new results related to the band structure of magnetic materials.

The main scientific results are:

• Calculation of magnetic properties of compounds of type intermetatlici R_2 (MM ') _5 by using an original computer program based on recursive method;

• Calculation of magnetic properties of intermetallic compounds such R_2 (MM ') _17 using the method TB - LMTO where M is the transition metal and M ' Si or Al.

• Calculation of the electronic structure of surfaces with application to Ni;

• Calculating correlation function shape memory alloys with application to the ternary alloy Cu-Zn-Al;

• Calculating the density of states of 123 and 214 high-temperature supraconductors;

• Evaluating the short distance in order FeNi alloys on the magnetic properties and thermal ab-initio calculations KKR-CPA;

• Study of metal semiconductor interface-zero temperatures by molecular dynamics method based on the application interface pseudopotentialului Fe / GaAs (001).

By understanding the importance of modern directions in material science, Prof. V. Crișan introduced new courses, related to modern methods in the study of solid state physics. His theoretical and experimental researches, as well as his pedagogic experience were fructified into a series of books focusing on physical properties of solid state. Professor V. Crișan published also two scientific books ("The calculation of energy bands in solid state" and "Jawa Script") and seven book frequently used by the students. These are remarkable for their accuracy and scientific level.

Professor V. Crisan was member of Romanian Physical Society, Romanian Society of Magnetic Materials, European Physical Society, Balkan Physical Society and International Society of Crystallography.

Professor V. Crișan was member of the Editorial Board of Journal Studia-Physica University Babeș-Bolyai Cluj, and referee to a series of international scientific journals. He was invited to sustain plenary presentations at many national and international meetings and conferences.

Today, at the age of 65 years, prof.V.Crișan can be satisfied that the young researchers supervised by him at the Faculty of Physics, continues his scientific research at the Babes-Bolyai University and in prestigious research institutes from Europe and United States of America.

Prof.dr. Aurel Pop
Dean, Faculty of Physics

STUDIA UBB PHYSICA, Vol. 59 (LIX), 1, 2014, pp. 7-12
(RECOMMENDED CITATION)

MAGNETIC PROPERTIES OF THE τ-PHASE OF MnAl ALLOY DOPED WITH Zn

D. BENEA[a*], S. MICAN[a], M. COLDEA[a] AND V. POP[a]

ABSTRACT. A detailed theoretical investigation on the electronic and magnetic properties of τ-phase of $Mn_{54}Al_{46}$ alloys with the CuAu tetragonal type of structure has been performed. All theoretical investigations of the electronic and magnetic properties have been done using the Korringa-Kohn-Rostoker (KKR) band structure method. The disorder in the system has been accounted for by means of the Coherent Potential Approximation (CPA). The spin resolved density of states (DOS) reflects the covalent nature of the interatomic bands. The calculated magnetic moments for the system $Mn_{54-x}Al_{46}Zn_x$ show a non-linear variation with Zn content ranging between 4.06 μ_B/unit cell for $Mn_{54}Al_{46}$ (x = 0) to 4.68 μ_B /unit cell for $Mn_{50}Al_{46}Zn_4$ (x = 4), suggesting an optimum Zn doping of 4% for Mn, close to the value of 2.9 % determined by experiment. On the other side, the SPR-KKR calculations do not confirm the existence of an optimum Zn for Al substitution which maximizes the magnetic moment of the samples.

Keywords: *band structure calculations, magnetic moments, density of states*

INTRODUCTION

The ferromagnetic τ-phase of the MnAl alloy, which has been first reported by Kono [1] and Koch et al. [2], attracted much attention in the field of high performance magnets, due to its high magnetic performance, low cost and low density (5.3 g/cmc). Despite the fact that Mn and Al are not ferromagnetic, the metastable tetragonal τ-phase with the composition $Mn_{54}Al_{46}$ at which the eutectoid transformation occurs at 870 ºC, can be obtained with high remanence, coercivity and saturation magnetization [3]. The magnetic moment for MnAl τ-phase is 2.4 μ_B /f.u. [4] and the Curie temperature is 382 ºC [5], which is higher than the T_C of $Nd_2Fe_{14}B$ (314 ºC).

[a] *Babes-Bolyai University, Faculty of Physics, 400084 Cluj-Napoca, Romania*
** Corresponding author email: diana.benea@phys.ubbcluj.ro*

Park et al. [6] obtained by theoretical first principle calculations for MnAl τ-phase values of magnetic moment and magnetocrystalline anisotropy of 2.37 μ_B / f.u. and 0.259 meV/f.u., respectively. The experimentally reported saturation of magnetization of the τ-phase of MnAl alloy is 89 emu/g, lower than the calculated value of 144 emu/g. Also, the experimentally determined value of energetic product is 4.7 MGOe, lower than the estimated theoretical value of 12.64 MGOe [6].

As the τ-phase of MnAl is metastable, pure phase can be produced only by rapid quenched of high temperature ε-phase, followed by isothermal annealing [5]. Long time annealing would produce the decomposition of τ-phase into the equilibrium γ and β phases. In order to stabilize the τ-phase, doping with several elements (Ti, Ni, Cu, C, B) has been reported [8]. The effect of Zn substitution on the structural and magnetic properties of τ-phase of MnAl has been investigated by Wang et al. [7]. They found that Zn substitution can stabilize the τ-phase, increase the coercivity and saturation magnetization but reduces the Curie temperature. The optimal magnetic performances of the Zn doped MnAl (τ-phase) was found for 2.9 % Zn for Mn and 3.7 % Zn for Al, respectively.

To evaluate the influence of Zn substitution on the electronic and magnetic properties of $Mn_{54}Al_{46}$ τ-phase, we performed electronic band structure calculations for $Mn_{54-x}Al_{42+x}Zn_4$ (x = 0, 2, 4, 6) and $Mn_{54-y}Al_{46}Zn_y$ (y=0, 2, 4, 6) alloys and we correlated the results with the experimental measurements. The variation of magnetic moments with Zn content, together with the preferential substitution of Zn on a certain crystal site is discussed.

COMPUTATIONAL DETAILS

The electronic structure of the τ-phase of $Mn_{54}Al_{46}$ alloy doped with Zn was calculated self-consistently by means of the spin polarized scalar relativistic Korringa-Kohn-Rostoker (KKR) method in the atomic sphere approximation (ASA) mode [9]. The calculation method is based on the KKR-Green's function formalism that makes use of multiple scattering theory. The local spin density approximation (LSDA) for the exchange-correlation energy using the Vosko, Wilk and Nusair (VWN) parameterization was used [10]. The disorder in the system has been accounted by means of the Coherent Potential Approximation (CPA) [11].

RESULTS AND DISCUSSIONS

The fully relativistic KKR band structure calculations have been performed for $Mn_{54-x}Al_{42+x}Zn_4$ (x = 0, 2, 4, 6) and $Mn_{54-y}Al_{46}Zn_y$ (y = 0, 2, 4, 6) alloys in CuAu type of

structure, using the experimental lattice constants of $Mn_{54}Al_{46}$ (a = 3.94 Å, c = 3.58 Å) determined by Kono et al. [1]. The τ- phase structure of Mn-Al alloy used for these calculations is presented in Fig. 1.

The base plane denoted as layer (1) is occupied with Mn (1) 8% and Al (1) 92% atoms, whilst the layer (2), at distance of 0.5 *c* is occupied with Mn (2) atoms (100 %), this tetragonal planar structure stacking alternately in [001] direction of crystal. The nearest neighbors of Mn from two adjacent layers have the distance 2.66 Å, whilst the distance between Mn atoms in the Mn layer is 2.79 Å, higher than the critical value for occurrence of ferromagnetism between Mn atoms (2.57 Å) as derived from the Bethe-Slater curve [1].

The KKR band structure calculations have been performed for $Mn_{54}Al_{46}$ alloy considering the Mn atoms from different layers ferromagnetically and antiferromagnetically coupled, respectively.

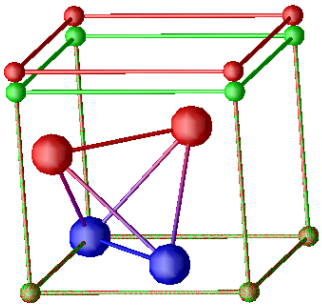

Fig. 1. The τ- phase structure of Mn-Al alloy.
Blue: Al atoms in the base plane. Red: Mn atoms at *0.5c*.

The total energy calculations show that the antiferromagnetic coupling of Mn spins is energetically favored, in agreement with experimental measurements [2]. Consequently, the further discussions on Zn doped $Mn_{54}Al_{46}$ alloys are done considering an antiferromagnetic spin configuration for Mn spins.

By doping with 3d elements into the $Mn_{54}Al_{46}$ alloy, the dopant atoms can substitute into the layer (1) populated by Mn(1) and Al or into the layer (2), populated only by Mn(2). In order to investigate the preferential substitution with Zn atoms, total energy calculation have been performed for the structure denoted as $(Al_{46}Zn_{4-\delta}Mn_{\delta})^1(Mn_{50-\delta}Zn_{\delta})^2$, where (1) and (2) stands for layer type and δ represents the percentage of Zn substituting the Mn from the layer (2). The results of total energy calculations are shown in Fig. 2. According to this calculation, the Zn substitution into the layer (2) is energetically unfavorable. As a conclusion, by Zn addition into the $Mn_{54}Al_{46}$ alloy the Zn atoms would substitute the Mn(1)/Al(1) atoms from the layer (1).

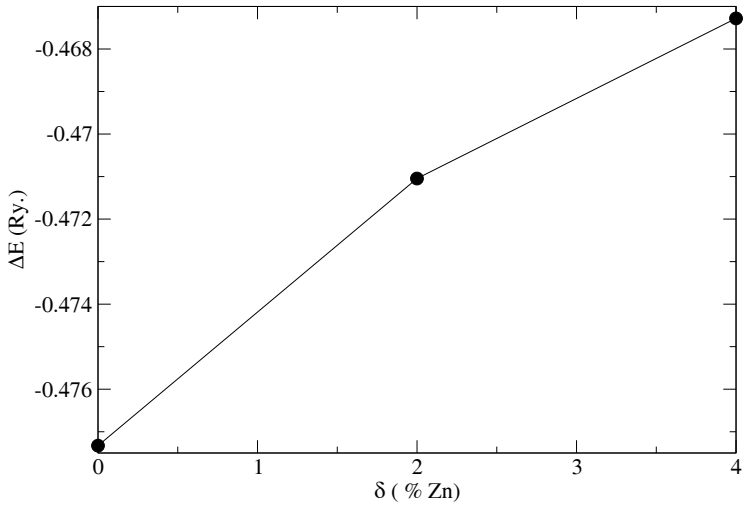

Fig. 2. Total energy calculations of $(Al_{46}Zn_{4-\delta}Mn_{\delta})^{1}(Mn_{50-\delta}Zn_{\delta})^{2}$, where (1) and (2) stands for layer type and δ represents the percentage of Zn substituting the Mn from layer (2).

The magnetic moments (in μ_B) for the $Mn_{54}Al_{46-x}Zn_x$ (x = 0, 2, 4, 6) alloys in antiferromagnetic spin configuration are presented in Table 1. The total magnetic moment is calculated per unit cell, including four atoms (see Fig. 1). As can be seen in Table 1, the Zn for Al substitution in $Mn_{54}Al_{46-x}Zn_x$ alloys is beneficial for the magnetization, the total magnetic moment per unit cell increasing with Zn content. We notice a slight decrease of the Mn(1) spin magnetic moment with Zn content (from 3.17 μ_B for undoped sample to 3.11 μ_B for x = 6), whilst the Mn(2) magnetic moment is increasing from 2.35 μ_B (x = 0) to 2.47 μ_B (x = 6). From our SPR-KKR calculations there is no clear evidence of a certain Zn for Al doping (in the range x = 0 – 6) which would maximize the magnetization of the $Mn_{54}Al_{46-x}Zn_x$ alloys.

Table 1.

The magnetic moments (in μ_B) for the $Mn_{54}Al_{46-x}Zn_x$ (y = 0, 2, 4, 6) alloys in antiferromagnetic spin configuration.

x	Al (1)		Zn (1)		Mn(1)		Mn(2)		Total(μ_B/cell)	
	m_s	m_l	m_s	m_l	m_s	m_l	m_s	m_l	m_s	m_l
0	-.07	0	-	-	-3.17	-	2.35	0.04	4.06	0.08
2	-.08	0	-.04	0	-3.12	-.01	2.41	0.04	4.20	0.08
4	-.08	0	-.04	0	-3.12	-.01	2.44	0.04	4.24	0.08
6	-.08	0	-.04	0	-3.11	-.01	2.47	0.04	4.30	0.08

The magnetic moments (in μ_B) for the $Mn_{54-y}Al_{46}Zn_y$ (y=0, 2, 4, 6) alloys in the antiferromagnetic spin configuration are presented in Table 2.

As can be seen in Table 2, the Zn for Mn substitution is increasing the total magnetic moment per unit cell of the samples with about 10% for an optimum doping of 4% Zn for Mn. The SPR-KKR calculations confirm the existence of an optimum Zn for Mn substitution, the value deduced from our calculations being higher than the experimentally determined doping of 2.9 % Zn.

Table 2.

The magnetic moments (in μ_B) for the $Mn_{54-y}Al_{46}Zn_y$ (y = 0, 2, 4) alloys in antiferromagnetic spin configuration.

Y	Al (1)		Zn (1)		Mn(1)		Mn(2)		Zn (2)		Total(μ_B/cell)	
	m_s	m_l	m_s	m_l	m_s	m_l	m_s	m_l	m_s	m_l	m_s	m_l
0	-.07	0	-	-	-3.17	0	2.35	0.04	-	-	4.06	0.08
2	-.08	0	-.04	0	-3.13	0	2.43	0.04	-	-	4.46	0.08
4	-.08	0	-.04	0	-	-	2.42	0.04	-	-	4.68	0.08
6	-.09	0	-.04	0	-	-	2.43	0.04	-.03	0	4.50	0.08

The density of states (DOS) calculations for the $Mn_{54}Al_{46}$ and $Mn_{50}Al_{46}Zn_4$ alloys reflects the covalent nature of the interatomic bands. As can be seen in Fig. 2,

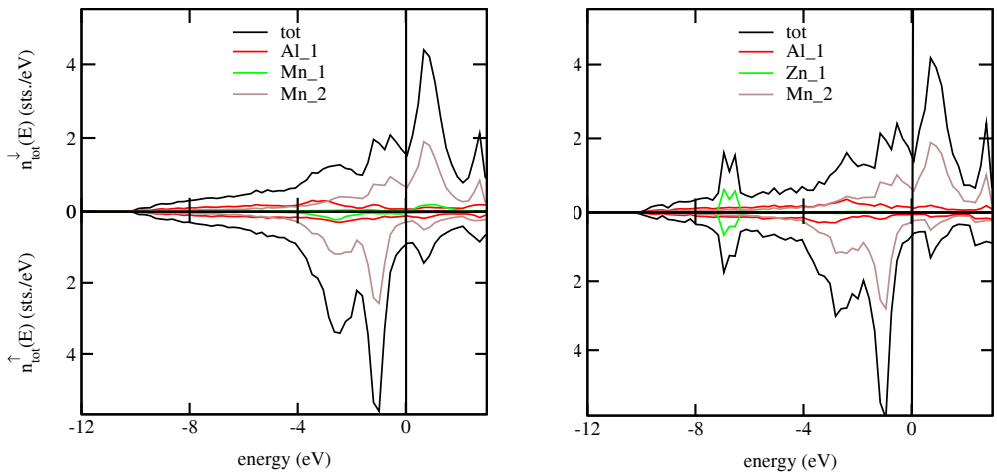

Fig. 2. Density of states calculated for $Mn_{54}Al_{46}$ alloy (left) and $Mn_{50}Al_{46}Zn_4$ alloy (right). The Fermi energy is the origin of the energy scale.

No significant modification for DOS of Mn (2) is observed by Zn for Mn substitution in $Mn_{54}Al_{46}$. The DOS calculation takes into account the preferential substitution of Zn for Mn (1) sites. A significant peak (at -7 eV) is observed in the DOS of $Mn_{50}Al_{46}Zn_4$ stemming from Zn.

CONCLUSIONS

SPR-KKR band structure calculations have been performed for τ-phase of $Mn_{54}Al_{46}$ alloy in CuAu structure type. The total energy calculations show a preferential occupation by Zn substitution for basal plane on the unit cell, denoted as layer (1), occupied with Mn(1) and Al(1) atoms in the undoped alloy. The calculated magnetic moments for the system $Mn_{54-x}Al_{46}Zn_x$ suggest an optimum doping of 4% Zn for Mn, close to the value of 2.9 % determined by experiment [7]. Also, the SPR-KKR calculations do not confirm the existence of an optimum Zn for Al substitution which maximizes the magnetic moment of the samples, as reported by experimental measurements [7].

ACKNOWLEDGEMENTS

The authors acknowledge the financial support of the UEFISCDI project PNII-ID-PCE-2012-4-0470.

REFERENCES

[1] H. Kono, J. Phys. Soc. Japan **13**, 1444 (1958).
[2] A.J.J. Koch et al, J. Appl. Phys. **31**, S75 (1960).
[3] T. Saito, J. Appl. Phys. **93** 8686 (2003).
[4] A. Sakuma, J. Phys. Soc. Jpn. **63** 1422 (1993).
[5] Q. Zeng, I. Baker, J.B. Cui and Z.C. Yan, J. Magn. Magn. Mater. **308**, 214 (2007).
[6] J.H. Park, Y.K. Hong, S. Bae, J.J. Lee, J. Jalli, G.S. Abo, N. Neveau, S.G. Kim, C.J. Choi and J.G. Lee, J. Appl. Phys. **107**, 09A731 (2010).
[7] H.X. Wang et al, Open J. of Microphysics **1**, 19 (2011).
[8] M. Matsumoto, A. Morisako and J. Ohshima, J. Appl. Phys. **69** 5172 (1991).
[9] H. Ebert, D. Kodderitzsch and J.Minar, Rep. Prog. Phys. **74** 096501 (2011).
[10] S.H. Vosko, L. Wilk and M. Nusair, Can. J. Phys. **58** (1980) 1200.
[11] J.S. Faulkner, Prog. Mater. Sci. 27 1 (1982); J. S. Faulkner and G. M. Stocks, Phys. Rev. B **21** 3222 (1980).

STUDIA UBB PHYSICA, Vol. 59 (LIX), 1, 2014, pp. 13-30
(RECOMMENDED CITATION)

ALLOY MICROSTRUCTURE AS REFLECTED BY THE EFFECTIVE BAND STRUCTURE: PARTIALLY ORDERED $In_{0.5}Ga_{0.5}P$ AND $In_{0.5}Ga_{0.5}As$

VOICU POPESCU[a] AND ALEX ZUNGER[b]

ABSTRACT. Random substitutional alloys have no long range order (LRO) or translational symmetry so rigorously speaking they have no $E(\vec{k})$ band structure or manifestations thereof. Yet, many experiments on alloys are interpreted using the language of band theory, for example by inferring van Hove singularities, band dispersion and effective masses.

While many standard alloy theories have the LRO imposed on the alloy Hamiltonian, assuming only on-site disorder, we have proposed a different way, by using large (thousands of atoms) randomly generated supercells in which chemically identical atoms are allowed to have different local environments (a polymorphous representation). This then drives site-dependent atomic relaxation as well as potential fluctuations. The eigenstates from such supercells are mapped onto the Brillouin zone (BZ) of the primitive cell, producing an effective band structure (EBS).

Our method is presented here to a certain detail and applied to study the effect of gradually increasing the LRO in partially ordered (001) (In,Ga)*X* (*X* = P and As) alloys. The results show that (In,Ga)P alloys exhibit band-like behaviour only near the centre and faces of the BZ, rapidly losing such characteristics away from Γ or for higher bands. This system further appears to respond much stronger to changes in its morphology. In contrast, (In,Ga)As shows characteristics of an effective medium alloy in which variations of the LRO has a rather small influence on its EBS.

Keywords: *Semiconductor compounds; electronic structure; pseudopotential methods; partial order*

[a] *Faculty of Physics, University Duisburg-Essen, Duisburg, Germany*
[b] *University of Colorado, Boulder, Colorado 80309, USA*

1 Introduction

The occurrence of partial order in form of layered structures in III-V alloys was discovered in the mid-late eighties in $InGaAs_2$ [1] and $InGaP_2$ [2]. This triggered an extensive experimental and theoretical research [3, 4, 5], and it is now known that, while disordered III-V alloys usually share the same crystal structure as their underlying zinc blende (ZnS, B3) components, essentially all of them can exhibit spontaneous or artificial (partially) ordered structures [4]. A perfectly ordered isovalent $A^{\rm III}B^{\rm III}C_2^{\rm V}$ alloy can crystallise in one of the structures depicted in Fig. 1(a): the group III atoms A and B occupy the cation sublattice [large blue spheres in Fig. 1(a)] to form either the (001)-oriented CuAu ($L1_0$), the (111)-oriented CuPt ($L1_1$) or, together with the anions, the chalcopyrite $CuFeS_2$ ($E1_1$) crystal structure [6]. Such layered periodic arrangements can be described by introducing a long range order (LRO) parameter η: The cations are distributed over alternating layers with nominal composition $A_{0.5-\eta/2}B_{0.5+\eta/2}$ and $A_{0.5+\eta/2}B_{0.5-\eta/2}$, where $\eta = 1.0$ corresponds to the perfectly ordered structure. In this case, the ensuing systems may be seen as $(AC)/(BC)$ *natural superlattices* with either (001), (111) or (210) orientations, depending on the adopted CuAu, CuPt, or $CuFeS_2$ cation arrangement.

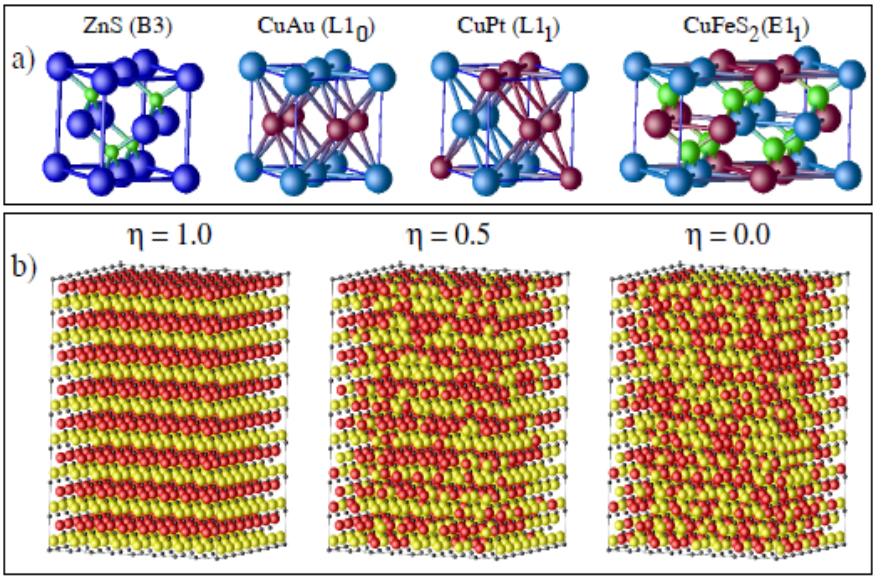

Figure 1: (a) Balls-and-sticks representations of the prototype ZnS (B3), CuAu ($L1_0$), CuPt ($L1_1$), and $CuFeS_2$ ($E1_1$) crystal structures. The zincblende (ZnS) structure is most common for the III-V semiconductors, with the cations and the anions depicted as large blue and small green spheres, respectively. Isovalent $(A^{\rm III}B^{\rm III})C_2^{\rm V}$ alloys may attain ordered structures like the chalcopyrite $CuFeS_2$ [(210)-oriented], or such in the cations sublattice $A^{\rm III}B^{\rm III}$ is either of type CuAu [(001)-oriented] or CuPt [(111)-oriented]. (b) Structural model of the 2048-atom supercells used in the calculations of the $In_{0.5}Ga_{0.5}X$ alloys. In these supercells the two cations In (red) and Ga (yellow) are randomly distributed according to the different values of the ordering parameter η (see text). For the completely ordered case ($\eta = 1.0$), the In-Ga sub-lattice corresponds exactly to the CuAu structure depicted in (a). At an intermediate value, $\eta = 0.5$, In-rich and Ga-rich layers alternate along the vertical (001) direction, whereas for $\eta = 0.0$ the cation sub-lattice is completely random.

Spontaneous (111) long range order in otherwise random $In_{0.5}Ga_{0.5}X$ alloys with X =P and X =As has been explained theoretically [4, 7, 8] as arising from the stablest arrangement of two cations (Ga and In) on the *reconstructed* (001) surface, an arrangement that is frozen-in by subsequent coverage, thus extending into macroscopically thick samples. In the absence of reconstruction, the site preference for Ga versus In is lost, and so is the (partial) ordering. The delicate dependence of this process on surface steps, on deviations of composition from $x = 0.5$ and its competition with phase-separation tendencies contribute to an imperfect degree of the LRO parameter $\eta < 1$.

The most striking feature observed in these systems was the optical band gap reduction induced by the ordering. Simple symmetry considerations [9, 10] have shown that this occurs because of the combined effect of several factors:
(i) the lowering of the symmetry (tetragonal for $L1_0$ and rhombohedral for $L1_1$) causes the valence band maximum (VBM) Γ_{8v} state to split, effectively leading to a raising of the VBM in the ordered phase;
(ii) the original Γ-states of the zinc blende structure will fold into Γ-states of $L1_0$ ($L1_1$) and couple to the original zinc blende X_z (L_{111})-states that will also fold into $\bar{\Gamma}$-states of $L1_0$ ($L1_1$) structure. This generally leads to a lowering of the conduction band minimum (CBM) of the ordered phase.

Electronic structure calculations performed so far for these systems modelled the structural disorder by means of special quasi-random structures (SQSs) [11] or by employing large supercells [12, 13, 14, 15]. These calculations, however, merely focused on band edge states, tracking the dependence on the partial order of specific quantities such as the optical band gap, the absorption intensities, the indirect gaps and the effective mass.

Here we enquire about the effect of ordering in the rest of the Brillouin zone (BZ). Whereas the formation of configurationally disordered alloys is inevitably associated with loss of LRO and hence with the automatic loss of the concepts of E versus $\vec{k}$ band structure and its derived quantities, the band structure language of $E(\vec{k})$ continues to be enormously useful to phenomenologically describe trends with alloy composition x from the ordered $x = 0.0$ and $x = 1.0$ constituents to disordered structures for intermediate x. Such a link between the realistic treatment of substitutional disorder by using large simulation boxes (supercells) and the intuitive picture of a dispersion relation in a primitive BZ that preserves the *macroscopic* symmetry of the alloy can be accomplished via a computational tool recently developed by us [16, 17]. This transforms the energy eigenvalues obtained from (large) supercell calculations – whose content may include an arbitrary atomic microstructure – into an *effective* band structure (EBS) of alloy systems.

Examples of such supercell constructions are given in Fig. 1(b). These may represent either a perfectly ordered ($\eta = 1.0$), a partially ordered ($\eta = 0.5$), or a completely disordered ($\eta = 0.0$) (In,Ga)X alloy with sites occupied by In and Ga atoms via an appropriate probability function. The eigenvalues are first obtained by explicitly diagonalising the relevant single-particle Schrödinger equation in a large supercell containing many *local environments*. The results are afterwards transformed into an EBS in a reference primitive cell. In such a description, each of the X_i atom located on a lattice site $i = 1, \ldots, N$ in the supercell may have a distinctly different local environment, depending on the coordination of atom X_i with different amounts of In and Ga atoms, and so the ensuing EBS would correspond to a *polymorphous description* of the alloy, different from simplified descriptions in alloy theory (e.g., effective medium approximations) where all atoms, at a fixed composition x, are assumed to have the same potential.

The relevant steps involved in the EBS determination are provided in Section 2, where the general concepts of the procedure are described on a rather universal level, independent on the particular implementation of the underlying electronic structure calculations. Specific computational details pertinent to the current applications are given in Section 3. To illustrate the manifestation of non-random alloy microstructure on the EBS we shall consider (001)-partially ordered $In_{0.5}Ga_{0.5}X$ alloys (X =P and As), with the appropriate results discussed in Section 4.

In perfectly ordered $InGaX_2$ there are atomic layers perpendicular to the (001) direction which are made of pure Ga or pure In, whereas in partially ordered alloys such layers are mixed, being represented by alternate layers of $In_{1-x-\eta/2}Ga_{x+\eta/2}X$ and $In_{1-x+\eta/2}Ga_{x-\eta/2}X$. We will show how the different atomic micro-arrangements are reflected both qualitatively and quantitatively in the EBS. Varying the LRO parameter η allows us to go from the totally disordered $In_{0.5}Ga_{0.5}X$ alloys to the completely ordered $InGaX_2$ compounds. In particular, it will be shown that the coupling of various folded bulk states that leads to the band gap reduction manifests itself along the entire $\Gamma - Z$ direction of the primitive Brillouin

zone, the effect being stronger for the (In,Ga)P system. In addition, a side-by-side comparison of the EBS derived for the two alloys (In,Ga)As and (In,Ga)P reveals that, while a reduction of the LRO parameter η significantly diminishes the Bloch character of the alloy states, (In,Ga)As remains much closer to an effective medium behaviour. The influence of disorder on the electronic structure is weaker in (In,Ga)As than in (In,Ga)P.

2 How to extract an EBS from supercell calculations

The method we apply here allows one to generate what we termed as an "effective band structure" (EBS) for disordered alloys in the primitive BZ of the parent compounds and is based on a fully polymorphous description of the alloy. Unlike models that discard fluctuations at the outset [18, 19, 20], the substitutionally disordered alloy is first described using large supercells, containing possibly thousands of atoms

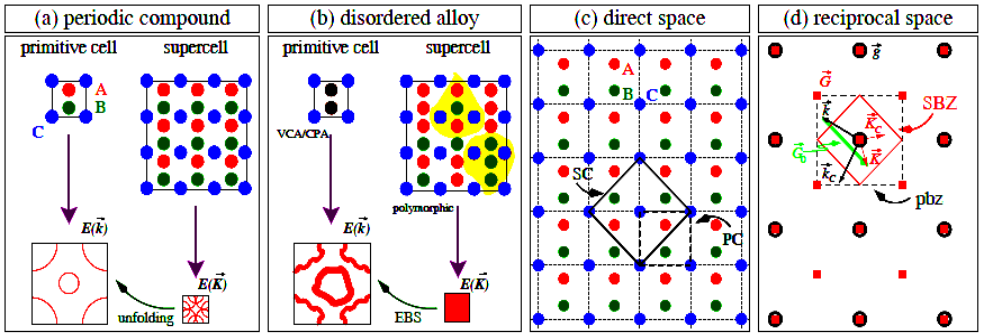

Figure 2: Two-dimensional representation of (a) a simple unfolding of bands for a periodic fictitious system ABC and (b) the analogy with periodic systems when treating an alloy $A_{1-x}B_xC$ by effective medium and polymorphic model approaches. The connection between the two representations of a primitive cell (PC) and a supercell (SC) in (c) real space and (d) reciprocal space. The PC and SC are related by a transformation similar to Eq. (1). The corresponding primitive (pbz) and supercell (SBZ) Brillouin zones, their associated wavevectors $\vec{k}$ ($\vec{K}$) and translation vectors $\vec{g}$ ($\vec{G}$) as well as folding (unfolding) relations are also illustrated. Figure taken from Popescu and Zunger [17]. © American Physical Society (2012).

with randomly (or correlated) distributed site occupations. The alloy eigenstates $\{|\Psi_i\rangle, \varepsilon_i\}$ are obtained by diagonalisation of the SC Hamiltonian. In a second step, the amount of Bloch character preserved in the SC eigenstates is explicitly *sought*, rather than being *a priori* assumed to exist. This is precisely what differentiates the present method from effective medium models: It conveys the effects of existence of a multitude of local environments through broadening and dispersion of the effective $E(\vec{k})$ relation of the EBS [16].

While a detailed description of our approach is given elsewhere [16, 17], we will discuss here its relevant steps, needed in understanding the results presented. This section introduces the concepts of folding and unfolding of wavevectors and associated states, defines the spectral function from which the EBS is derived, and illustrates the generation of an EBS for a simple case of a random alloy. The EBS procedure is discussed in this section on a very general level, valid in principle for any band structure calculation method using basis sets. Specific details related to our adopted implementation are given in the next section.

2.1 Main idea behind the EBS determination

We first note that a supercell (SC) is an artificial mathematical construction obtained by stacking a primitive cell (PC) along one or more spatial directions. In ordered systems, these two entities provide a dual description of the same space. We introduce the convention (and use it throughout) that small (capital) symbols refer to quantities related to the PC (SC). The respective unit cell vectors of the PC (SC) are then $\vec{a}_i$ ($\vec{A}_i$), with $i = 1, 2, 3$ denoting the Cartesian coordinates x, y, and z. An equivalent dual representation also holds for the reciprocal space with its lattice vectors $\vec{g}$ ($\vec{G}$) and wave vectors $\vec{k}$ ($\vec{K}$) corresponding to the PC (SC) Brillouin zone (pbz and SBZ).

The principle is illustrated in Fig. 2(a) and (b) for a fictitious two-dimensional (2D) system ABC. When dealing with the ordered, periodic compound ABC, Fig. 2(a), one can use either a SC or a PC to calculate its electronic structure. In both cases, dispersion relations $E(\vec{k})$ or $E(\vec{K})$ can be obtained directly. An *unfolding* technique [21, 22, 23, 24, 25] will enable the reconstruction of $E(\vec{k})$ *from* a directly calculated $E(\vec{K})$.

Analogously to the ordered system, one can treat also the disordered $A_{1-x}B_xC$ alloy, Fig. 2(b), in two ways. Applying effective medium theories such as the virtual crystal (VCA) [18] or the single-site coherent potential approximation (CPA) [20, 26], enforces a PC periodicity and obtains alloy dispersion relations. In the CPA case, these are given as "broadened bands" in terms of Bloch spectral functions [26]. Alternatively, the random system $A_{1-x}B_xC$ can be modelled by using large SCs, in which the atomic sites are occupied by A and B atoms following a coin-toss or other disorder procedures commensurate with the composition x. This leads to the natural occurrence of different local atomic environments around different atomic sites, as illustrated by the shaded areas in Fig. 2(b), a generic construction termed *polymorphic model*. The directly calculated SC eigenstates are then projected on a reference Hamiltonian defined over the PC. Following an unfolding step, this will determine an alloy effective band structure (EBS) $E(\vec{k})$. The constructed EBS will resemble a "broadened band complex" only inasmuch as such a picture, of a PC-periodic system, is preserved by the polymorphic model.

The crux of the EBS determination method is represented by the calculation of the spectral weight of a large number of SC eigenvalues [25] and the construction of a spectral function. Combining this spectral decomposition with a $\vec{k}$-unfolding algorithm [23], we could show [16, 17] that an alloy spectral function can, in practice, be obtained for any primitive $\vec{k}$ vector. We will focus on these steps in the next subsection, discussing the $\vec{k}$-folding and $\vec{K}$-unfolding. Once these notions are understood, the determination of the spectral function and, from it, the derivation of the EBS, follow in a straightforward manner.

2.2 Folding and unfolding of wavevectors

Constructing the SC essentially implies a stacking along (all or some of) the three spatial directions of the PC of a Bravais lattice. In matrix notation, the two sets of basis vectors introduced above are related by $\underline{\vec{A}} = \underline{M} \cdot \underline{\vec{a}}$, or:

$$\begin{pmatrix} \vec{A}_1 \\ \vec{A}_2 \\ \vec{A}_3 \end{pmatrix} = \begin{pmatrix} m_{11} & m_{12} & m_{13} \\ m_{21} & m_{22} & m_{23} \\ m_{31} & m_{32} & m_{33} \end{pmatrix} \cdot \begin{pmatrix} \vec{a}_1 \\ \vec{a}_2 \\ \vec{a}_3 \end{pmatrix} \quad , \qquad m_{ij} \in \mathbb{Z} \ . \tag{1}$$

The only condition imposed on the transformation matrix $\underline{M}$ is to be invertible (non-singular). In the most general case, $\underline{M}$ does not need to be diagonal, that is, the SC and PC unit vectors do not need to be collinear. The elements of $\underline{M}$ are integers ($m_{ij} \in \mathbb{Z}$), which corresponds to the case of a SC commensurate [23] to the PC, the only one considered here. The volumes of the PC and SC unit cells, v_{PC} and V_{SC}, are related by $V_{SC} = v_{PC} \cdot \det(\underline{M})$, whence the condition of non-singularity of $\underline{M}$.

Following the convention adopted above, we denote by $\vec{b}_i$ ($\vec{B}_i$) the respective unit cell vectors of the pbz (SBZ), constructed in the usual way [27]: $\vec{b}_i = (2\pi/v_{PC})(\vec{a}_j \times \vec{a}_k)$, and $\vec{B}_i = (2\pi/V_{SC})(\vec{A}_j \times \vec{A}_k)$. A relation similar to Eq. (1) connects the two bases, $\underline{\vec{B}} = \underline{M}^{-1} \cdot \underline{\vec{b}}$, while the volumes of SBZ and pbz are $V_{SBZ} = v_{pbz}/\det(\underline{M})$. The reciprocal lattice vectors $\vec{g}_n$ ($\vec{G}_n$) associated with the pbz (SBZ):

$$\vec{g}_n = \sum_i p_i \vec{b}_i, \quad p_i \in \mathbb{Z} \ , \tag{2a}$$

$$\vec{G}_n = \sum_i q_i \vec{B}_i, \quad q_i \in \mathbb{Z} \ , \tag{2b}$$

will form two infinite sets $\{\vec{g}_n\}$ and $\{\vec{G}_n\}$ with the obvious property [see also Fig. 2(d)] $\{\vec{g}_n\} \subset \{\vec{G}_n\}$; in other words, any $\vec{g}$-vector is a $\vec{G}$-vector.

Folding of states of different wavevectors in supercells depends only on the geometry and symmetry of the SC and its underlying PC, through their corresponding Brillouin zones SBZ and pbz. A wave-vector $\vec{k}$ (in pbz) is said to *fold* into a wave-vector $\vec{K}$ (in SBZ) [see Fig. 2(d)] if there exists a reciprocal lattice vector $\vec{G}_0$ such that:

$$\vec{K} = \vec{k} - \vec{G}_0 \ . \tag{3}$$

Conversely, a wave-vector $\vec{K}$ (of the SBZ) *unfolds* into $\vec{k}_i \in$ pbz if

$$\vec{k}_i = \vec{K} + \vec{G}_i \ , \qquad i = 1, \ldots, N_{\vec{K}} \ . \tag{4}$$

Despite their apparent equivalence, the equations (3) and (4) have been intentionally written down explicitly because they summarise the very principle of folding and unfolding of states. Indeed, the vectors $\vec{K}$ and $\vec{G}_0$ in Eq. (3) are *unique* for a given $\vec{k}$, which means that a given wave-vector $\vec{k} \in$ pbz is mapped precisely into a single wave-vector $\vec{K} \in$ SBZ (folding). In contrast, Eq. (4) shows that a given wave-vector $\vec{K}$ can be obtained from a number $N_{\vec{K}}$ of different $(\vec{k}_i, \vec{G}_i)$ pairs (unfolding). In other words, a SC state is made of $N_{\vec{K}}$ PC states, whereas one particular bulk state contributes to a unique SC state. Not surprisingly,

$$N_{\vec{K}} = \det \underline{M} \ , \tag{5}$$

which, as we could see, equals v_{pbz}/V_{SBZ}. This is illustrated in Fig. 2(d) for the 2D model system ABC: in this case $N_{\vec{K}} = 2$, with $\vec{K}$ unfolding into $\vec{k}_1 = \vec{K}$ ($\vec{G}_1 \equiv \vec{0}$) and $\vec{k}_2 = \vec{k}$ ($\vec{G}_2 \equiv \vec{G}_0$). Let us also note here that $N_{\vec{K}}$ refers to the full Brillouin zone, not to its irreducible part; that is, some of the $\vec{k}_i \in$ pbz wavevectors may be related by symmetry operations of the PC space group.

2.3 Folding and unfolding of states

Standard electronic structure calculation methods can be applied to a periodic solid using either a PC or a SC representation. Because of periodicity in both PC and SC, $\vec{k}$ (PC) and $\vec{K}$ (SC) are good quantum numbers. By solving the associated Schrödinger equation of the electronic system one can readily obtain both the eigenvectors $|\vec{k}n\rangle$ and $|\vec{K}m\rangle$ (where n and m stand for band indices) and the dispersion relations, $E(\vec{k})$ and $E(\vec{K})$, which are well defined quantities in both representations. The zone folding and unfolding geometric relations lead to the property that any SC eigenvector $|\vec{K}m\rangle$ can be expressed as a linear combination of PC eigenvectors $|\vec{k}_i n\rangle$ $(i = 1, \ldots, N_{\vec{K}})$ [28, 22]. Commonly termed as *folding* of the bulk pbz into the SBZ, this is formally expressed as:

$$|\vec{K}m\rangle = \sum_{i=1}^{N_{\vec{K}}} \sum_n F(\vec{k}_i, n; \vec{K}, m) |\vec{k}_i n\rangle \ , \tag{6}$$

where the projections $F(\vec{k}_i, n; \vec{K}, m)$ are real numbers. The purpose of an *unfolding* procedure is to recover, from the SC calculation alone, either: (i) the PC eigenvectors $|\vec{k}_i n\rangle$ and their contributions $F(\vec{k}_i, n; \vec{K}, m)$ to the SC eigenstates $|\vec{K}m\rangle$, or (ii) as illustrated in Fig. 2(a), the $E(\vec{k})$ picture from the often complicated $E(\vec{K})$. This last step can be accomplished by projecting $|\vec{K}m\rangle$ on all the PC Bloch states $|\vec{k}_i n\rangle$ of a fixed $\vec{k}_i$ and calculating the spectral weight [21, 22]

$$P_{\vec{K}m}(\vec{k}_i) = \sum_n \left| \langle \vec{K}m \mid \vec{k}_i n \rangle \right|^2 \ . \tag{7}$$

This quantity represents the probability of finding a set of PC states $|\vec{k}_i n\rangle$ of energy E_n contributing to the SC state $|\vec{K}m\rangle$, or, equivalently, the amount of Bloch character $\vec{k}_i$ preserved in $|\vec{K}m\rangle$ [21, 22].

2.4 The spectral function for alloys

From $P_{\vec{K}m}(\vec{k}_i)$ one can further derive a spectral function (SF) of continuous variable E:

$$A(\vec{k}_i, E) = \sum_m P_{\vec{K}m}(\vec{k}_i)\delta(E_m - E) \ . \tag{8}$$

In the simple case of an SC obtained by a spatial repetition of identical PCs, without changing the symmetry of the lattice [as in the example of Fig. 2(a)], the spectral weights are

$$P_{\vec{K}m}(\vec{k}_i) = g_n(\vec{k}_i)\,\delta(E_m - E_n) \ , \tag{9}$$

where $g_n(\vec{k}_i)$ is the (bulk) degeneracy of the PC state $|\vec{k}_i n\rangle$. The SF will then be a set of delta functions of amplitude $g_n(\vec{k}_i)$ at each eigenvalue $E_n(\vec{k}_i)$ of the PC Hamiltonian, which reconstructs exactly the $E(\vec{k})$ provided by a direct PC calculation [see Fig. 2(a)]. This is because, by such a construction, no additional, symmetry governed coupling is introduced between the PC states $|\vec{k}_i n\rangle$. In Section 3.3 we will discuss the special case of superlattices, where the symmetry of the folded stated *does* change.

The supercell construction proves to be a useful tool in the electronic structure calculation of substitutionally disordered alloys. By building a large SC, which is then randomly occupied by atoms of different species, one accommodates a polymorphic description of the investigated system allowing different local environments to appear inside the SC, as illustrated, for the fictitious 2D alloy $A_{1-x}B_xC$ by the highlighted areas in Fig. 2(b). In contrast to the case of ordered systems, the spectral weights determined from such a SC calculation will no longer be integer numbers, nor will the spectral functions consist of only delta functions. The different local environments and the inelastic scattering in the alloy will be reflected in a *finite width* of $A(\vec{k}, E)$ in *both* arguments $\vec{k}$ and E. Because of this finite width, it is useful to introduce the cumulative sum [23]:

$$S_{\vec{k}_i}(\mathcal{E}_n) = \int^{\mathcal{E}_n} A(\vec{k}_i, E)dE \ . \tag{10}$$

This function is characterised by steps of value $g(\vec{k}_i)$ whenever an "alloy band" of degeneracy $g(\vec{k}_i)$ is crossed [23]. Consequently, it is this auxiliary quantity that allows one to to actually introduce this very concept of alloy bands and perform an estimation of their positions and widths.

With the SF determined for a set of $\vec{k}$-vectors and over a wide range of energies one can recover the alloy EBS. Next subsection summarises the flow chart of the full EBS determination procedure on a concrete example of the weakly disturbed alloy $In_{0.1}Ga_{0.9}N$. Most of the steps are independent of the actual implementation of the electronic structure calculation.

2.5 Flow chart of EBS determination

We illustrate the actual construction of an EBS for an alloy system, $In_{0.1}Ga_{0.9}N$, that preserves, to a large extent, a recognisable band structure [16], as shown in Fig. 3. The necessary steps for an alloy EBS determination are the following:

(A) Geometry step (implementation independent):

One starts by choosing the SC to be used in modelling the alloy system and a reference PC over which to construct the EBS. While the SC needs to be constructed in such a way that its symmetry corresponds to the macroscopic (experimental) symmetry of the alloy its actual size needs to ensure a reasonable balance between accuracy and computational cost. The chosen PC, on the other hand, will define the pbz, its associated $\vec{k}$-space and will deal as reference for the EBS. Although the choice of the PC unit vectors $\vec{a}$ is not necessarily unique, Eq. (1) connecting $\vec{a}$ to $\vec{A}$ (SC unit vectors) must be fulfilled.

For the purpose of determining an EBS, one further assumes the existence of a set of "virtual crystal" eigenvectors $\{|\vec{k}n\rangle\}$, with $\vec{k} \in$ pbz. Their explicit calculation is not necessary, as they do not appear at all in the final expression of $P_{\vec{K}m}(\vec{k}_j)$ [17]. The only condition $|\vec{k}n\rangle$ need to fulfil is that they form a complete, orthonormal set:

$$\langle \vec{k}n \mid \vec{k}n' \rangle \;=\; \delta_{nn'} \;. \tag{11}$$

(B) Representation step (implementation independent):

Once the reference pbz has been defined, one should decide on a set of wavevectors $\{\vec{k}_i\} \in$ pbz for which the SFs and the EBS are determined. Since the *macroscopic* symmetry of the alloy needs to be enforced, the SFs $A(\vec{k}, E)$ over all symmetry related $\vec{k}$ vectors inside the pbz need to be averaged. Indeed, if the system were periodic, with C one of its symmetry operations, the PC (SC) wavevectors $\vec{k}$ and $\vec{k}_C = C\vec{k}$ ($\vec{K}$ and $\vec{K}_C = C\vec{K}$) would be equivalent, as shown in Fig. 2(d). For a *random alloy*, however, C is no longer a symmetry operation of the SC, and we therefore need to take into account explicitly *all* of the corresponding $\vec{K}_C = \vec{k}_C + \vec{G}$ vectors. This procedure increases the size of the chosen set $\{\vec{k}_i\}$, leading to the extended sets $\{\vec{k}_j\}$ and $\{\vec{K}_J\}$ ($J \geq 1$). The latter will provide, for the given SC and PC, all of the primitive vectors $\vec{k}_j$, via Eq. (4).

(C) Morphology step (implementation independent)

One decorates the SC, one random realisation at a time, by occupying the SC lattice sites with atoms, according to the alloy composition.

(D) Computational step (implementation dependent)

The SC eigenvalues and eigenvectors $\{E_m(\vec{K}_J), |\vec{K}_j m\rangle\}$ need to be determined for each SBZ wavevector $\vec{K}_J$. This step may include or not a geometry optimisation (relaxation) of the atomic positions, performed ahead of the eigenvalue problem. One then derives the SFs $A(\vec{k}_j, E)$, using Eqs. (8). In line with the macroscopic symmetry enforcement procedure, the effective, representative SF $\bar{A}(\vec{k}_i, E)$ at a point $\vec{k}_i$ is obtained as the average of SFs over all n_C wavevectors $\vec{k}_C$ belonging to the same symmetry class $C(\vec{k}_i)$ as $\vec{k}_i$:

$$\bar{A}(\vec{k}_i, E) = \frac{1}{n_C} \sum_{\vec{k}_C \in C(\vec{k}_i)} A(\vec{k}_C, E) \;. \tag{12}$$

(E) Graphical representation step (implementation independent)

If different random realisations are used, the steps (C) and (D) are repeated and the results stored. The statistically averaged SFs at each $\vec{k}_i$ are then collected into the EBS. This final product (a typical EBS) is shown in Fig. 3(b) and will serve as a general template for the rest of the results presented here.

The SC eigenvalues obtained for $In_{0.1}Ga_{0.9}N$ alloy and the corresponding SF generation are illustrated in Fig. 3(a). They have been explicitly calculated for two different SBZ wavevectors $\vec{K}$ and $\vec{K}'$. The derived SFs $\bar{A}(\vec{k}_i, E)$ at selected primitive $\vec{k}_i$ vectors are shown in red lines along the abscissas. The cumulative sums $S_{\vec{k}_i}$ defined by Eq. (10) are depicted in the same panels as $\bar{A}(\vec{k}_i, E)$ with green lines. It is easy to recognise the steps made by this function whenever crossing an "alloy band". For the present applications, a $\vec{k}_i$-dependent band width, the shaded areas in Fig. 3(a), is taken as the energy range in which $\bar{A}(\vec{k}_i, E) \geq 10^{-3}$ around a band centre. The final graphical representation of an EBS consists of collecting all of the SFs and the band widths in single E versus $\vec{k}$ plots, as those shown in Fig. 3(b), where the individual $\vec{k}_i$ vectors are designated by vertical thin lines to which the corresponding SFs $\bar{A}(\vec{k}_i, E)$ are aligned.

3 EBS implementation and computational details

With the basic principles for the EBS determination given, we provide in this section specific details on how the partially ordered CuAu layered structure of the (In,Ga)X alloys is modelled and on the adopted method to calculate the supercell eigenvalues. Since an increased order in the layered systems leads to an increased InX/GaX-superlattice behaviour, we discuss in the last subsection the important aspect related to the coupling of folded bulk states in superlattices.

3.1 Modelling the partially ordered layered structures

The degree of ordering in layered structures can be described by the LRO parameter η: The (partially) ordered alloy $In_xGa_{1-x}X$ will consist of successive layers occupied alternatively by In-rich and Ga-rich

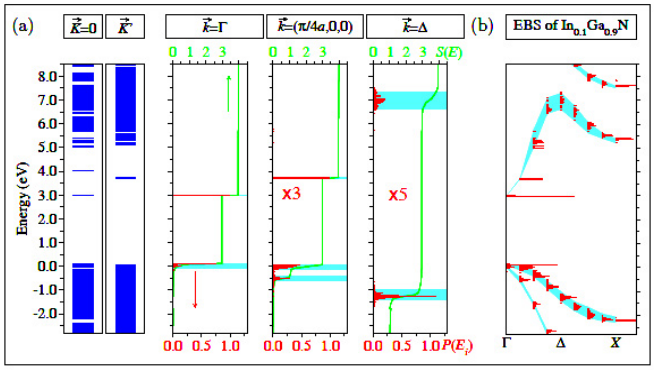

Figure 3: An example, for the $In_{0.1}Ga_{0.9}N$ alloy, on how the alloy EBS is obtained: (a) Supercell eigenstates $|\vec{K}m\rangle$ calculated at various $\vec{K}$'s are projected and then unfolded on the fcc BZ (pbz) vectors $\vec{k}_i = \vec{K} + \vec{G}_i$ [Eq. (4)], providing the spectral functions $\bar{A}(\vec{k}_i, E)$ [Eq. (12), red lines] and the cumulative sums $S_{\vec{k}_i}(E)$ [Eq. (10), green lines]; the latter quantity is used to determine the alloy bands positions and widths (shaded areas). (b) results for all $\vec{k}_i$ vectors (thin vertical lines) are put together into an E versus $\vec{k}$ plot, having along the abscissa also the spectral function amplitude. Figure taken from Popescu and Zunger [17]. © American Physical Society (2012).

alloys, according to the chemical formulas $In_{x+\eta/2}Ga_{1-x-\eta/2}X$ and $In_{x-\eta/2}Ga_{1-x+\eta/2}X$. The upper limit of η is given by $\eta_{max} = \min\{2x, 2(1-x)\}$. Obviously, $\eta = 0$ and $\eta = \eta_{max}$ will correspond to the two limiting situations, complete disorder and maximum order, of $In_xGa_{1-x}X$. Here we will consider the $x = 0.5$ case with $\eta = 0.0$, 0.5 and 1.0, and only the (001)-ordered CuAu ($L1_0$) phase. We use as building unit a tetragonal unit cell with the lattice vectors and atomic positions (in Cartesian coordinates) given by :

$$\begin{pmatrix} \vec{a}_1 \\ \vec{a}_2 \\ \vec{a}_3 \end{pmatrix} = \begin{pmatrix} 0.5 & -0.5 & 0.0 \\ 0.5 & 0.5 & 0.0 \\ 0.0 & 0.0 & 1.0 \end{pmatrix} \bar{a} \quad ; \qquad \begin{matrix} \vec{R}_{\text{cation}} : & \begin{matrix} (0.00\ 0.00\ 0.00)\ \bar{a} \\ (0.50\ 0.50\ 0.50)\ \bar{a} \end{matrix} \\ \vec{R}_{\text{anion}} : & \begin{matrix} (0.50\ 0.00\ 0.25)\ \bar{a} \\ (0.00\ 0.50\ 0.75)\ \bar{a} \end{matrix} \end{matrix} \tag{13}$$

Here $\bar{a}$ is the average lattice constant of the $In_{0.5}Ga_{0.5}X$ alloy, as given by Vegard's law. It is this primitive cell that defines the corresponding $\vec{k}$-space for the Bloch basis functions used in projecting the alloy eigenvalues, according to the methodology described above.

For better statistics, it is important to have the layers along the ordering direction equally sized in the supercell. Indeed, for $\eta = 0.5$, alternative In-rich and Ga-rich layers are formed but the distribution within a single layer of $In_{0.75}Ga_{0.25}As$ (or $In_{0.25}Ga_{0.75}As$) is still *random*, i.e., no identical layers are found along each supercell c-axis. Thus, the EBS in the case of $\eta = 0.5$ and $\eta = 0.0$ has been calculated using supercells defined by the vectors

$$\begin{pmatrix} \vec{A}_1 \\ \vec{A}_2 \\ \vec{A}_3 \end{pmatrix} = \begin{pmatrix} 4.0 & -4.0 & 0.0 \\ 4.0 & 4.0 & 0.0 \\ 0.0 & 0.0 & 8.0 \end{pmatrix} \bar{a} \ , \tag{14}$$

containing a number of 2048 atoms, as illustrated in Fig. 1(b).

3.2 Eigenstates of a random alloy by supercell calculations

After decorating the SC with a random realisation, we allow the atoms to relax about their initial positions $\vec{R}^0_{n\alpha}$ so as to minimise the elastic strain energy in the SC. During this process, most of the bonds In-X and Ga-X of the $In_{0.5}Ga_{0.5}X$ alloy will tend towards their "natural" (equilibrium) values in the corresponding binaries, leading to local relaxation. We calculate the elastic energy by means of a valence force field (VFF) functional [29, 30] in its generalised form [31]. The elastic energy is expressed as a sum of three terms, representing the bond stretching, bond angle bending, and bond-length/bond-angle interactions. Each of these terms is described by VFF parameters which are related to the elastic coefficients of the corresponding bulk materials [31].

At a given random realisation, we obtain the SC eigenvalues and eigenvectors by solving the single-particle equation

$$\left[-\frac{\beta}{2}\nabla^2 + \sum_{n,\alpha} \widehat{v}_\alpha(\vec{r} - \vec{R}_{n\alpha}, \underline{\varepsilon}_n) + \widehat{V}_{\alpha\text{NL}} \right] |\vec{K}m\rangle \ = \ E_m\, |\vec{K}m\rangle \ , \tag{15}$$

where $v_\alpha(\vec{r} - \vec{R}_{n\alpha}, \underline{\varepsilon}_n)$ is a screened atomic empirical pseudopotential depending on the identity α of the atom and the local strain tensor $\underline{\varepsilon}$ at its relaxed position $\vec{R}_{n\alpha}$:

$$v_\alpha(\vec{r}, \underline{\varepsilon}) \ = \ v_\alpha(\vec{r}, 0)\,[1 + \gamma_\alpha \text{Tr}(\underline{\varepsilon})] \ , \tag{16}$$

with γ_α a fitting parameter introducing a further dependence on the identity of the neighbours [32]. The other terms entering Eq. (15) are the non-local spin-orbit coupling potential $\widehat{V}_{\alpha\text{NL}}$ and a scaling factor, β, for the kinetic energy [32].

The unstrained pseudopotentials $v_\alpha(\vec{r}, 0)$ are determined by requiring that the bulk binaries described by $v_\alpha(\vec{r}, 0)$ fit experimental and local density approximation (LDA) high symmetry points (Γ, X and L) energy eigenvalues and effective masses. In addition, a fit of the bang gap bowing parameter of the $A_xB_{1-x}C$ alloy is performed for each AB/AC pair of binaries. Explicit values for the pseudopotential parameters used in this work are given elsewhere [33].

Using the pseudopotentials of each atom α and the relaxed positions $\vec{R}_{n\alpha}$, we solve the single-particle equation (15) by making a plane-wave Ansatz [34] for the eigenvector $|\vec{K}m\rangle$:

$$|\vec{K}m\rangle = \left[\sum_{\vec{G}} C_{\vec{K}m}(\vec{G})\, e^{i\vec{G}\vec{r}}\right] e^{i\vec{K}\vec{r}}\,, \quad \vec{K} \in \text{SBZ}\,, \tag{17}$$

where $\vec{G}$ are reciprocal lattice vectors in units of the SBZ, as given by Eq. (2b). The numerical determination of $|\vec{K}m\rangle$ and E_m is accomplished by diagonalising the Hamiltonian using the folded spectrum method [35].

Adopting a plane-wave expansion for the SC eigenvectors, it is straightforward to show [17] that the spectral weight $P_{\vec{K}m}(\vec{k}_j)$ of Eq. (7) is given by:

$$\begin{aligned} P_{\vec{K}m}(\vec{k}_j) &= \sum_{\vec{g}} \left| C_{\vec{K}m}(\vec{g}+\vec{k}_j-\vec{K}) \right|^2 \,, \\ &= \sum_{\vec{g}} \left| C_{\vec{K}m}(\vec{g}+\vec{G}_j) \right|^2 \,, \end{aligned} \tag{18}$$

where we took into account the unfolding relation, Eq. (4). In the last equation, $C_{\vec{K}m}(\vec{G})$ are the expansion coefficients obtained from the numerical diagonalisation of Eq. (15). As anticipated, $P_{\vec{K}m}(\vec{k}_j)$ is completely independent on the projecting Bloch functions $|\vec{k}n\rangle$ [17]. We recall here that $\{\vec{g}_j\} \subset \{\vec{G}_j\}$ and thus all $C_{\vec{K}m}(\vec{g}+\vec{G}_j)$ coefficients are well defined quantities.

3.3 Folding and coupling of bulk states in superlattices

Superlattices (SLs, also known as multilayers) denote layered structures of two or more materials periodically repeated along a certain spatial (growth) direction. For the maximum value of the LRO parameter $\eta = 1$, the systems investigated her form a short-period SL, $(\text{In}X)_1/(\text{Ga}X)_1$. In the context of folding states discussed in Section 2.3, SLs represent a particular situation in which the folding bulk states may change their symmetry in the SL as compared to bulk, and so couple one to another. This interplay between folding and coupling of folded states is important in understanding the nature of states in both SLs and quantum wells (QWs) [33, 36, 37, 38].

By construction, the tetragonal unit cell used to describe the completely ordered $\text{InGa}X_2$ (001)-oriented compounds will lead to a folding of the fcc $X_z = (0, 0, 2\pi/\bar{a})$ and $\Gamma = (0, 0, 0)$ points into the $\bar{\Gamma}$ point of the SC. We discuss in this subsection the expected effect of the folding and coupling of these bulk states and show how, only because of symmetry, the repulsion of the bulk conduction band states may lead to a reduction of the band gap in the ordered $\text{InGa}X_2$ compounds.

In zinc blende III-V semiconductors the two lowest conduction band states at the X-point of the BZ have the atomic orbital representations $|X^\alpha\rangle$ =(anion-s, cation-p) and $|X^\beta\rangle$ =(cation-s, anion-p) [39]. The $|X^\alpha\rangle$ state typically lies lower in energy than $|X^\beta\rangle$. Taking the origin of the coordinate system on an anion site (as done in this work), the two states are labelled $X_1 = X^\alpha$ and $X_3 = X^\beta$, being even and odd with respect to symmetry operations that change z into $-z$. A change of the origin to a cation site reverses this symmetry labelling [40] i.e., $X_1 = X^\beta$ and $X_3 = X^\alpha$. In order to avoid possible confusions, we use in the following the X^α/X^β notation.

We further note that in the cubic structures the three X points X_x, X_y and X_z in the BZ are equivalent and so any X-state is three-fold degenerate. This degeneracy is preserved in unstrained SLs, such as GaAs/AlAs or InAs/GaSb, but is lifted in strained systems such as InP/GaP or InAs/GaAs: under the biaxial deformation, the energy shift of the X_z and X_x/X_y band edges has opposite signs [33].

The zinc blende bulk states $|\Gamma_{1c}\rangle$, $|\Gamma_{15c}\rangle$ (first two band edges of the conduction band) and $|X_z^\alpha\rangle$, $|X_z^\beta\rangle$, folding into $\bar{\Gamma}$-point of the SBZ will couple only if both have the same irreducible representation at $\bar{\Gamma}$ (point group D_{2d}) with respect to symmetry operations that change z to $-z$ [36]. For the Γ-point related states one has [33, 41]:

$$|\Gamma_{1c}\rangle \mapsto \bar{\Gamma}_1(\Gamma_{1c}) \tag{19a}$$

$$|\Gamma_{15c}\rangle \mapsto \bar{\Gamma}_4(\Gamma_{15c}) + \bar{\Gamma}_5(\Gamma_{15c}) \tag{19b}$$

The irreducible representations of $|X_z^\alpha\rangle$ and $|X_z^\beta\rangle$, on the other hand, depend on the morphology of the SL [33, 36, 38, 41]. For common anion SLs (such as InP/GaP or InAs/GaAs) these representations are, respectively [33]:

$$|X_z^\alpha\rangle \mapsto \bar{\Gamma}_4(X_z^\alpha) \tag{19c}$$
$$|X_z^\beta\rangle \mapsto \bar{\Gamma}_1(X_z^\beta) \tag{19d}$$

.

Thus, couplings between the bulk states $|X_z^\alpha\rangle$ and $|\Gamma_{15c}\rangle$ as well as between $|X_z^\beta\rangle$ and $|\Gamma_{1c}\rangle$ are expected to occur. The latter leads to a repulsion of $|\Gamma_{1c}\rangle$ and $|X_z^\beta\rangle$ states, and was found to be responsible for: (i) the band gap reduction, by lowering the CBM, in $InGaAs_2$ and (ii) for the localisation of the CBM state in the GaAs sublattice [41]. One should note here that the strength of a symmetry allowed coupling will obviously depend on the energy separation between the coupling states.

4 Results and discussions

We start this section by presenting the band structure for the perfectly ordered compounds $InGaP_2$ and $InGaAs_2$ (LRO parameter $\eta = 1.0$) and discuss its main characteristics, in particular with respect to that

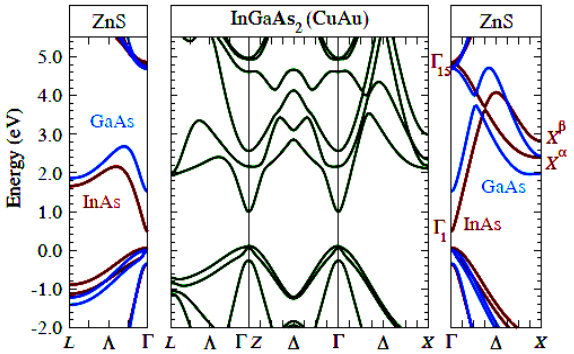

Figure 4: Band structure of the totally ordered $InGaAs_2$ compound in the layered (001) structure, with the In and Ga atoms building a CuAu ($L1_0$) sublattice. Although the primitive cell is tetragonal, with alternating (001)-oriented layers of pure In and Ga, the high symmetry points notation corresponds to the fcc BZ. With this convention, the Z-point at $(0, 0, 2\pi/a)$ folds into the Γ-point. Energy reference is the GaAs VBM (-5.628 eV). Relative to this value, the $InGaAs_2$ VBM and CBM lie at 0.112 eV and 0.984 eV, respectively, with a corresponding band gap of 0.872 eV. The side panels show for comparison the band structure of the zinc blende compounds InAs (dark red lines) and GaAs (light blue lines) along the $\Gamma - L$ (left) and $\Gamma - X$ (right) directions of the fcc BZ. The valence band offset between InAs and GaAs is 0.058 eV.

of the parent zinc blende compounds InP/GaP and InAs/GaAs. We then compare the extracted EBSs for $\eta = 0.5$ and $\eta = 0.0$ in both systems, evidencing the qualitative and quantitative differences brought upon by reducing the degree of ordering in the cation layers.

We will show that our calculations correctly reproduce the expected reduction of the band gaps in both ordered compounds $InGaAs_2$ and $InGaP_2$ based on the symmetry arguments expressed by the Eqs. (19). We find, however, that the $\bar{\Gamma}_1(X_z^\beta) - \bar{\Gamma}_1(\Gamma_{1c})$ repulsion is much stronger in the latter compound. The reason for this different behaviour will be related to the indirect band gap character of GaP.

A side-by-side comparison of the EBS derived for the two alloys demonstrates, first of all, the suitability of the EBS procedure as an investigative tool for (partially) disordered alloys. Specific to the (In,Ga)X systems presented here, the EBSs reveal that the repulsion mechanism manifests itself even in cases of partial order (LRO parameter $\eta = 0.5$) and it is not restricted to the $\bar{\Gamma}$-point of the SC, but along the entire folding direction $\Gamma - Z$ in the conduction band. In contrast, its influence on the valence band is rather negligible.

As such, a rather intimate connection between the degree of order and the complete EBS of the partially ordered alloys appears to exist. In addition, we will show that, while a reduction of the LRO parameter η significantly diminishes the Bloch character of the alloy states for both (In,Ga)As and (In,Ga)P, the former remains much closer to an effective medium behaviour, leading to the conclusion that the influence of disorder on the electronic structure is weaker in (In,Ga)As than in (In,Ga)P.

4.1 Band structure of ordered InGaX_2 compounds

The band structure of the totally ordered $InGaAs_2$ and $InGaP_2$ compounds in the layered (001) structure is shown in Figs. 4 and 5 along three directions of the tetragonal BZ connecting the points of coordinates $\Gamma = (0,0,0)$, $X = (1,0,0)$, $Z = (0,0,1)$, and $L = (1/2,1/2,1/2)$ (in units of $2\pi/\bar{a}$). The high symmetry points notation actually corresponds to the fcc BZ, kept for a consistent comparison with the band structure of the parent zinc blende compounds displayed at the sides of each figure. The Γ and Z points are in this case folding into the $\bar{\Gamma}$ point of the tetragonal BZ, as can be recognised from the reflection

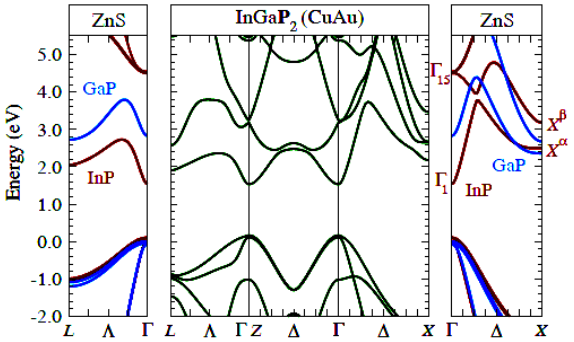

Figure 5: Same as Fig. 4 but for $InGaP_2$. Energy reference is the GaP VBM (-6.098 eV), relative to which the $InGaP_2$ VBM and CBM are at 0.167 eV and 1.529 eV, respectively. The corresponding band gap of $InGaP_2$ is then 1.362 eV. The side panels show the bands of InP (dark red lines) and GaP (light blue lines). The valence band offset between InP and GaP is 0.106 eV.

symmetry about the $\Delta = (0,0,1/2)$-point of the bands displayed along the $\Gamma - Z$ direction.

Plotting both of $\Gamma - X$ and $\Gamma - Z$ directions (which are equivalent in the fcc BZ) allows one to directly observe the changes induced in the band structure as a consequence of folding and coupling of bulk states. The $\Gamma - L$ direction, on the other hand, has been included in order to emphasise on the rather minor modifications caused in the band dispersion by an increased order along a non-collinear direction, and so lacks a symmetry-induced coupling between bulk states.

There are certain characteristics that the two compounds $InGaAs_2$ and $InGaP_2$ share. First of all, both are direct band gap semiconductors. With the empirical pseudopotentials fitted to deliver the experimental band gap of the parent compounds [42], the band gap energies of the ordered systems, as determined by our calculations, are $E_g = 0.872$ eV and 1.362 eV, respectively, for $InGaAs_2$ and $InGaP_2$.

A direct comparison of the $E(\vec{k})$ curves in the two figures, Fig. 4 and Fig. 5, reveals that the two systems have qualitatively similar dispersions throughout the whole valence band (VB) and, along the $\Gamma - L$ direction, also in the conduction band (CB). It can also be seen that, in these regions, the $\vec{k}$-dependence of the energy bands in the two compounds is akin to that in the respective parent compounds.

Moreover, the VB of both $InGaAs_2$ and $InGaP_2$ along $\Gamma - Z$ appears as a straightforward folding of the corresponding $\Gamma - X$ band structure. The reason for this behaviour is the obvious absence of coupling between folding states. Along the $\Gamma - L$ direction both in VB and CB the folding bulk states remain of different symmetries, such that no coupling is actually expected. Along the $\Gamma - Z$ direction in the VB, on the other hand, the folding X_z states lie very deep in energy, about $2.5 - 3.0$ eV below the Γ_v states. For this reason, although not forbidden by symmetry, the coupling of VB folding states along $\Gamma - Z$ is extremely weak.

Turning now to the CB of the two compounds $InGaAs_2$ and $InGaP_2$, we note how rich the band complex appears along the $\Gamma - Z$ direction. The CB structure contains bands that are not only folded, as seen in the VB, but are characterised by an *anti-crossing* behaviour. This is in stark contrast to the $\Gamma - X$ direction, where the bands do *cross* each other, as a result of possessing different symmetries.

There are, nevertheless, some significant differences between the two systems, differences that originate from the characteristics of their parent compounds. First, we note the relative position of the CBM to that of the respective alloy partners. In $InGaAs_2$, the CBM lies approximately half way between InAs and GaAs, whereas in $InGaP_2$ it is almost aligned with the InP CBM. Second, along the folding $\Gamma - Z$ direction $InGaAs_2$ is seen to exhibit much flatter bands than $InGaP_2$.

For a ternary semiconductor alloy $A_xB_{1-x}C$ one can approximate the x dependence of a band edge eigenvalue (here, the CBM at Γ point) through a Vegard law type formula corrected for the bowing parameter b_g of the band gap:

$$E_\Gamma(x) = xE_\Gamma(AB) + (1-x)E_\Gamma(AC) - b_g x(1-x)\ . \tag{20}$$

The bowing parameters of (In,Ga)As and (In,Ga)P alloys are of comparable size [42]. One would therefore expect, for $x = 0.5$, the CBM position to be fairly similar in both $InGaAs_2$ and $InGaP_2$: about half way between the InAs/GaAs and InP/GaP CBMs. The actual results show that this expectation is fulfilled only for $InGaAs_2$. This indicates that the afore mentioned $\Gamma_1(X_z^\beta) - \Gamma_1(\Gamma_{1c})$ repulsion is much stronger in $InGaP_2$ than in $InGaAs_2$.

The reason for this different behaviour can be understood easily by comparing the band structures of the corresponding alloy partners. It is furthermore the source of the second observed peculiarity, the significant differences in the dispersion curves along $\Gamma - Z$ for $InGaAs_2$ versus $InGaP_2$.

As shown in the right most panel of Fig. 4, both InAs and GaAs are direct band gap semiconductors. In these two compounds, the $|X^\beta\rangle$ states (the second band edges at X-point in the CB) are relatively high in energy as compared to the $|\Gamma_{1c}\rangle$ state, the difference being $\simeq 0.91$ eV ($\simeq 2.35$ eV) for GaAs (InAs). As in the case of the VB, this large energy separation causes the coupling of the folding states to be extremely weak. On the other hand, as evidenced in Fig. 4, both InAs and GaAs have the $|\Gamma_{15c}\rangle$ state (second CB edge at Γ-point) relatively low and very close one to another. One should therefore expect the $\Gamma_4(X_z^\alpha) - \Gamma_4(\Gamma_{15c})$ coupling to be enhanced. It is the reason why, in the energy range displayed, the bands along the $\Gamma - Z$ direction tend to avoid each other.

In contrast to $InGaAs_2$, $InGaP_2$ is formed by a combination of direct (InP) and indirect (GaP) binaries. The $|X^\beta\rangle$ state of GaP lies only $\simeq 0.15$ eV below its $|\Gamma\rangle$ state, which, in turn, is $\simeq 0.35$ eV below the InP $|X^\beta\rangle$ state. It is this small separation of the folding bulk states, symmetry allowed to couple, responsible for the stronger $\bar{\Gamma}_1(X_z^\beta) - \bar{\Gamma}_1(\Gamma_{1c})$ repulsion in $InGaP_2$. Let us further note that the $|\Gamma_{15c}\rangle$ state of GaP is very high in energy, outside the displayed range in the right most panel of Fig. 5. As a result, the second CB of GaP is highly dispersive. The absence of this second band near the Γ-point in the 5 eV energy range above the CBM explains why, with less states available to fold and couple, the CB along $\Gamma - Z$ in $InGaP_2$ is less rich than in $InGaAs_2$.

Much of the physics related to folding and coupling of states discussed in this subsection obviously applies to perfectly periodic systems. By gradually introducing disorder in the layered systems we shall try to track down to what extent the order specific manifestations survive in the EBS of the partially ordered and completely disordered systems.

4.2 EBS of layered $In_{0.5}Ga_{0.5}X$ alloys

The EBS of the the partially ordered (001)-layered alloys $In_{0.5-\eta/2}Ga_{0.5+\eta/2}X$ / $In_{0.5+\eta/2}Ga_{0.5-\eta/2}X$ is plotted in Fig. 6 and Fig. 7 for $X =$ As and $X =$ P, respectively. In both figures the top panels correspond to an LRO parameter $\eta = 0.0$ (completely random), the bottom panels to $\eta = 0.5$ (partially ordered). The 'true' band structure of the corresponding ordered compound $InGaX_2$ has been also depicted, to serve as reference for the alloy EBS.

Each vertical thin line corresponds to a wavevector $\vec{k}$ for which the SF $A(\vec{k}, E)$ (the full set forming the actual EBS) is depicted using blue lines. The intersections of these vertical lines with the bands of the ordered compounds would correspond to delta functions in the case of a SF calculated for the ordered systems. Thus, the individual peaks of the alloy SFs allow us to identify – through their spread and displacement – to what extent (i) the Bloch character of the alloy states is preserved; and (ii) how much the alloy bands dispersion differs from that of the ordered compounds.

For the (In,Ga)As alloy EBS, shown in Fig. 6, it can be seen that, throughout the whole BZ, both in VB and CB, the alloy maintains to a large extent a Bloch character. In other words, the (In,Ga)As does behave as an effective medium. The alloy fluctuations caused by various environments around the As atom are small. We note, first of all, that the SFs have well defined peaks regardless of their $\vec{k}$ argument, albeit somehow more pronounced at the BZ edges. Second, these peaks follow nearly exactly the bands of the ordered compound both in the completely disordered ($\eta = 0.0$) and in the partially ordered ($\eta = 0.5$)

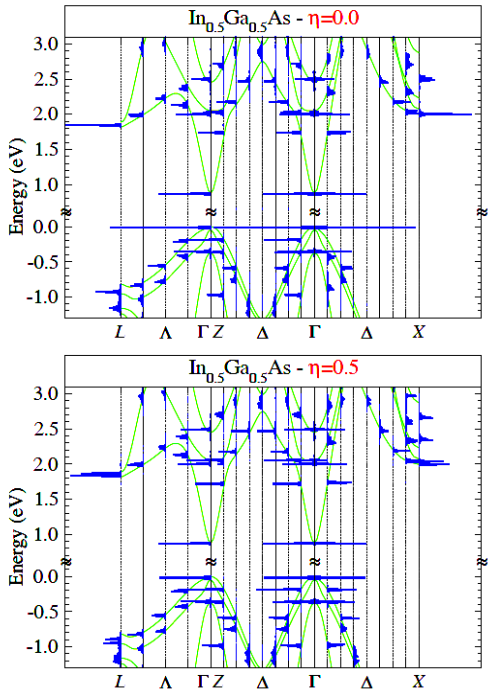

Figure 6: Effective band structure of the partially ordered (001)-layered alloy $In_{0.5-\eta/2}Ga_{0.5+\eta/2}As/In_{0.5+\eta/2}Ga_{0.5-\eta/2}As$, for $\eta = 0.0$ (top) and $\eta = 0.5$ (bottom). Notation of BZ high symmetry points is the same as in Fig. 4. Each vertical thin line corresponds to a wavevector $\vec{k}$ for which the SF $A(\vec{k}, E)$ is depicted in blue lines. Note that for $\eta = 0.0$ the alloys are perfectly random and their macroscopic symmetry is tetragonal. The alloy states have been calculated using the tetragonal SC defined by Eq. (14). The projection of alloy states has been done on the Bloch states of the tetragonal primitive cell of CuAu ($L1_0$) structure with lattice vectors given in Eq. (13). The bands of the completely ordered compound $InGaAs_2$ ($\eta = 1.0$) from Fig. 4 are shown for comparison using thin green lines. Energy reference is the $InGaAs_2$ VBM (−5.516 eV).

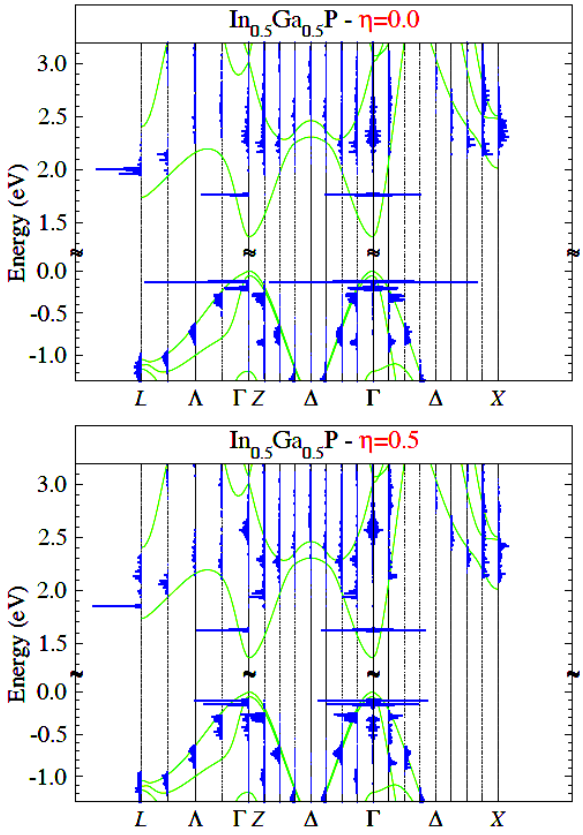

Figure 7: Same as Fig. 6 but for $In_{0.5-\eta/2}Ga_{0.5+\eta/2}P/In_{0.5+\eta/2}Ga_{0.5-\eta/2}P$. The bands of the completely ordered compound $InGaP_2$ ($\eta = 1.0$) from Fig. 5 are shown for comparison using thin green lines. Energy reference is the $InGaP_2$ VBM (-5.931 eV).

configurations. This holds even in the case of the $\Gamma - Z$ folding direction, showing that, to some degree, the symmetry-induced anti-crossing behaviour is preserved in the partially ordered system.

Comparing the EBSs obtained for $\eta = 0.0$ and $\eta = 0.5$, one can hardly tell the difference between the two. This is yet another indication of the small effect caused by the alloy fluctuations in (In,Ga)As. Also the band gap exhibits just a weak variation with η, increasing only slightly from 0.872 eV ($\eta = 1.0$) to 0.875 eV ($\eta = 0.5$) and 0.882 eV ($\eta = 0.0$).

The effect of ordering does show up, however, at the centre and at the edges of the BZ. For example, the alloy VBM at Γ-point is characterised by a sharp, large amplitude peak for $\eta = 0.0$, but it renders into two equally high peaks for $\eta = 0.5$, actually approaching the VBM splitting in the ordered compound. This splitting, caused by the crystal field, is a direct consequence of the increased order (and symmetry) for $\eta = 0.5$ versus $\eta = 0.0$, a feature effectively captured by the EBS. Similar improved resolutions of the bands for $\eta = 0.5$ against $\eta = 0.0$ can be observed also for the VB and CB at the L-point and for the CB at Γ- and X-points. In the latter case, the EBS exhibits in fact three different peaks, a similar number of band edges being present in the ordered $InGaAs_2$ compound.

A completely different situation is found for the (In,Ga)P alloy, with its EBSs for $\eta = 0.0$ and $\eta = 0.5$ depicted in Fig. 7. The deviations of the alloy CBM from that of the ordered $InGaP_2$ compound are clearly visible. With decreasing LRO parameter, the band gap changes from 1.362 eV ($\eta = 1.0$) to 1.731 eV ($\eta = 0.5$) and up to 1.888 eV ($\eta = 0.0$). This evidences the tremendous band gap reduction effect brought about by ordering in this system, consistent with the arguments discussed above for $InGaP_2$ and related to the indirect band gap character of one of the alloy partners.

As was the case for (In,Ga)As, also for (In,Ga)P is the EBS able to resolve the VBM splitting caused by the crystal field for $\eta = 0.5$ (bottom panel of Fig. 7). We do note, however, that (In,Ga)P is far from an effective medium alloy behaviour. Except for the centre and the edges of the BZ, one can not speak of a well-preserved Bloch character of the alloy states, neither can one recognise any "band structure" in the CB range, regardless of the η value. In fact, what we see above 2 eV in energy is a quasi-continuum distribution of states with non-zero projections on every $\vec{k}$ vector state of the primitive cell BZ. The VB does possess certain alloy bands but, as compared to (In,Ga)As, their widths are much larger. Apart from the BZ centre, increasing the alloy order seems to produce only a small effect.

5 Summary

We have investigated the changes induced by the partially ordering on the electronic structure of the layer-ordered isovalent (In,Ga)P and (In,Ga)As applying an approach which is based on a polymorphic description of the alloy disorder. The partial or complete random distribution of the atomic species is accounted for by means of large supercells from which an effective band structure (EBS) in a primitive Brillouin zone can be extracted using unfolding techniques combined with the numerical calculation of spectral functions. We have shown that the EBS is sensitive to the changes induced by an increased long range order (LRO) parameter even in the case of weakly perturbed alloy such as (In,Ga)As. The alloy states in this system are preserving to a large extent their Bloch character. In addition, the coupling of the folding states was found to be rather small, leading only to a minor reduction of the band gap upon increasing LRO parameter. In contrast, the (In,Ga)P alloy behaves as a strongly perturbed alloy, with the EBS exhibiting bulk-like sharp peaks only at the centre and edges of the Brillouin zone. Owing to the indirect band gap character of GaP, which brings the folding bulk states closer in energy, the band gap reduction induced by ordering through the increased symmetry is very large in (In,Ga)P.

Acknowledgements

Main part of this work has been accomplished during VP's extremely pleasant and fruitful employment at the National Renewable Energy Laboratory, in Golden, Colorado, within the Solid State Theory Group.

VP would also like to express his gratitude to Prof. Dr. Vasile Crişan under whose guidance he started his scientific adventure twenty-five years ago and with whom he learned the first, fundamental notions of Solid State Physics, such as Brillouin zone, wavevectors, electronic band structure, ingredients appearing also in the present contribution.

References

[1] T. Fukui and H. Saito, Japanese Journal of Applied Physics **23**, L521 (1984).

[2] A. Gomyo, T. Suzuki, and S. Iijima, Phys. Rev. Lett. **60**, 2645 (1988).

[3] H. Lee, M. V. Klein, J. M. Olson, and K. C. Hsieh, Phys. Rev. B **53**, 4015 (1996).

[4] A. Zunger, MRS Bulletin **22**, 20 (1997).

[5] J. D. Perkins, Y. Zhang, J. F. Geisz, W. E. McMahon, J. M. Olson, and A. Mascarenhas, J. Appl. Phys. **84**, 4502 (1998).

[6] A. Zunger and S. Mahajan, in *Handbook on Semiconductors*, 2nd ed., edited by T. S. Moss and S. Mahajan (Elsevier, Amsterdam, 1994), Vol. 3, pp. 1399–1513.

[7] G. P. Srivastava, J. L. Martins, and A. Zunger, Phys. Rev. B **31**, 2561 (1985).

[8] S. Froyen and A. Zunger, Phys. Rev. Lett. **66**, 2132 (1991).

[9] J. E. Bernard, S.-H. Wei, D. M. Wood, and A. Zunger, Appl. Phys. Lett. **52**, 311 (1988).

[10] S.-H. Wei, D. B. Laks, and A. Zunger, Applied Physics Letters **62**, 1937 (1993).

[11] S.-H. Wei and A. Zunger, Phys. Rev. B **49**, 14337 (1994).

[12] R. Osório, J. E. Bernard, S. Froyen, and A. Zunger, Phys. Rev. B **45**, 11173 (1992).

[13] D. B. Laks, S.-H. Wei, and A. Zunger, Phys. Rev. Lett. **69**, 3766 (1992).

[14] Y. Zhang, A. Mascarenhas, and L.-W. Wang, Phys. Rev. B **63**, 201312 (2001).

[15] Y. Zhang, A. Mascarenhas, and L.-W. Wang, Phys. Rev. B **78**, 235202 (2008).

[16] V. Popescu and A. Zunger, Phys. Rev. Lett. **104**, 236403 (2010).

[17] V. Popescu and A. Zunger, Phys. Rev. B **85**, 085201 (2012).

[18] A.-B. Chen and A. Sher, *Semiconductor Alloys: Physics and Materials Engineering* (Plenum Press, New York, 1995).

[19] W. Shan, W. Walukiewicz, J. W. Ager III, E. E. Haller, J. F. Geisz, D. J. Friedman, J. M. Olson, and S. R. Kurtz, Phys. Rev. Lett. **82**, 1221 (1999).

[20] J. S. Faulkner and G. M. Stocks, Phys. Rev. B **21**, 3222 (1980).

[21] T. G. Dargam, R. B. Capaz, and B. Koiller, Phys. Rev. B **56**, 9625 (1997).

[22] L.-W. Wang, L. Bellaiche, S.-H. Wei, and A. Zunger, Phys. Rev. Lett. **80**, 4725 (1998).

[23] T. B. Boykin, N. Kharche, G. Klimeck, and M. Korkusinski, J. Phys. Cond. Matter **19**, 036203 (2007).

[24] W. Ku, T. Berlijn, and C.-C. Lee, Phys. Rev. Lett. **104**, 216401 (2010).

[25] Y. Zhang and L.-W. Wang, Phys. Rev. B **83**, 165208 (2011).

[26] H. Ebert, D. Ködderitzsch, and J. Minár, Rep. Prog. Phys. **74**, 096501 (2011).

[27] N. W. Ashcroft and N. D. Mermin, *Solid State Physics* (Saunders College Publishers, New York, 1976).

[28] L. Bellaiche, S.-H. Wei, and A. Zunger, Phys. Rev. B **56**, 10233 (1997).

[29] P. N. Keating, Phys. Rev. **145**, 637 (1966).

[30] R. M. Martin, Phys. Rev. B **1**, 4005 (1970).

[31] K. Kim, P. R. C. Kent, A. Zunger, and C. B. Geller, Phys. Rev. B **66**, 045208 (2002).

[32] A. J. Williamson, L. W. Wang, and A. Zunger, Phys. Rev. B **62**, 12963 (2000).

[33] V. Popescu and A. Zunger, Phys. Rev. B **84**, 125315 (2011).

[34] A. Zunger, in *Quantum Theory of Real Materials* (Kluwer, Boston, 1996).

[35] L.-W. Wang and A. Zunger, J. Chem. Phys. **100**, 2394 (1994).

[36] Y.-T. Lu and L. J. Sham, Phys. Rev. B **40**, 5567 (1989).

[37] S.-H. Wei and A. Zunger, Journal of Applied Physics **63**, 5794 (1988).

[38] R. G. Dandrea and A. Zunger, Phys. Rev. B **43**, 8962 (1991).

[39] D. J. Chadi and M. L. Cohen, phys. stat. sol. (b) **68**, 405 (1975).

[40] T. N. Morgan, Phys. Rev. Lett. **21**, 819 (1968).

[41] P. Bogusławski and A. Baldereschi, Solid St. Comm. **70**, 1085 (1989).

[42] I. Vurgaftman, J. R. Meyer, and L. R. Ram-Mohan, J. Appl. Phys. **89**, 5815 (2001).

STUDIA UBB PHYSICA, Vol. 59 (LIX), 1, 2014, pp. 31-38
(RECOMMENDED CITATION)

ELECTRONIC STRUCTURE AND MAGNETIC PROPERTIES AND OF $La_{1.2}Nd_{0.2}Ca_{1.6}Mn_2O_7$ AND $La_{1.2}Sm_{0.2}Ca_{1.6}Mn_2O_7$ COMPOUNDS

R. DUDRIC[a,*], C. HIMCINSCHI[b], C. RUSU[a], I. GR. DEAC[a] AND R. TETEAN[a]

ABSTRACT. The magnetic properties and magnetocaloric effect of $La_{1.2}Nd_{0.2}Ca_{1.6}Mn_2O_7$ and $La_{1.2}Sm_{0.2}Ca_{1.6}Mn_2O_7$ are reported. The magnetic measurements indicate a second-order magnetic transition for $La_{1.2}Nd_{0.2}Ca_{1.6}Mn_2O_7$ and a first-order one for $La_{1.2}Sm_{0.2}Ca_{1.6}Mn_2O_7$. The decrease of the Curie temperature from ~247 K to ~198 K and ~176 K when La is substituted by Nd and Sm, respectively, can be correlated with the structural changes. The magnetic entropy changes determined from magnetization isotherms are higher for $La_{1.2}Sm_{0.2}Ca_{1.6}Mn_2O_7$ (6.45 J/kgK for ΔH = 4 T) than for $La_{1.2}Nd_{0.2}Ca_{1.6}Mn_2O_7$ (3.8 J/kgK for ΔH = 4 T). The high calculated values of the relative cooling powers in low magnetic field suggest the possibility to use these materials for magnetic refrigeration devices.

Keywords: *double layered manganites, magnetization, magnetocaloric effect*

INTRODUCTION

The interplay between structure, magnetic and transport properties in double layered manganites with the chemical formula $La_{2-2x}Ca_{1+2x}Mn_2O_7$ was the subject of many papers in the last two decades [1-6]. These doped double-layered manganites belonging to the Ruddelsden-Popper series consist of MnO_2 bilayers separated by insulating rock-salt layers, stacked along the *c*-axis, leading to a quasi-two-dimensional structure. The La and Ca ions can occupy two different sites: a twelve-fold-coordinate site in the middle of the MnO_2 layer, inside the perovskite blocks, and a nine-fold-coordinate site in the rock-salt layer, at the top and bottom of each block. The substitution of the trivalent La ion by the divalent Ca produces an

[a] *Faculty of Physics, Babes-Bolyai University, Kogalniceanu 1, 400084 Cluj Napoca, Romania.*
* *Corresponding author; e-mail address: roxana.pacurariu@phys.ubbcluj.ro*
[b] *Institut fur Theoretische Physik, TU Bergakademie Freiberg, Leipziger Str. 23, 09596 Freiberg, Germany.*

inhomogeneous distribution of mixed valence Mn^{4+}/Mn^{3+} ions, needed to maintain charge neutrality. The chemical randomness or the impurity doping may cause major modifications in the electronic phase diagram as well as in the magnetoelectronic properties. For doping concentrations $0.22 \le x \le 0.5$ the $La_{2-2x}Ca_{1+2x}Mn_2O_7$ manganites can have two transition temperatures for magnetic ordering [1], possibly originating from the anisotropic exchange interactions that are expected in these manganites: an intralayer exchange interaction within the MnO_2 bilayers and an interlayer exchange interaction acting between the perovskite MnO_2 bilayers. Among other intriguing properties these materials exhibit large magnetic entropy change (ΔS_m) and magnetocaloric effect under a moderate magnetic field [7-13]. In this paper we report the magnetic properties and magnetocaloric effect of $La_{1.2}R_{0.2}Ca_{1.6}Mn_2O_7$ compounds where R = Nd or Sm. The effects of Nd and Sm partial substitution for La on the magnetic properties of $La_{1.4}Ca_{1.6}Mn_2O_7$ are discussed.

EXPERIMENTAL

Polycrystalline samples with nominal composition $La_{1.2}R_{0.2}Ca_{1.6}Mn_2O_7$, where R = Nd or Sm were prepared. Stoichiometric proportions of La_2O_3, Nd_2O_3, Sm_2O_3 and $CaCO_3$ were mixed by high energy ball milling, calcinated at 900°C for 24 hours and then were pressed into pellets at 0.6 kbars and sintered in air at 900°C for 24 hours. For a better homogenization the samples were subsequently heated at 1200°C for 72 hours. The crystallographic structure of the samples was investigated by X-ray diffraction using a Bruker D8 Advance AXS diffractometer with Cr Kα radiation. A 12 T VSM from Cryogenics was used for magnetization measurements in the temperature range 4.2 – 300 K and external magnetic field up to 12 T. The magnetic entropy changes were determined from magnetization isotherms, between zero field and a maximum field (H_0) using the thermodynamic relation:

$$\Delta S_M(T, H_0) = S_M(T, H_0) - S_M(T, 0) = \frac{1}{\Delta T}\int_0^H [M(T+\Delta T, H) - M(T, H)]dT \qquad (1)$$

where ΔT is the temperature increment between measured magnetization isotherms (ΔT = 5K). The magnetic cooling efficiency was evaluated by calculating the relative cooling power (RCP) based on the magnetic entropy change:

$$\mathrm{RCP}(S) = -\Delta S_{\max}(T, H_0) \times \delta T_{FWHM} \qquad (2)$$

where ΔS_{max} represents the maximum magnetic entropy change and δT_{FWHM} its full-width at half-maximum.

RESULTS AND DISCUSSIONS

The X-ray diffraction analysis shows that the polycrystalline samples are single phase with a tetragonal $Sr_3Ti_2O_7$-type structure. The lattice parameters found for $La_{1.2}Nd_{0.2}Ca_{1.6}Mn_2O_7$ (a = b = 3.862 Å, c = 19.232 Å) and $La_{1.2}Sm_{0.2}Ca_{1.6}Mn_2O_7$ (a = b = 3.862 Å, c = 19.225 Å) are smaller than for $La_{1.4}Ca_{1.6}Mn_2O_7$ [12] (a = b = 3.863 Å, c = 19.240 Å) which can be due to the smaller ionic radius of Nd^{3+} and Sm^{3+} as compared to La^{3+}.

The temperature dependences of the magnetization in low field (0.2 T), presented in Figure 1, show a magnetic transition from a paramagnetic state to a ferrromagnetic order at temperatures below 250 K for both samples. As shown in the inset, the magnetization does not decrease to zero above the transition temperature, suggesting a 2D-magnetic order present even at room temperature. The Curie temperature calculated as the minima of the $\delta M/\delta T$ curves is 197.8 K for $La_{1.2}Nd_{0.2}Ca_{1.6}Mn_2O_7$ and 176.4 K for $La_{1.2}Sm_{0.2}Ca_{1.6}Mn_2O_7$, lower than the value 247.5 K found for the parent compound $La_{1.4}Ca_{1.6}Mn_2O_7$ [12]. The decrease of the Curie temperature can be correlated with the structural changes. The ionic radius of substitution atoms, Nd^{3+} and Sm^{3+}, are smaller than that of La^{3+} which leads to a distortion of the Mn-O-Mn angle and to the diminution of the exchange interaction strength. $La_{1.2}Nd_{0.2}Ca_{1.6}Mn_2O_7$ shows a wider ferromagnetic transition than $La_{1.2}Sm_{0.2}Ca_{1.6}Mn_2O_7$ as one can see in Figure 2 from the derivatives of magnetization data. In order to get an insight on the type of magnetic transition in our samples, we derived the Arrot plots (H/M vs. M^2) in the vicinity of T_C from the magnetization isotherms in magnetic field up to 4 T. The results plotted in Figure 3 indicate according to the Banerjee criterion [14] a second-order character of the magnetic transition for $La_{1.2}Nd_{0.2}Ca_{1.6}Mn_2O_7$ and a first-order magnetic transition for $La_{1.2}Sm_{0.2}Ca_{1.6}Mn_2O_7$. The Curie temperatures determined from the Arrott plots are very close to the values obtained from the $\delta M/\delta T$ curves.

The temperature dependences of the magnetic entropy changes around transition temperatures for $La_{1.2}Nd_{0.2}Ca_{1.6}Mn_2O_7$ and $La_{1.2}Sm_{0.2}Ca_{1.6}Mn_2O_7$ in magnetic fields of 2 T and 4 T are plotted in Figure 4. For comparison the temperature dependence of the magnetic entropy changes for $La_{1.4}Ca_{1.6}Mn_2O_7$ in magnetic field of 2 T is also shown. The maximum values of $|\Delta S_M|$ in 4 T and respectively 2 T magnetic field, listed in Table 1, are located at temperatures close to the magnetic transition ones. The $|\Delta S_M|$ peak for $La_{1.2}Nd_{0.2}Ca_{1.6}Mn_2O_7$ is nearly symmetric and its maximum value and temperature width strongly depend on the applied magnetic field, which is in general characteristic for a second order magnetic transition [15]. The decrease of the magnetic entropy change in respect to the parent compound $La_{1.4}Ca_{1.6}Mn_2O_7$ (2.85 J/kgK in 2 T) can be attributed to the diminution of the exchange interactions.

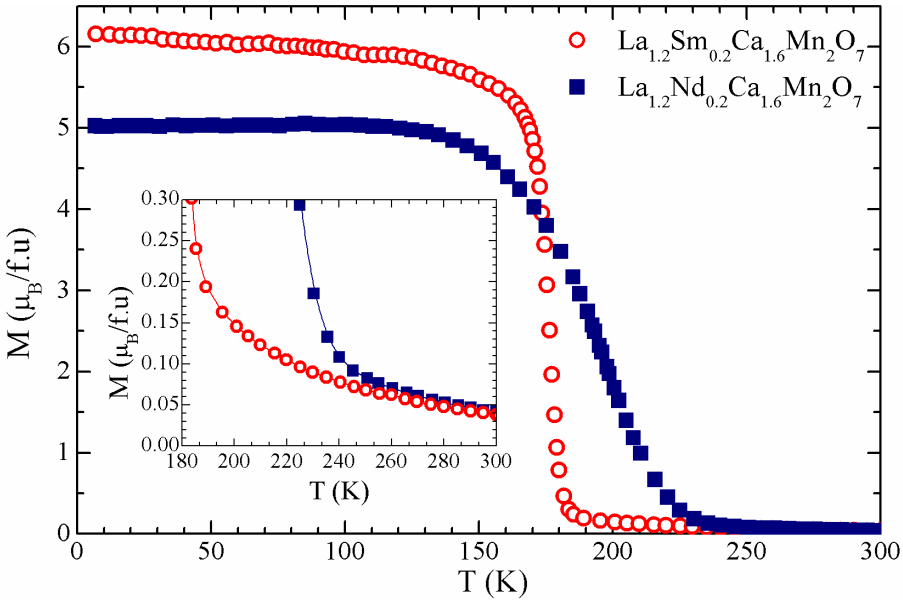

Fig. 1. The temperature dependences of the magnetization in 0.2 T magnetic field

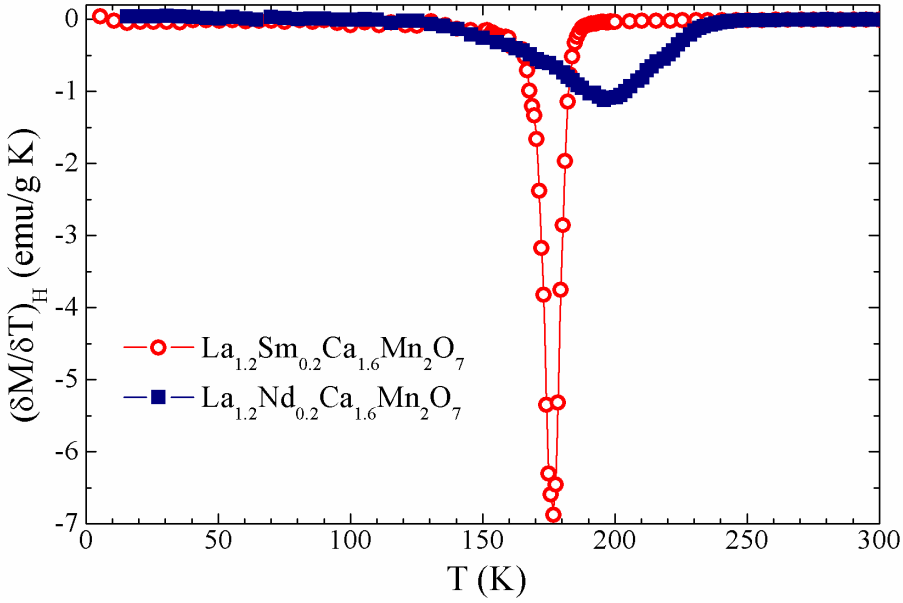

Fig. 2. The derivatives of magnetization M(T) data

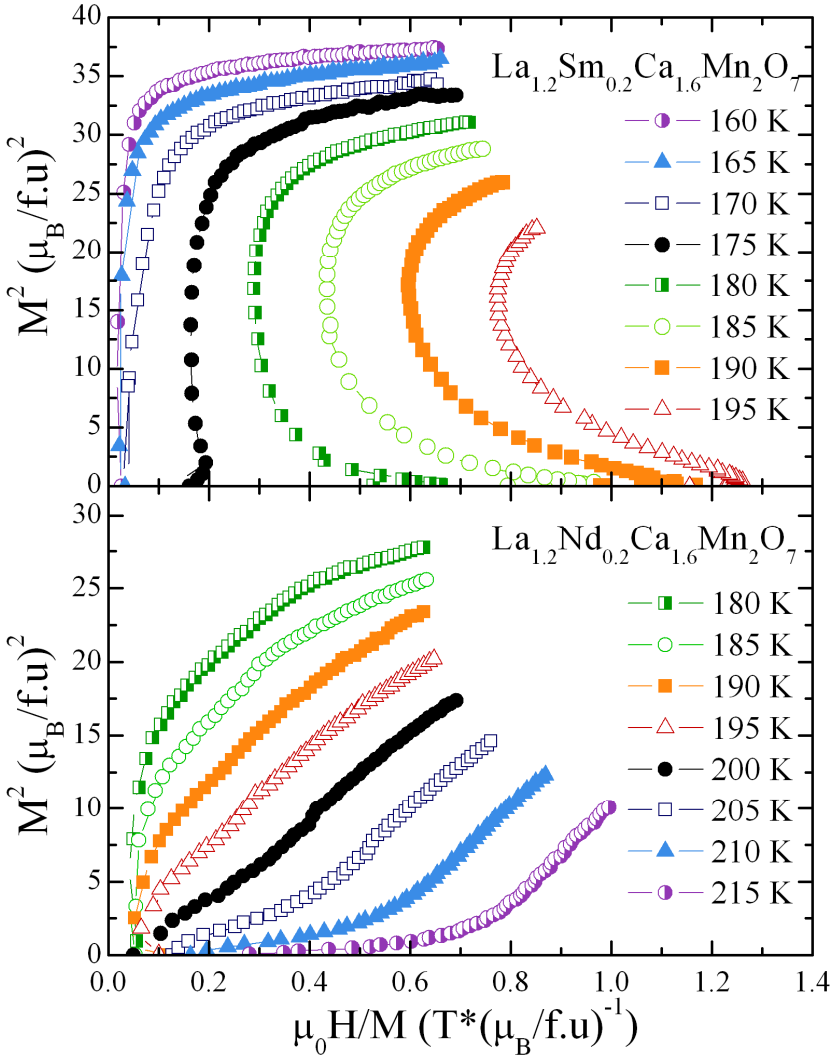

Fig. 3. Arrot plots for $La_{1.2}Sm_{0.2}Ca_{1.6}Mn_2O_7$ (up) and $La_{1.2}Nd_{0.2}Ca_{1.6}Mn_2O_7$ (down)

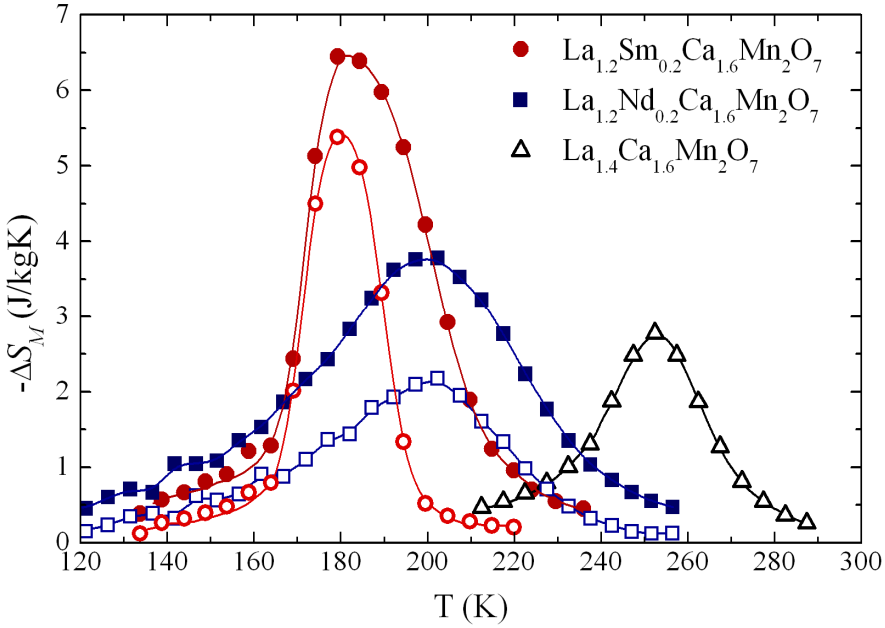

Fig. 4. Magnetic entropy changes around transition temperatures

The maximum values of the magnetic entropy changes are higher for $La_{1.2}Sm_{0.2}Ca_{1.6}Mn_2O_7$ and the temperature dependence shows an asymmetric peak, as expected in the case of a first order magnetic transition. Also the temperature width of the $|\Delta S_M|$ peak increases with H, but the maximum value is less sensitive to the applied magnetic field. Although the magnetic entropy change is a significantly higher for $La_{1.2}Sm_{0.2}Ca_{1.6}Mn_2O_7$, the relative cooling power values obtained in 2 T and 4 T for our samples are comparable, due to the broadened magnetic entropy curves of $La_{1.2}Nd_{0.2}Ca_{1.6}Mn_2O_7$. The RCP($S$) values in 2 T magnetic field (Table 1) are higher than for $La_{1.4}Ca_{1.6}Mn_2O_7$ (85.5 J/kg) and are comparable with those obtained in other oxide compounds.

Table 1.

Magnetocaloric properties of investigated manganites

	T_C (K)	$\mu_0 B$ (T)	T_{max} (K)	$\lvert\Delta S_{max}\rvert$ (J/kgK)	δT_{FWHM} (K)	RCP(S) (J/kg)
$La_{1.2}Nd_{0.2}Ca_{1.6}Mn_2O_7$	197.8	2	199.6	2.15	50	107.5
$La_{1.2}Nd_{0.2}Ca_{1.6}Mn_2O_7$		4	199.3	3.8	57	216.6
$La_{1.2}Sm_{0.2}Ca_{1.6}Mn_2O_7$	176.4	2	180.5	5.3	21	111.3
$La_{1.2}Sm_{0.2}Ca_{1.6}Mn_2O_7$		4	181.2	6.45	33	212.8

CONCLUSIONS

The structure, magnetic properties and magnetocaloric effect in $La_{1.4-x}R_xCa_{1.6}Mn_2O_7$ compounds where R = Nd or Sm have been investigated. The substitution of Nd or Sm for La does not affect the crystalline structure but it leads to a small decrease of the lattice parameters and of the Curie temperature. Using a criterion given by Banerjee, we have determined that $La_{1.2}Nd_{0.2}Ca_{1.6}Mn_2O_7$ exhibits a second order magnetic phase transition, while $La_{1.2}Sm_{0.2}Ca_{1.6}Mn_2O_7$ shows a first order transition. A large magnetic entropy change at temperatures close to the magnetic transition ones has been observed for both investigated manganites. The RCP(*S*) values calculated in a magnetic field of 2 T are higher than for $La_{1.4}Ca_{1.6}Mn_2O_7$. The high low-field relative cooling power values obtained for $La_{1.2}Nd_{0.2}Ca_{1.6}Mn_2O_7$ and $La_{1.2}Sm_{0.2}Ca_{1.6}Mn_2O_7$ suggest the possibility to use these materials for the magnetic refrigeration devices.

ACKNOWLEDGMENTS:

This work was supported by the Ministry of National Education, Romania, grant PN-II-ID-PCE-2011-3-0583.

REFERENCES

[1] H. Asano, J. Hayakawa, and M. Matsui, Phys. Rev. B **56**, 5395 (1997).
[2] K.V. Kamenev, M.R. Lees, G. Balakrishnan, and D. McK. Paul, Phys. Rev. B **56**, R12688 (1997).
[3] H. Asano, J. Hayakawa, and M. Matsui, Phys. Rev. B **57**, 1052 (1998).
[4] Neeraj Khare, Ajai K. Gupta, G.L. Bhalla, Solid State Commun. **132**, 799 (2004).
[5] Ajai K. Gupta, Rajesh Kumar, Vijay Kumar, G.L. Bhalla, Neeraj Khare, J. Phys. Chem. Solids **70**, 117 (2009).
[6] E. Tasarkuyu, A. Coskun, A.E. Irmak, S. Akturk, G. Unlu, Y. Samancioglu, A. Yucea, C. Sarikurkcu, S. Aksoy, and M. Acet, J. Alloys. Compd. **509**, 3717 (2011).
[7] Tie-Jun Zhou, Z. Yu, W. Zhong, X.N. Xu, H.H. Zhang, and Y.W. Du, J. Appl. Phys. **85**, 7975 (1999).
[8] H. Zhu, H. Song, Y.H. Zhang, Appl. Phys. Lett. **81**, 3416 (2002).
[9] A. Wang, G. Cao, Y. Liu, Y. Long, Y. Li, Z. Feng, J.H. Ross Jr., J. Appl. Phys. **97**, 103906 (2005).
[10] K. Cherif, S. Zemni, Ja. Dhahri, Je. Dhahri, M. Oumezzine, M. Ghedira, H. Vincent, J. Alloys Compd. **396**, 29 (2005).

[11] X. Zhao, W. Chen, Y. Zong, S.L. Diao, X.J. Yan, M.G. Zhu, J. Alloys Compd. **469**, 61 (2009).
[12] R. Tetean, C. Himcinschi, E. Burzo, J. Optoelectron. Adv. Mater. **10**, 849 (2008).
[13] A. Vladescu, S. Mican, C. Himcinschi, R.Tetean, J. Optoelectron. Adv. Mater **13**, 2- 4,263 **(**2011).
[14] S.K. Banerjee, Phys. Lett. **12**, 16 (1964).
[15] K.W. Zhou, Y.H. Zhuang, J.Q. Li, J.Q. Deng, Q.M. Zhu, Solid State Commun. **137**, 275 (2006).

STUDIA UBB PHYSICA, Vol. 59 (LIX), 1, 2014, pp. 39-45
(RECOMMENDED CITATION)

CONDUCTANCE OF A QUANTUM WIRE-SIDE-COUPLED-QUANTUM DOT SYSTEM

I. GROSU[a]

ABSTRACT. A system with an interacting quantum dot side-coupled to a wire is analyzed. Transport through the quantum wire is studied using the equation of motion method. It was shown that the conductance (transmission) provides a suppression due to the destructive interference effects. The one dip, and two dips structure of the conductance is obtained for large and for moderate Coulomb repulsion.

Keywords: *Conductance, Wire, Quantum dot, Coulomb interaction*

INTRODUCTION

An interacting quantum dot side-coupled to a metallic quantum wire is analogous to the Fano model [1] (a continuous spectrum and a discrete level). The Fano effect, first considered in atomic physics, is a typical quantum interference between resonant and continuous paths of conductive electrons. Recently, the Fano effect in mesoscopic systems containing quantum dots have been investigated in a large number of experimental and theoretical papers [2-6]. This arrangement is different from the standard geometry where a quantum dot is connected in series with leads and resonantly enhances the conductance. For this arrangement, if only the resonant level in the quantum dot takes effect, the conductance ca have a symmetric dip structure. The asymmetric dip line shape can appear in the case of non-resonant levels and asymmetric electron occupation of levels. The difference between classical Fano resonance, in which the resonant channel is of single-particle nature, and many-body Fano resonance with the resonant channel formed by Kondo effect was discussed in Refs.[7, 8]. In such a case the quantum dot in Kondo regime

[a] *Babes-Bolyai University, Faculty of Physics, 1 Kogalniceanu str., 400084 Cluj-Napoca, Romania.*
E-mail: ioan.grosu@phys.ubbcluj.ro

describes the adatom, with nonzero magnetic moment, and the wire which serves as an analog of the metallic surface host. It was shown [7], using the sum rule and the slave-boson treatment, that the Kondo effect provides a suppression of the transmission due to the destructive interference of the ballistic channel and the Kondo channel. In this paper we will investigate the conductance of the setup that consist by a single quantum dot, modelled by Anderson Hamiltonian, and side-attached to a perfect wire. The model can provide information applicable to various nanostructures.

MODEL

We consider an one-dimensional wire with a side-coupled Anderson quantum dot. Additionally, the tunneling between wire and dot will be assumed to be relatively weak, so that both the Coulomb electron-electron interaction, and the quantum interference are important. The Hamiltonian of the system is taken in the form:

$$H = \sum_{k,\sigma} \varepsilon_k c_{k\sigma}^{+} c_{k\sigma} + \sum_{\sigma} \varepsilon_d d_{\sigma}^{+} d_{\sigma} + U n_{\uparrow} n_{\downarrow} + \sum_{k,\sigma} t(c_{k\sigma}^{+} d_{\sigma} + d_{\sigma}^{+} c_{k\sigma}) \qquad (1)$$

Here: $c_{k\sigma}$ - describes the conduction electron in the wire with momentum k, energy ε_k and spin σ ; d_{σ} - describes the quantum dot localized electron with spin σ, and energy ε_d ; n_{σ} - is the number of electrons with the spin σ at the localized state, and with the Coulomb repulsion U ; t – denotes the tunneling matrix element between the quantum dot level and the wire.

In order to calculate the conductance of the system the Green's function of the electronic wave propagating through the wire, in the presence of the quantum dot, should be calculated. The Green's function $G_{\sigma}(\omega) = << c_{k\sigma} \mid c_{k\sigma}^{+} >>$ can be obtained from the equation of motion method (EOM) [9], as the solution of the following equation:

$$\omega G_{\sigma}(\omega) = 1 + \langle\langle [c_{k\sigma}, H] | c_{k\sigma}^{+} \rangle\rangle \qquad (2)$$

where: [A, B] represent the commutator between operators A and B. It can be calculated using the general form of the system's Hamiltonian. Following the (EOM) method the Green's function will be:

$$G_\sigma(\omega) = G^{(0)}(\omega) + G^{(0)}(\omega)T_\sigma(\omega)G^{(0)}(\omega) \tag{3}$$

where:

$$T_\sigma(\omega) = t^2 G_{d,\sigma}(\omega) \tag{4}$$

is the T-matrix of the system, and $G_{d,\sigma}$ is the Green's function of the dot. The form of the T-matrix depends on the geometry of the system and approximation made. $G^{(0)}(\omega)$ is a free conduction electron Green's function. The Green's function can be rewritten in the form:

$$G_\sigma(\omega) = \frac{1}{\omega + i\Gamma}\left[1 + \frac{t^2 G_{d,\sigma}(\omega)}{\omega + i\Gamma}\right] \tag{5}$$

where Γ is the coupling strength of the site zero (the position of the connection with the side dot) to other part of the wire (it is proportional to the kinetic energy of the electrons in the wire) [7]. For the Green's function of the dot, using the (EOM) method, we will obtain an atomic-like approximation (valid for weak tunneling):

$$G_{d,\sigma}(\omega) = \frac{1 - \langle n_{-\sigma}\rangle}{\omega - \varepsilon_d - S} + \frac{\langle n_{-\sigma}\rangle}{\omega - \varepsilon_d - U - S} \tag{6}$$

The values of $\langle n_\sigma \rangle$ should be determined through the self-consistency equation:

$$\langle n_\sigma \rangle = -\frac{1}{\pi}\int d\omega \cdot f(\omega) \cdot \mathrm{Im}\, G_{d,\sigma}(\omega) \tag{7}$$

$f(\omega)$ - is the Fermi function. We introduced:

$$S = \sum_k t^2 G^{(0)}(\omega) \cong -i\frac{t^2}{\Gamma} \tag{8}$$

Here a constant density of states for the wire at $-D < \omega < D$ is assumed ($\rho \approx 1/\pi\Gamma$). At low temperatures and bias voltage the linear response conductance is given by the Landauer-type formula [7]:

$$\boldsymbol{G} = \frac{2e^2}{h}\int d\omega \cdot \left(-\frac{\partial f}{\partial \omega}\right) \cdot T(\omega) \tag{9}$$

where $T(\omega)$ - is the transmission, related to the Green's function through:

$$T(\omega) = \Gamma^2 \left|G_\sigma(\omega)\right|^2 \tag{10}$$

At zero temperature the conductance is given by:

$$\boldsymbol{G} = \frac{2e^2}{h} \cdot T(0) \tag{11}$$

and:

$$g = \frac{\boldsymbol{G}}{\boldsymbol{G}_0} = T(0) \tag{12}$$

where $\boldsymbol{G}_0 = 2e^2/h$.

In the following we will calculate the normalized conductance g for infinite U. In this case:

$$G_{d,\sigma}(\omega) \cong \frac{1 - \langle n_{-\sigma} \rangle}{\omega - \varepsilon_d + i\dfrac{t^2}{\Gamma}} \tag{13}$$

and the normalized conductance becomes:

$$g = \frac{\overline{t^4} \cdot \langle n_{-\sigma} \rangle + \overline{\varepsilon_d^2}}{\overline{t^4} + \overline{\varepsilon_d^2}} \tag{14}$$

Here we introduced the scaled quantities: $\bar{t} = t/\Gamma$, and $\overline{\varepsilon_d} = \varepsilon_d/\Gamma$. The values of $\langle n_{-\sigma} \rangle$ are determined using Eq.(7), and a similar form for $\langle n_{-\sigma} \rangle$. We obtain the result:

$$\langle n_{-\sigma} \rangle = \frac{\frac{1}{2} - \frac{1}{\pi} \cdot \arctan\left(\frac{\overline{\varepsilon_d}}{\overline{t^2}}\right)}{\frac{3}{2} - \frac{1}{\pi} \cdot \arctan\left(\frac{\overline{\varepsilon_d}}{\overline{t^2}}\right)} \tag{15}$$

In Fig.1 we plot the normalized conductance as a function of the level position of the quantum dot.

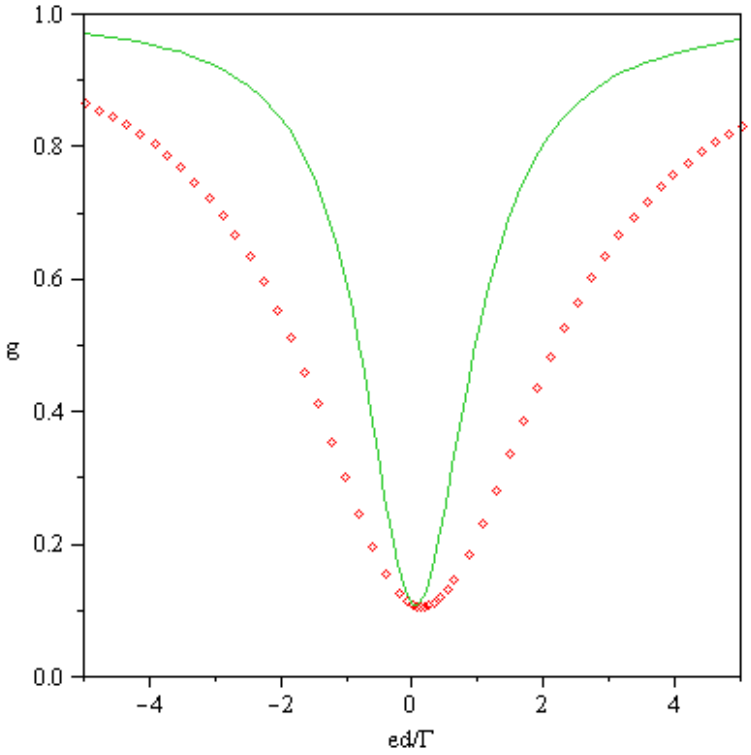

Fig. 1. Normalized conductance as function of the level position, for infinite repulsion, and for: $\bar{t} = 1$ (line); $\bar{t} = 1.5$ (doted line)

A dip occurs, as a peak does for a quantum dot connected with leads. A perfect transmission occurs where the coupling to the wire is small, for large $\left|\overline{\varepsilon_d}\right|$. In this case the destructive interference is (almost) absent. Close to the origin ($\overline{\varepsilon_d} \cong 0$) the reflection is almost perfect and it originates from a strong destructive interference between the ballistic and the resonant channel. This correspond to the dip in the normalized conductance.

For the case of finite U, using Eqs.(5), (6), (10) and (12), the normalized conductance becomes:

$$g = \frac{\overline{\varepsilon_d^2} \cdot (\overline{\varepsilon_d} + \overline{U})^2 + \overline{t^4} \cdot (\overline{\varepsilon_d} + \overline{U}\langle n_{-\sigma}\rangle)^2}{(\overline{t^4} + \overline{\varepsilon_d^2}) \cdot [\overline{t^4} + (\overline{\varepsilon_d} + \overline{U})^2]} \tag{16}$$

where: $\overline{U} = U/\Gamma$. Here, for simplicity, we will consider the non-magnetic case $\langle n_{-\sigma}\rangle = \langle n_{\sigma}\rangle = 1/2$. In Fig.2 we plot the normalized conductance for finite $\overline{U}$ ($\overline{U} = 3$), for two different couplings as a function of the level position of the dot.

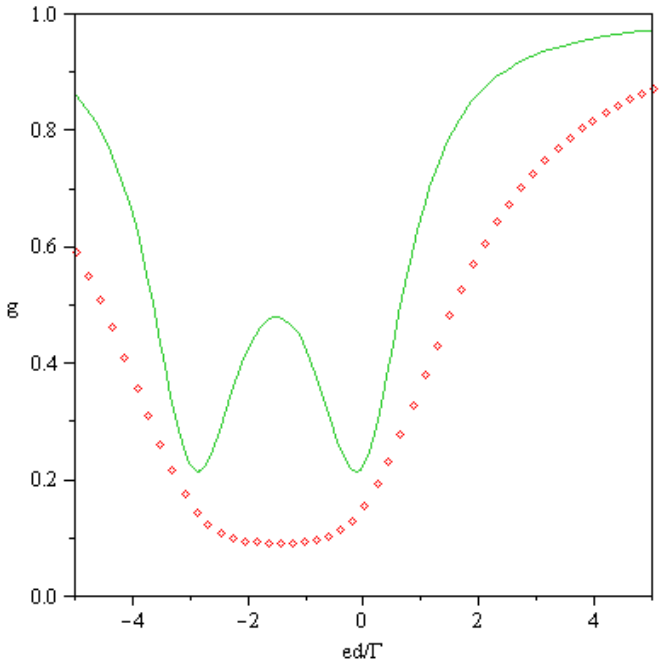

Fig. 2. Normalized conductance as function of the level position, for $\overline{U} = 3$, and for: $\bar{t} = 1$ (line); $\bar{t} = 1.5$ (doted line)

A two dips structure, due to the destructive interference with two resonant channels ($\overline{\varepsilon_d} = 0$, and $\overline{\varepsilon_d} = -\overline{U}$) could appear (the anti-Coulomb blockade behaviour). If the coupling strength increases, and the Coulomb repulsion is not too strong, the two dips structure vanish. The reflection is more effective on a wide interval of the level positions of the quantum dot.

CONCLUSIONS

We have analyzed the quantum transport through a quantum wire with a side-coupled interacting quantum dot. Using the equation of motion method we have shown that quantum interference leads to an almost perfect reflection of the electrons in both cases, for an infinite and for moderate repulsion. We obtained an one dip, and two dips structure of the conductance, depending on the strength of the Coulomb repulsion and the tunnelling between quantum dot and the wire. Our analysis does not include temperature effects. In the case of infinite repulsion, associated with the Kondo resonance, it was shown [7] that this system present perfect reflection of the electrons, in the limit of low energy level position of the quantum dot. When temperature increases [10], the Kondo effect diminishes and the scattering of the electron waves by the quantum dot's Kondo level becomes less effective.

REFERENCES

[1] U. Fano, *Phys.Rev.* 124, 1866, (1961).
[2] J. Göres et al., *Phys.Rev.B* 62, 2188, (2000).
[3] A.A. Clerk, X. Waintal, P.W. Brouwer, *Phys.Rev.Lett.* 86, 4636, (2001).
[4] K. Kobayashi, et al. *Phys.Rev.Lett.* 88, 256806, (2002).
[5] Xiong Shi-jie, Y. Yin, *Phys.Rev.B* 66, 153315, (2002).
[6] Xiong Yong-Jian, He Zhou-Bo, *Chin.Phys.Lett*. 21, 1802, (2004).
[7] Kicheon Kang, Sam Young Cho, Ju-Jin Kim, Sung-Chul Shin, *Phys.Rev.B* 63, 113304, (2001).
[8] P. Stefanski, *Solid State Commun.* 128, 29, (2003).
[9] D.N. Zubarev, *Usp.Fiz.Nauk* 71, 71, (1960) [*Sov.Phys.Uspeki* 3, 320, (1960)].
[10] T. Lobo, M.S. Figueira, M.E. Foglio, *Brazilian Journ.Phys.* 36, 397, (2006).

STUDIA UBB PHYSICA, Vol. 59 (LIX), 1, 2014, pp. 47-58
(RECOMMENDED CITATION)

NUMERICAL INVESTIGATIONS ON INFLUENCE OF DIE GEOMETRY AND RAM SPEED ON THE HOT EXTRUSION OF ALUMINIUM ALLOY

M. POP[a,*], D. FRUNZA[a], A. V. POP[b]

ABSTRACT. In the present work, an attempt was made to predict the force evolution during the extrusion of 7075 aluminium alloy by means of 3D FEM computer simulation. For this purpose the general F.E.A. software Forge-3D has been used to set up the finite element model of the hot aluminium extrusion. 7075 Aluminium was used as billet material, with 30 mm diameter and 30 mm length. The extrusion process was modeled as isothermal, which means that the billet material was preheated at a specific temperature and then it was pressured into the circular die, with different extrusion ratio. The extrusion speed was varied from 2 to 6 mm/s and also the extrusion die angles varied. The friction between work piece and die, concerns concerns Tresca model with 0.3 friction factor .

The influence of die angle, reduction ratio, ram speed, die temperature on the extrusion force during the extrusion process were investigated. Results show that die angle, ram speed, die land diameter has a significant influence on the extrusion force evolution.

Keywords: *FE-analysis, forward extrusion, aluminium alloy*

INTRODUCTION

Finite element analysis (FEA) has been developed during the last decades as a very useful tool for analysis of metal forming processes [1,2,3,4,5]. Recent progress in FEA, together with increasingly powerful computers, has permitted increased use of such numerical modeling. Hence, today it is possible to FEM-simulate the metal forming processes at various design stages. When a FEM model has been made for a

[a] *Technical University, Faculty of Materials Engineering and Environment, B-dul Muncii 103-105, Cluj-Napoca, Romania*

** Corresponding author e-mail: mariana.pop@ipm.utcluj.ro*

[b] *Babes-Bolyai University, Faculty of Physics, M. Kogalniceanu No. 1, 400084, Cluj-Napoca, Romania*

particular forming application, the load requirement, velocity, strain rate, strain and stress fields, etc., can easily be obtained for the considered process. FEA has significantly improved the standard of engineering design and the methodology of the design process in many industrial applications. It has substantially reduced the time required to get products from concept level to production line. Process simulation using FEA has yielded considerable cost and quality improvements in the industry.

The FE method allows the user to incorporate in the simulation: the tool and workpiece temperatures, the heat transfer during deformation, strain-rate-dependent material properties, strain hardening characteristics, and capabilities for microstructure analysis. This results in a more accurate analysis of the forging process. Commercial FE software packages have been used successfully in simulating complex two-dimensional(2-D) and three-dimensional (3-D) forging operations.

Extrusion is a deformation process used to produce long, straight, semifinished metal products such as a bar, solid and hollow sections, tubes, wires, and strips. The starting material is usually a cylindrical, cast, or previously extruded or rolled billet that is placed into a container and pressurized, by means of a punch attached to the ram of a hydraulic or mechanical press [5].

Aluminum and aluminum alloys are probably the ideal materials for extrusion. Most commercially available aluminum alloys can be extruded, and any shape can be produced from easily extrudable alloys. Aluminium alloy, AA7075, is one of the most used high-strength materials for aircraft structural components. Among common wrought aluminium alloys, it is considered as the most difficult to extrude[6]. The alloy has a very small extrusion window, as restrained by its high flow stress and by its low incipient melting point.

The progress in computer hardware and simulation tools has, in recent years, enabled complicated simulations of industrial forming processes. However, the accuracy of such simulations will remain dependant on the reliability of the material data, most important of all the true flow stress. Experimental tests at different strains, strain rates and temperatures reached during metal forming application are performed to reveal this constitutive relationship, which relates the deformation behavior to stress.

The present study employs FORGE 3D finite element code to predict the force evolution throughout the whole cycle of extruding a AA7075 billet.

THEORETICAL ASPECTS

FEM simulation of metal forming is highly complex and computation intensive. This is due to extreme nonlinearities because of large strains, plastic flow of anisotropic materials, with interfacial friction between irregular-shaped surfaces

under changing contact. Because of this, it is difficult to obtain analytical to such problems for quantitative evaluation of temperature, stress, and strain distributions, within the deforming body. It is therefore common to use the FEM for this purpose.

Constitutive equations are used to describe the changes in strength observed to occur in materials being deformed. These formulations are empirical and relate changes in strength produced by variation in strain, temperature or strain rate. Such equations are used to predict forces, distortions, stresses, etc. that can be encountered during mechanical processing of materials.

The techniques for extrusion of different materials are dependent, to a large extent, on the extrusion temperature. The essence of hot working is to reduce the yield stress and thus increase extrusion speed for a given press force. An important advantage of extrusion is that it produces compressive and shear forces in the billet; no tensile force is produced, which makes high deformation possible. Figure 1 present the forward extrusion principle.

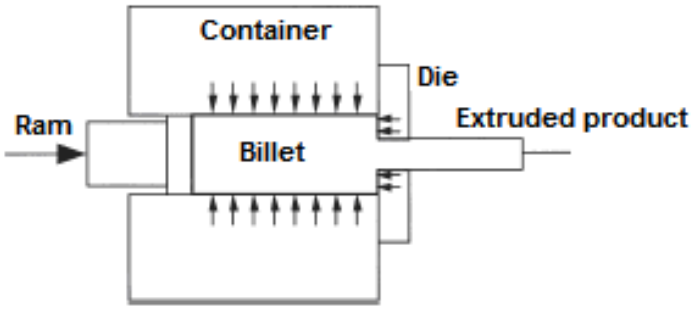

Fig. 1. Forward extrusion principle

Forge is a commercial software developed at CEMEF, Ecole des Mines de Paris and is used for the analysis of plastic deformation processes. The program is based on the finite element method for cold and hot metal forming. It enables the thermo-mechanical simulation of the plastic deformation processes of metals in an axisymmetric, homogeneous and isotropic state of deformation and obeys the von Mises criterion. The calculations of the metal flow, stress field, strain, strain rate and temperature are conducted on the assumption of the viscoplastic model of the deformed body.

The tensorial form of the Norton-Hoff law used in **FORGE 3®** is written as:

$$s = 2A(T, \bar{\varepsilon}, \ldots)(\sqrt{3} * \dot{\bar{\varepsilon}})^{m-1} \dot{\varepsilon} \quad (1)$$

$$A(T,\bar{\varepsilon}) = A_0 * (\bar{\varepsilon} + \bar{\varepsilon}_0)^n * e^{\frac{\beta}{T}} \quad (2)$$

Where ***s*** is the deviatoric stress tensor, A is the consistency of material, $\bar{\varepsilon}$ the equivalent strain, m the strain rate sensitivity, $\dot{\varepsilon}$ the equivalent strain rate, β material constant, n the strain hardening index and $\bar{\varepsilon}_0$ is a small constant.

The flow formulation introduced by Hensel and Spittel is written as:

$$\sigma = A * e^{m_1 T} * T^{m9} * \varepsilon^{m2} * e^{m4/\varepsilon} * (1+\varepsilon)^{m5T} * e^{m7\varepsilon} * \dot{\varepsilon}^{m3} * \dot{\varepsilon}^{m8T} \quad (3)$$

Where $m_{1...9}$ are sensitivity parameters.

The extrusion process parameters including die geometry and ram speed has an important influence on material flow during the deformation. The material flow affects the product quality (structure and properties) and the extrusion load. The material flow pattern is influenced by local friction conditions and die geometric shape. These aspects influenced the size of the dead zone in the material. In order to limit the friction force, die and ram has to be designed with appropriate dimensions. The friction during the extrusion process has a high influence on the occurrence of defects in the extruded products. Due to friction forces between billet and die, the material on the inside tends to move faster than the outside.

SIMULATION DETAILS

A schematic illustration of the forward extrusion process is presented in figure 2.

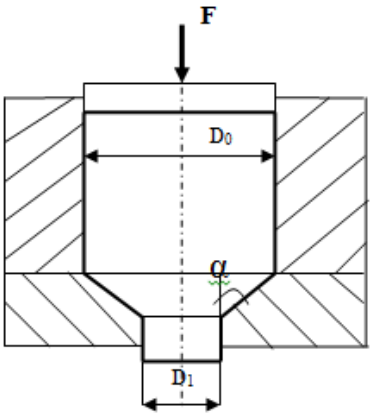

Fig. 2. Schematic illustration of the forward extrusion process

A simulation of the extrusion process was performed using the finite element software. This was achieved by constructing an accurate three dimensional CAD model of the process. The model was meshed with appropriate elements and material properties and boundary conditions were added. The geometries of the billet, die, container and ram were generated in SolidWorks and the meshes within their space domains in FORGE 3D. The physical properties of the aluminium alloy used in the computer simulation are given in Table 1. The billet was considered thermo-viscoplastic while the tools rigid, and both of these material models neglected the elastic deformation. The shear-type friction conditions at the workpiece and tooling interfaces were imposed as part of the boundary conditions. The friction factor, according to Tresca friction law, at the billet–die interfaces were assumed to be 0,3.

Table 1

Properties	Material AA7075
Density (kg/m^3)	2800
Heat capacity (N/m^2 ^{0}C)	2,39
Thermal conductivity (W/mK)	180
Emissivity	0,05

The process parameters used in the simulations are given in Table 2.

Table 2

Billet height [mm]	30
Billet diameter [mm]	30
Die semi angle α [^{0}]	60,70,80,90
Extrusion ratio	2,4,6
Billet temperature [^{0}C]	450
Container and die temperature [^{0}C]	250,300,400
Ram speed [mm/s]	2,4,6
Friction factor at the workpiece–die interface	0,3

The geometries of the billet, die, container and ram were generated in SolidWorks and the meshes within their space domains in FORGE 3D. Fig. 3 shows the initial meshes of the billet and the tooling, together with a cross-section cutting through the die. The die had a rotational symmetry, which allowed one-quarter of objects to be modelled in order to save computing time.

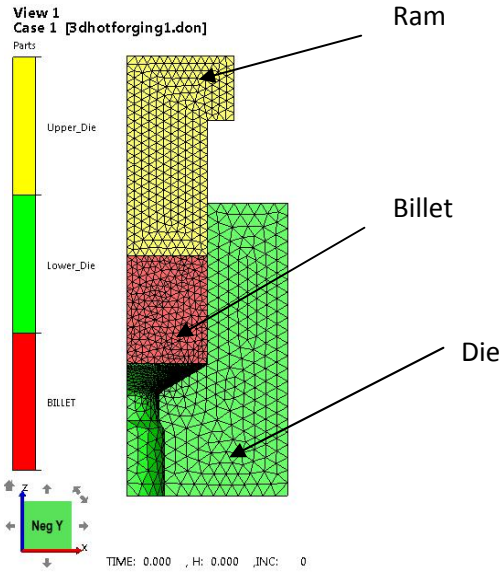

Fig. 3. Initial meshes of the billet, container, die and ram and the cross-section of the die (one-quarter of the objects)

SIMULATION RESULTS

The results obtained for strain and extrusion force distribution in different extrusion conditions are presented in figures below.

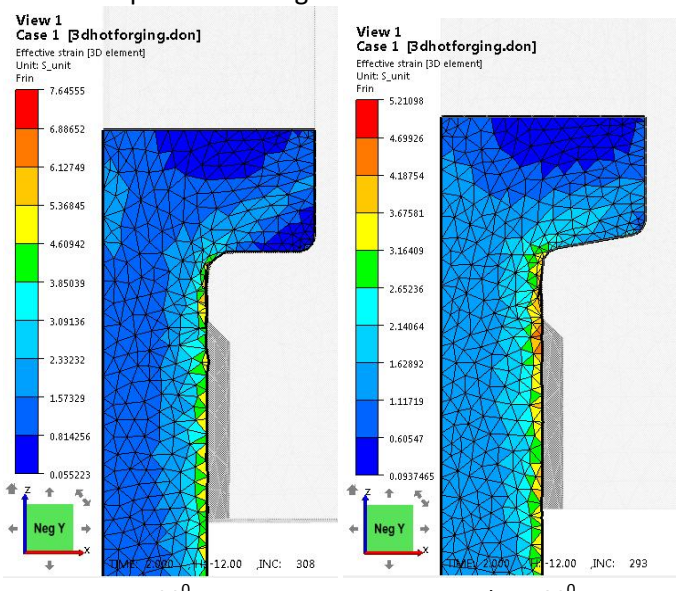

a. $\alpha=90^0$ b. $\alpha=80^0$

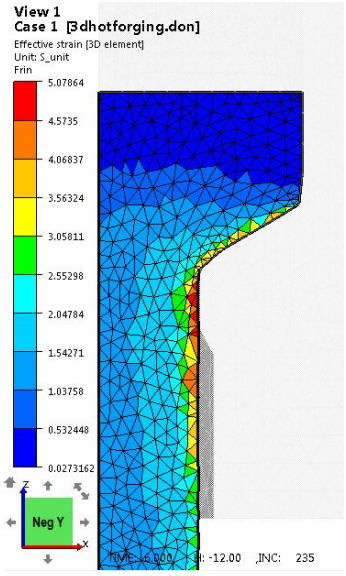

c. $\alpha=60^0$

Fig. 4. Effective strain distribution for different die angles, ram speed 2mm/s, die land diameter 15 mm

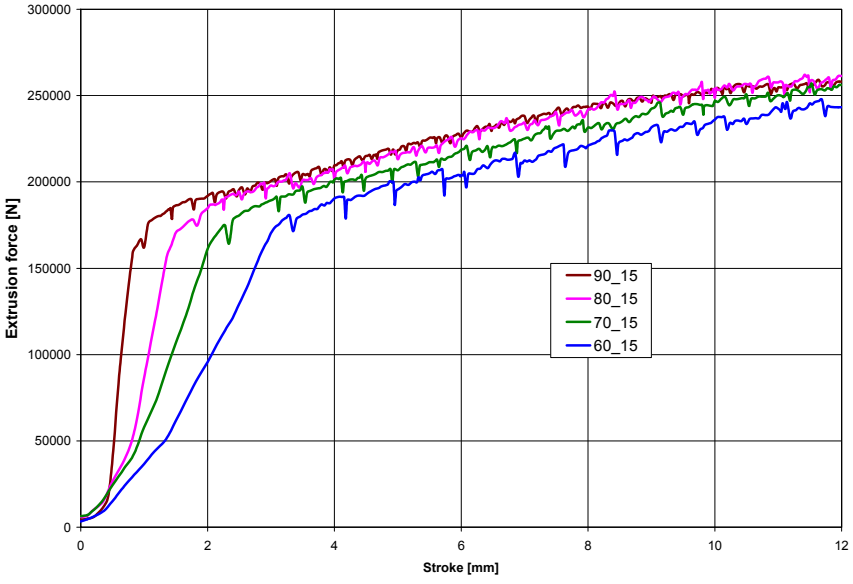

Fig. 5. Extrusion force distribution for different die angles, ram speed 2 mm/s; die land diameter 15 mm

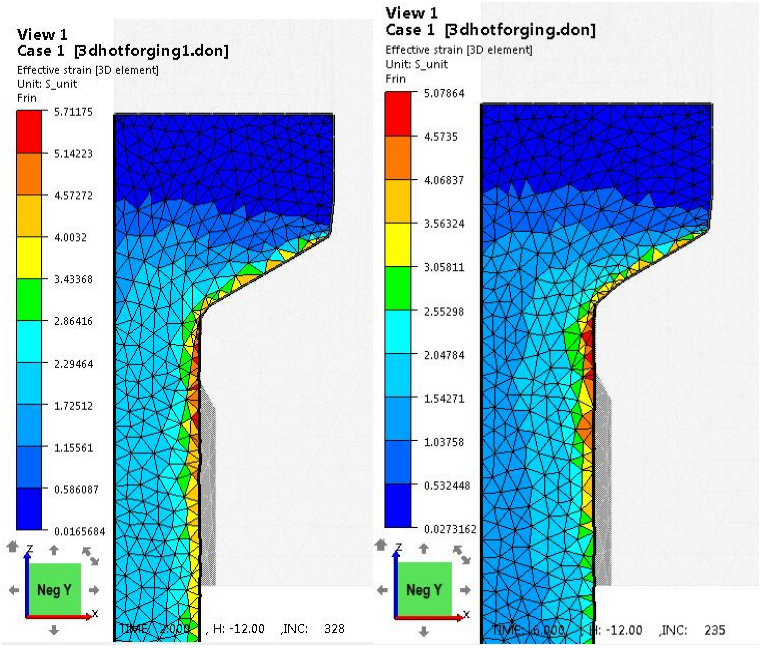

a. d=12mm b. d=15 mm

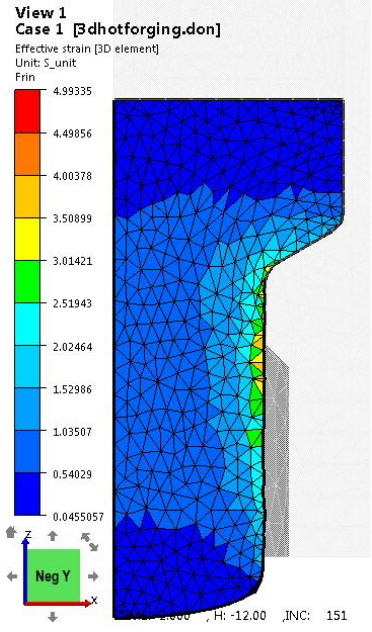

c. d=20 mm

Fig. 6. Effective strain distribution for die angle 60^0, ram speed 2mm/s, different die land diameter

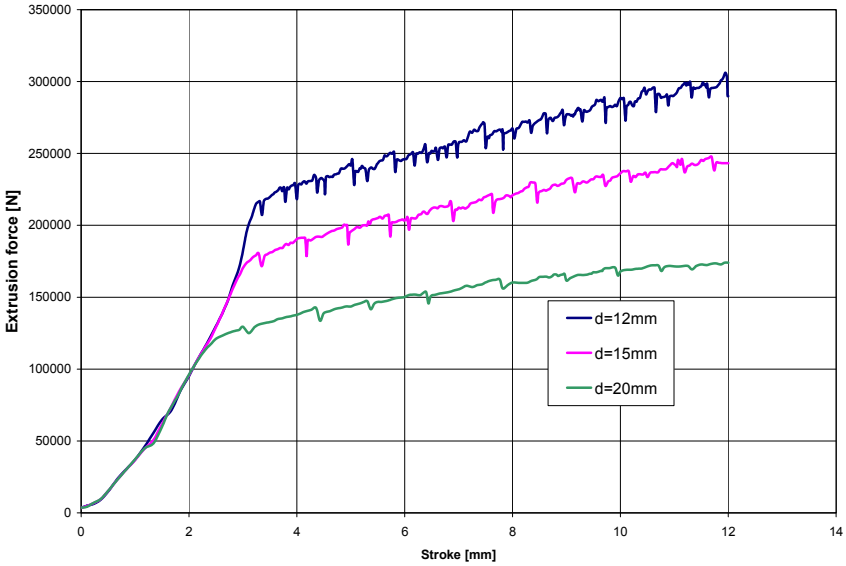

Fig. 7. Extrusion force distribution for different die lands diameters, die angle 60^0, ram speed 2 mm/s

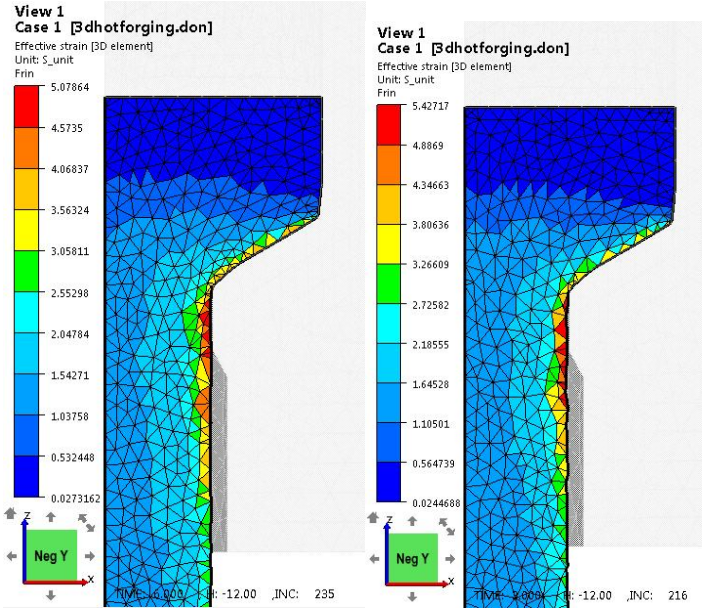

a. v=2 mm/s b. v= 4 mm/s

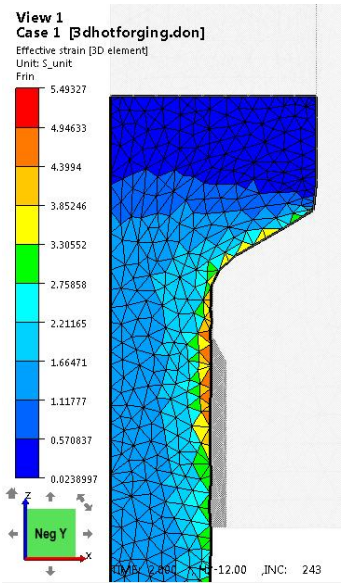

c. v= 6 mm/s

Fig. 8. Effective strain distribution for die angle 60^0, die land diameter 15 mm and different ram speed

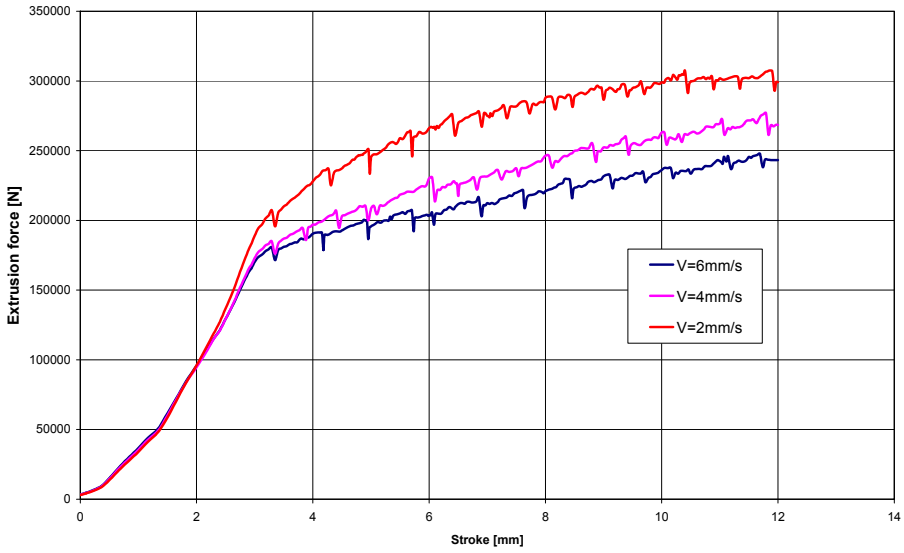

Fig. 9. Force distribution for different ram speed, die angle 60^0, die land diameter 15 mm

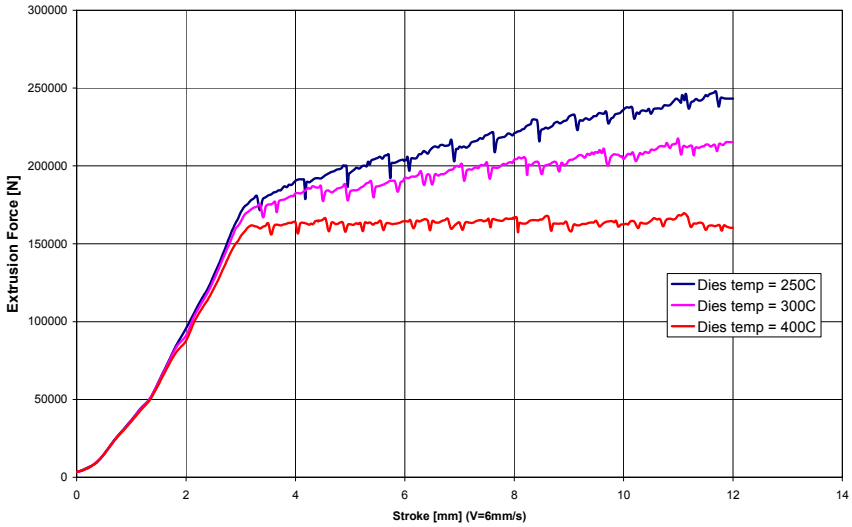

Fig. 10. Force distribution for different dies temperature, die angle 60^0, die land diameter 12 mm

CONCLUSIONS

Figures 4, 6 and 8 presents the effective strain distribution for different deformation conditions. Die geometry and ram speed has a significant influence on uniform deformation. The deformation, in terms of the effective strain distribution inside the partial extruded billet, was computed by the simulation model. These figures reveals that the deformation, quantified as effective strain, is small in the core of the billet ($\bar{\varepsilon}$< 1) and considerably larger in the surface layer of the billet ($\bar{\varepsilon}$ >3), where the shear zone is present. For a die angle $\alpha = 90$ °, there are present large dead zones (with no plastic deformation) and a nonuniform material flow due to high friction between billet and container and billet and die. By reducing the die angle to 80^0 and 60^0 the deformation in the section became more uniform (Fig. 4).

The effect of the die semi-angle on the extrusion force is presented in Fig. 5. The extrusion force increased as the semi-angle increased from 60^0 to 90^0. Die land diameter (extrusion ratio) has also an important influence on the extrusion force. Figure 7 shows that by increasing the die land diameter from 12 mm to 20 mm (decreasing the extrusion ratio) the extrusion force decrease too.

The influence of ram speed on extrusion force is presented in figure 9. To make best use of the force capacity of the press and to approach the highest possible extrusion speed without leading to extrusion defects caused by incipient melting at

around 550 ^{0}C, it is necessary to select an optimum ram speed at a given billet temperature. In practice this goal is obtained by running extrusion trials at various ram speeds within the press force capacity until the observable defects appear on the extrudate surface. Then the ram speed is set somewhat lower.

An overall concluding remark is that the FEA has proved to be useful for the investigation of the nature of the metal flow in forward hot Al extrusion. The study has led to new insight regarding what conditions control the material flow.

REFERENCES

[1] Fietier N., Krahenbuhl Y., Vialard M., New methods for the fast simulations of the extrusion process of hot metals journal of materials processing technology (2008).
[2] Li L., Zhou J., Duszczyk J., Prediction of temperature evolution during the extrusion of7075 aluminium alloy at various ram speeds by means of 3D FEM simulation, Journal of Materials Processing Technology 145 (2004) 360–370.
[3] Tiernan T., Hillery M.T., Draganescu M., Gheorghe M., Modelling of cold extrusion with experimental verification, Journal of Materials Processing Technology 168 (2005) 360–366.
[4] Dyi-Cheng Chen, Sheng-Kai Syu, Cing-Hong Wu, Sin-Kai Lin, Investigation into cold extrusion of aluminum billets using three-dimensional finite element method, Journal of Materials Processing Technology 192–193 (2007) 188–193.
[5] Uyyuru R.K., Valberg H., Physical and numerical analysis of the metal flow over the punch head in backward cup extrusion of aluminium, Journal of Materials Processing Technology 172 (2006) 312–318.
[6] Sheppard T., Extrusion of Aluminium Alloys, Kluwer Academic Publications, Dordrecht 1999, p. 239.
[7] Valberg, H., Applied metal forming including FEM analysis, Cambridge University Press, 2010.

STUDIA UBB PHYSICA, Vol. 59 (LIX), 1, 2014, pp. 59-72
(RECOMMENDED CITATION)

INVESTIGATION OF HANDMADE FERROFLUIDS' MOTION IN A VENTILATED CAVITY USING COMPUTATIONAL FLUID DYNAMICS

AMIR JAVAD AHRAR[a], MOHAMAD HASSAN DJAVARESHKIAN[b], VALI KALANTAR[c]

ABSTRACT. In this research, some more applicable ferrofluids are produced and their mechanical specifications are measured, experimentally. Also, their treatments in the ventilated cavity geometry are assessed numerically. The magnetite nanoparticles are produced by a chemical combination of Fe^{2+} and Fe^{3+} with NH_3, the black deposit of Fe_3O_4 nanoparticles will be produced. In order to dissolve the nanoparticles in the new mediums, a proper coating should be added to them. In this case the oleic acid is the hydrophobic surfactant; which is added to the particles while their mixture with water was heated. Then they are dissolved in kerosene, brake oil, hydraulic oil and the motor oil with different particle fractures. A pressure-based procedure to solve Navier-stokes equations with finite volume formulation is developed to simulate a magnetic fluid in ventilated cavity geometry. One of the usages of this geometry is found in magnetic separation. The ventilated cavity geometry includes a square medium with one velocity inlet and one velocity outlet. In addition, a magnetic field due to a DC current carrying wire is employed on the geometry. The magnetic field intensities, its positions and ferrofluids' mediums are changed. Then, the flow characteristics for each case are obtained to find the optimum situation for magnetic separation.

***Key Words**: Ferrofluid, CFD, ventilated cavity*

INTRODUCTION

Ferrofluid or magnetic fluid is an over growing topic for mechanical engineers in the current decade. Ferrofluid is a type of fluid which absorbs to a magnetic field source; it means that when a ferrofluid is exposed to a magnetic

[a] *Ph.D. Student, Ferdowsi University of Mashhad, am_ah47@stu-mail.um.ac.ir*
[b] *Associate professor, Ferdowsi University of Mashhad, javareshkian@um.ac.ir*
[c] *Assistant of professor, Yazd University, vkalantar@yazduni.ac.ir*

field source, some pikes will be developed in the magnetic field lines directions. Generally, magnetic particles are divided into two groups: Hydrophobic and hydrophilic particles. The hydrophobicity of ferrofluids is usually due to the surfactant which is used to stabilize the magnetic nano particles in the liquid carrier as well. In the case that the surfactant is polar the nano particles would be dissolved in polar solvents like water but if the surfactant is nonpolar, they would dissolve in nonpolar surfactants like oil thus the ferrofluid becomes hydrophobic.

Magnetic fluids' industrial background comes back to 1940. In that time magnetic fluids – with particle size of a few microns – were used in magnetic clutches. In 1960 ferrofluids with nano sized particles were produced on behalf of NASA. The aim was to produce a magnetic nano particle which can be solved in space craft fuel so the movement of the fuel could be controlled in the space (A gravity free place).

Thereafter, ferrofluids were used as a non porous seal. Also with the aid of these fluids, high quality load speakers were produced. This technology annually is being applied in more than 100 million load speakers. In medicine, magnetic fluids are used as contrast agents for Magnetic Resonance Imaging and can be used for cancer detection. They are in this case composed of iron oxide nanoparticles and called SPION, for "Super paramagnetic Iron Oxide Nanoparticles". There is also much experimentation with the use of ferrofluids in an experimental cancer treatment called magnetic hyperthermia. It is based on the fact that if this kind of fluid is placed in an alternating magnetic field it releases heat [1].

Academic researches have reached to the highest level in the last decade. Some tried different methods for solving the flow equations like two phase solutions or lattice Boltzmann methods [2, 3]. Some other papers refer to different geometries like cavity, Journal bearing or micro channels [3-8] and some of them used different magnetic field sources like permanent magnet or a magnetic dipole [9, 10]. In the case of simple geometries, In 2003 Chang et al. presented a paper on the stability of ferrofluid flow between two concentric cylinders. In his work the mentioned fluid was exposed to a magnetic field and so the specifications of flow were estimated [11]. In 2005, Rhodes et al in an experimental work placed a droplet of ferrofluid in a Hele - Shaw cell then the droplet was exposed to different magnetic fields. Due to the different magnetic field types and strengths, different shapes of magnetic droplet were obtained [10]. In March of 2006, Jue presented an investigation of ferrofluid flow in cavity geometry. In his work convective forces and the force due to a magnetic field source were combined [12]. Rinaldi et al studied magnetic fluid flow between two concentric cylinders to investigate the magneto viscosity of ferrofluids [13]. He could reach to zero magneto viscosities for certain magnetic fields. Singh and Bajaj also used this geometry to estimate ferrofluid stability [14].

Although fine works have been done on this kind of fluid, there are still some points which need to be discussed. Most of working ferrofluids are based on kerosene or water. These mediums can reduce their applicability in a lot of industrial purposes. Also a vast number of papers are investigating ferrofluids' behavior in situations in which low density fluids can not be applied e.g. magnetic seals. So in this work we tried to produce some more applicable ferrofluids and then their mechanical specifications were measured, experimentally. Afterward, the ventilated cavity geometry was solved via CFD methods using these new ferrofluids' specifications.

GOVERNINC EQUATIONS

In order to determine ferrofluids' behavior in the presence of a magnetic field, the continuity and enhanced Navier-Stokes equations are used:

$$\nabla.V = 0 \tag{1}$$

$$\rho\frac{dV}{dt} = -\nabla P + \rho g + \mu\nabla^2 V + \mu_0 M.\nabla H \tag{2}$$

In the above equations: μ, μ_0, M and H are referred to fluid viscosity, air permeability, magnetization of ferrofluid and the magnetic field intensity, respectively. Actually the only term which is added to the familiar Navier-Stokes equations is the last term of equation 2 ($\mu_0 M.\nabla H$). As we know the conservation of mass equation does not change, because the final result of the steady state flow should satisfy the mass conservation condition. But the momentum of the flow would vary due to the magnetic forces. The non dimensional forms of these equations in the Cartesian coordinate system can be written as [15 and 16]:

$$\frac{\partial u^*}{\partial x^*} + \frac{\partial v^*}{\partial y^*} = 0 \tag{3}$$

$$\frac{\partial}{\partial x^*}\left(u^{*2} - \frac{1}{\mathrm{Re}}\frac{\partial u^*}{\partial x^*}\right) + \frac{\partial}{\partial y^*}\left(u^* v^* - \frac{1}{\mathrm{Re}}\frac{\partial u^*}{\partial y^*}\right) = -\frac{\partial p^*}{\partial x^*} + \beta h_m^* \frac{\partial h_m^*}{\partial x^*} \tag{4}$$

$$\frac{\partial}{\partial x^*}\left(u^* v^* - \frac{1}{\mathrm{Re}}\frac{\partial v^*}{\partial x^*}\right) + \frac{\partial}{\partial y^*}\left(v^{*2} - \frac{1}{\mathrm{Re}}\frac{\partial v^*}{\partial y^*}\right) = -\frac{\partial p^*}{\partial v^*} + \beta h_m^* \frac{\partial h_m^*}{\partial v^*} \tag{5}$$

The dimensionless variables are defined as:

$$x^* = \frac{x}{l_{in}}, \qquad y^* = \frac{y}{l_{in}}, \qquad u^* = \frac{u}{U_{in}}, \qquad v^* = \frac{v}{U_{in}}, \qquad p^* = \frac{p}{\rho U_{in}^2},$$

$$\mathrm{Re} = \frac{\rho U_{in} l_{in}}{\mu}, \qquad \mathrm{h}_\mathrm{m}^* = \frac{h_m}{h_{mo}}, \qquad \beta = \frac{\mu_0 \chi_m (h_{mo})^2}{\rho U_{in}^2}$$

Here, l_{in} refers to the entrance length; U_{in} is the inlet velocity, h_{mo} is the characteristic value of magnetic field intensity and ρ, μ, μ_0 are referred to the density, viscosity and the gap magnetic permeability, respectively. In the rest of this text, the superscript of * is deleted for simplicity, while all the used parameters are nondimensional.

In order to solve this set of equations, next step is to calculate h_m. In this paper, a wire was used as a magnetic field source. It's known that the magnetic field intensity is a function of the magnetic field strength and the distance between the particles and the magnetic source. In this case, the magnetic field strength is proportional with the current of the wire. The field lines would be concentric circles with the wire at their center. So the magnetic field intensity for any point on the geometry is calculated by this equation:

$$h_m(x, y) = \frac{I}{2\pi\sqrt{x^2 + y^2}} \tag{6}$$

Here, I represents the current intensity of the wire and x and y are the dimensionless coordinates. Thus the value of h_m is neither a function of the fluid velocity nor time, so it will remain constant during the solving processes.

EXPERIMENTAL MEASURMENTS

The magnetite nanoparticles were produced by a chemical combination of Fe^{2+} and Fe^{3+} with NH_3, the black deposit of Fe_3O_4 nanoparticles will be produced. In order to dissolve the nanoparticles in the new mediums, a proper coating should be added to them. In this case the oleic acid was the hydrophobic surfactant; which was added to the particles while their mixture with water was heated. Then they were dissolved in kerosene, brake oil, hydraulic oil and the motor oil with different particle fractures (figure 1).

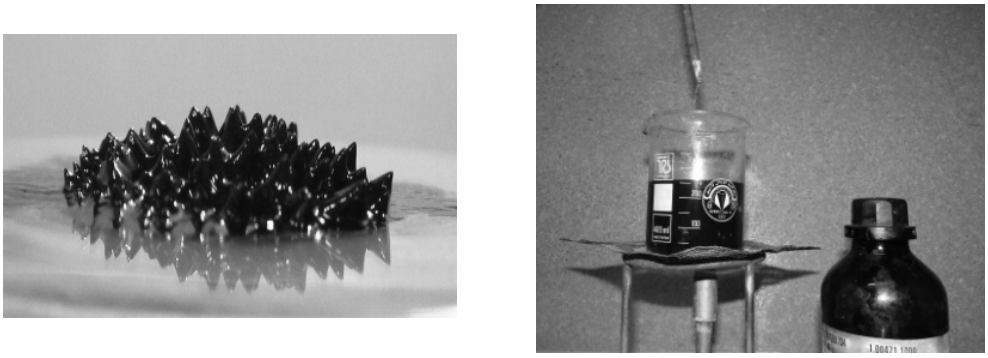

Fig. 1. ferrofluid based on hydraulic oil

The effect of both density and cinematic viscosity of these four ferrofluids are measured. In order to measure the cinematic viscosity of each ferrofluid a Cannon-Fenske Transparent Viscometer (CFR) was applied. This viscometer has a glass tube and an oil bath (figure 2). When this tube is filled with ferrofluid, the exit time can be measured. There is a table enclosed to this device which is calibrated for temperature and from it, the cinematic viscosity versus time can be obtained.

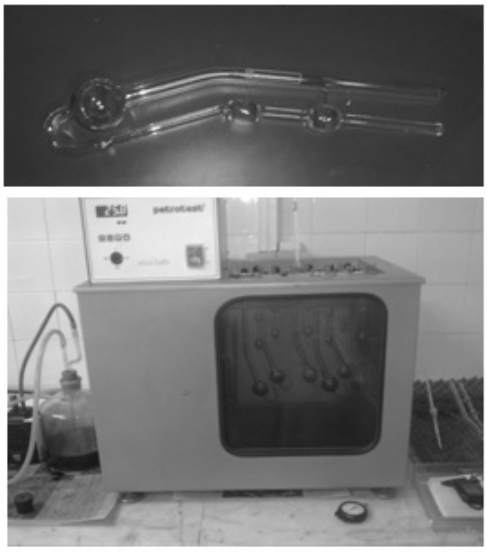

Fig. 2. Cannon-Fenske viscometer and the oil bath

The measured cinematic viscosities for the ferrofluids are presented on table 1. As can be seen, the motor oil and kerosene have the maximum and minimum cinematic viscosities, respectively. These viscosities will be used in the CFD code as an identifier for the medium changes.

Table 1.

Cinematic viscosity for different handmade ferrofluids

Medium fluid	***cinematic viscosity***
kerosene	*11.493 mm^2/sec*
Hydraulic oil	*84.544 mm^2/sec*
Brake oil	*62.615 mm^2/sec*
motor oil	*256.274 mm^2/sec*

RESULTS AND DISCUSSION

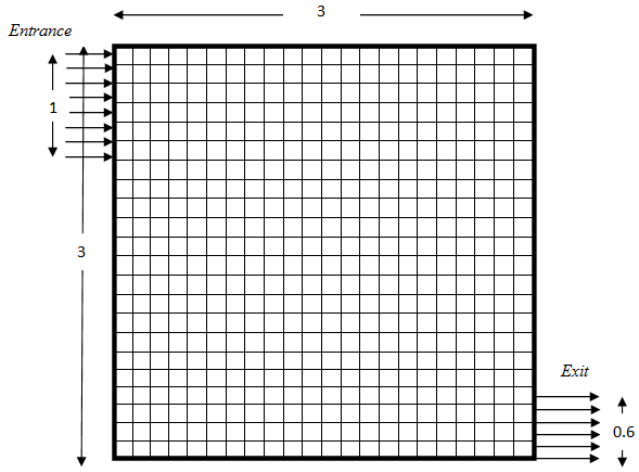

Fig. 3. the Geometry of the solution with 1 entrance and 1 exit.

It is worth mentioning that all the parameters in this study are Nondimensional. As shown in figure 3, the geometry which is solved is a 3*3 cavity with 1 entrance and 1 exit. The entrance and the exit width are 1 and 0.6, respectively. The velocity at the entrance is assumed to be 1(dimensionless) and the no slip condition is applied to all walls. A 100*100 mesh was generated and the Control Volume method was applied to solve the enhanced Navier Stokes equations on the geometry. The mesh independence test is shown in Fig. 4. As can be seen the results for two meshes 100*100 and 120*120 are the same. To verify the numerical simulation, the results of v velocity in the horizontal middle section of a lid-driven cavity are compared with [17, 18]. These comparisons verify the present numerical simulation

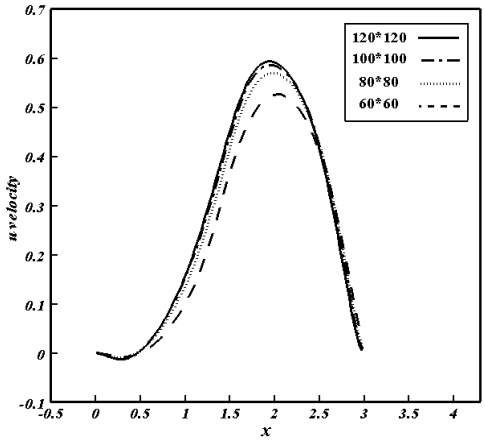

Fig. 4. mesh independence results

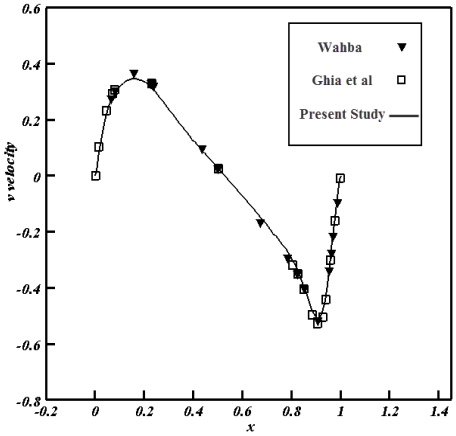

Fig. 5. Comparison of the present results with [17, 18]

The admixture of fluid is a significant factor in many industrial applications e.g. magnetic separation. In this study, the mentioned parameter for different Re Numbers is assessed.

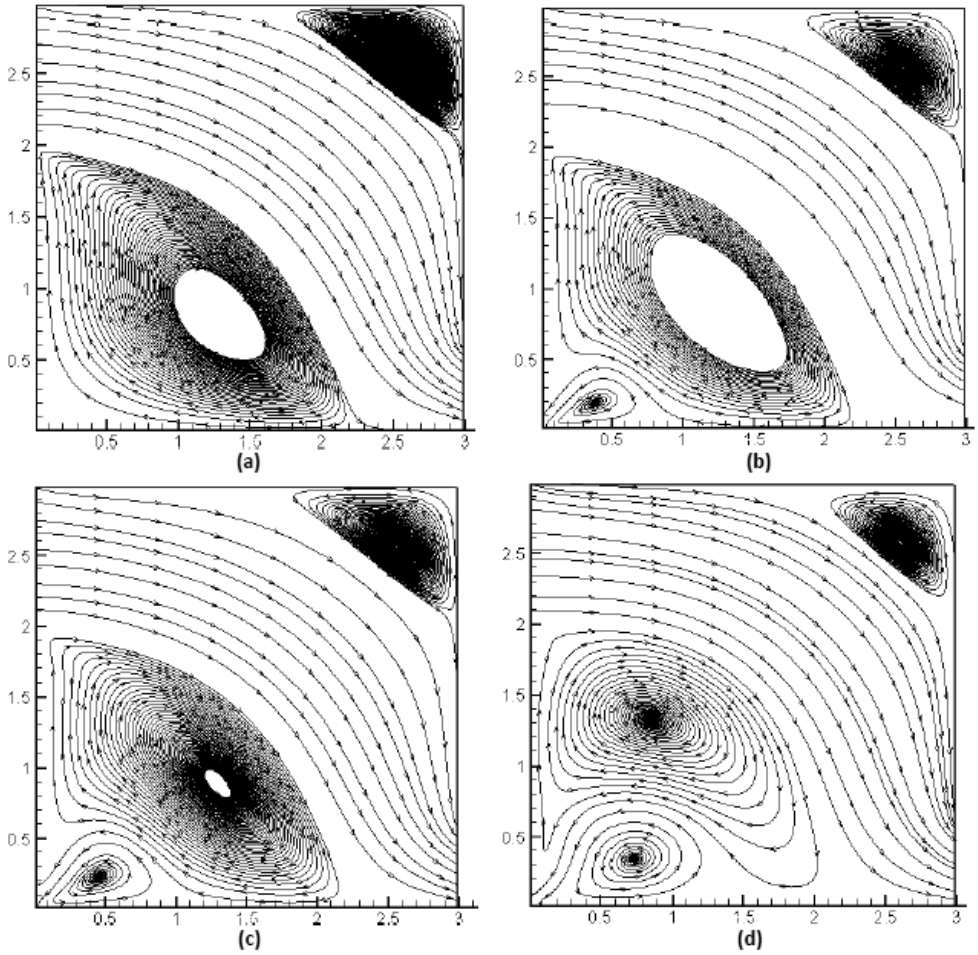

Fig. 6. the stream lines of the flow for a certain ferrofluid (Kerosene-based) for different magnetic field intensities. H_m for a = 0, b = 0.67, c = 0.8 and d = 1.

First of all, the position of wire - the source of the magnetic field - is considered to be fixed on the bottom left corner of the cavity and the ferrofluid is based on Kerosene. The results for the magnetic field intensities H_m = 0, 0.67, 0.8 and 1 are presented in Figs 6 a-d.

As it can be seen, in the case of no magnetic field there are two main vortexes on the whole region. As the magnetic field intensity starts to grow, a third vortex begins to grow as well. This can provide a very fine local mixing enviroment with respect to the entrance and exit.

On the second attempt, the ferrofluid mediums were changed. The most famous mediums for ferrofluids are water and kerosene. But as mentioned before, due to their low density and viscosity and also the corrosion effects of water, they can not provide wide range of mechanical applications. So the new hand made ferrofluids were tested under the same conditions. In this case, the magnetic field source is fixed on the right bottom corner with an intensity of 0.67 for all cases and the results are demonstrated for different mediums (figure 7).

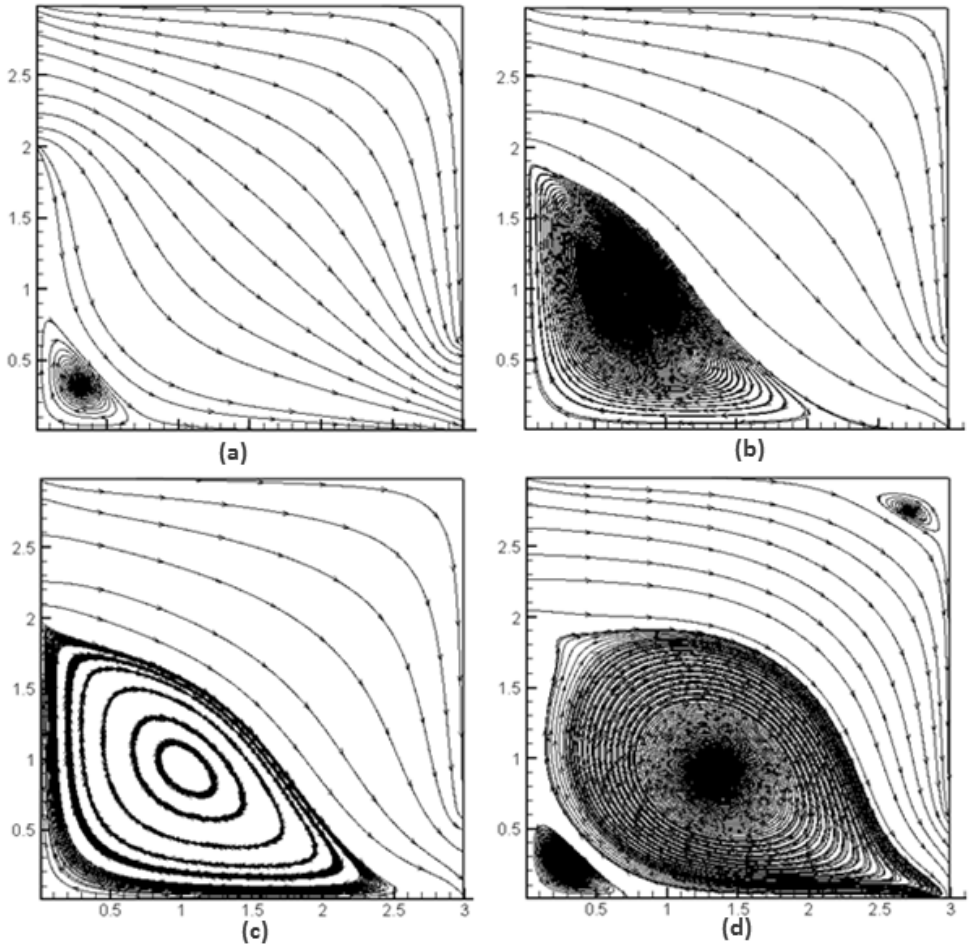

Fig. 7. the stream lines of the flow for the handmade ferrofluids based on:
a. Motor oil, b. Hydraulic oil, c. Brake oil and d. Kerosene.

Here, figure 7-a is in the case of Motor oil-based ferrofluid. As can be seen in this case the main vortex is so smaller than all other mediums. Thus the fluid flow can be assumed laminar in most regions of the geometry. This, in return, will provide higher pressure field on the system. On the other hand the biggest vortex is for the case of kerosene-based ferrofluid (figure 6-d). Although it provides better mixing than the others, but regarding to its poor mechanical properties and its flammability, the Hydraulic oil and Brake oil may be considered for different purposes as well.

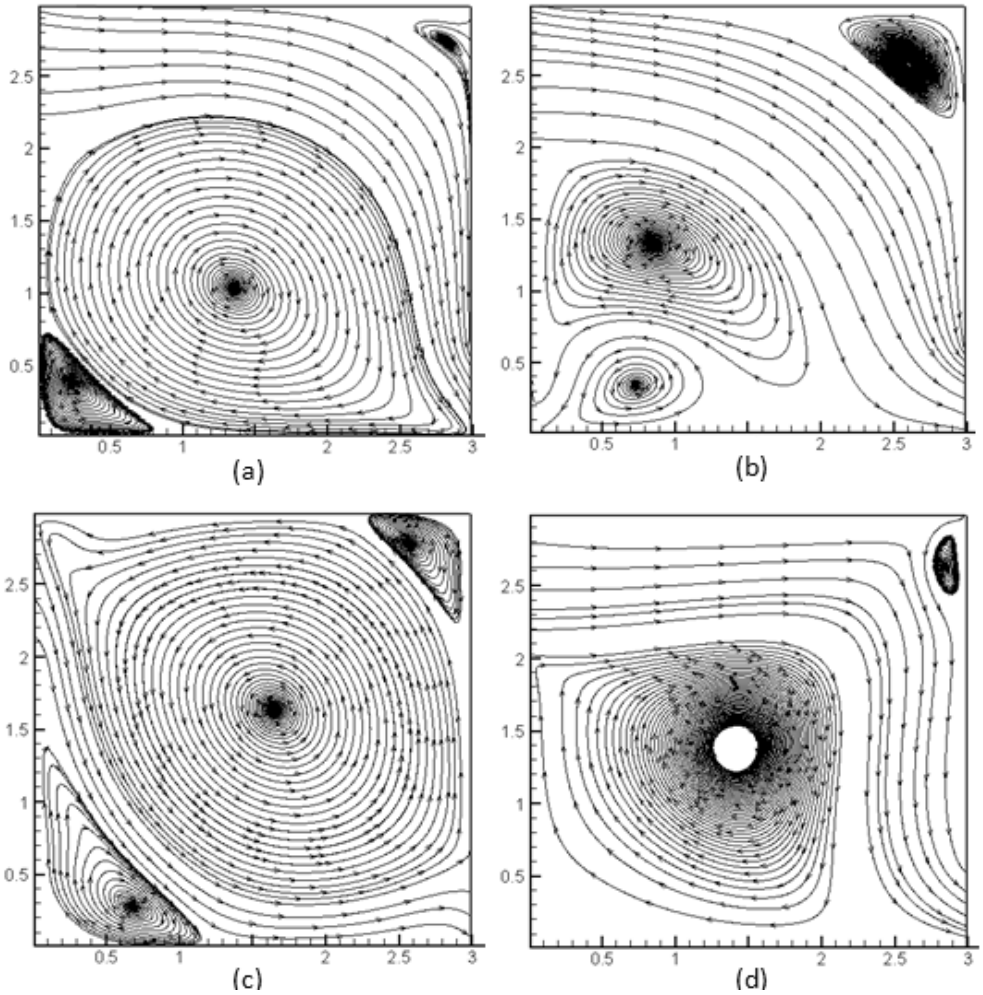

Fig. 8. stream lines changes due to the change in the location of the magnetic source for a certain ferrofluid (Kerosene-based) where the magnetic field sources are located on a. the right-bottom corner, b. the left-bottom corner, c. the left-upper corner and d. on the right-upper corner of the cavity

Finally, four different locations for the magnetic field source were chosen for particular magnetic field intensity and Re. Figure 8 presents the stream lines of each case throughout the cavity. These locations are at a) the left-bottom corner, b) the right-upper corner, c) the right-bottom corner and d) the left-upper corner of the cavity.

Figure 8 basically, shows that any changes in the place of the magnetic field source will have a direct effect on the ferrofluid flow. In the cases of 8-a and 8-c, it can be seen that the lower vortex is extended and it has almost filled the whole region. With a more precise look at these cases, we will recognize that the flow in the case a passes *on* the vortex while in the case c it is driven *under* the vortex due to the magnetic field. Also as mentioned before, the 8-b and 8-d positions are considered for local mixings; in which, case 8-b can be assumed to work more efficiently because of its extra vortex. Also the velocity profiles for each case are presented on figure 9.

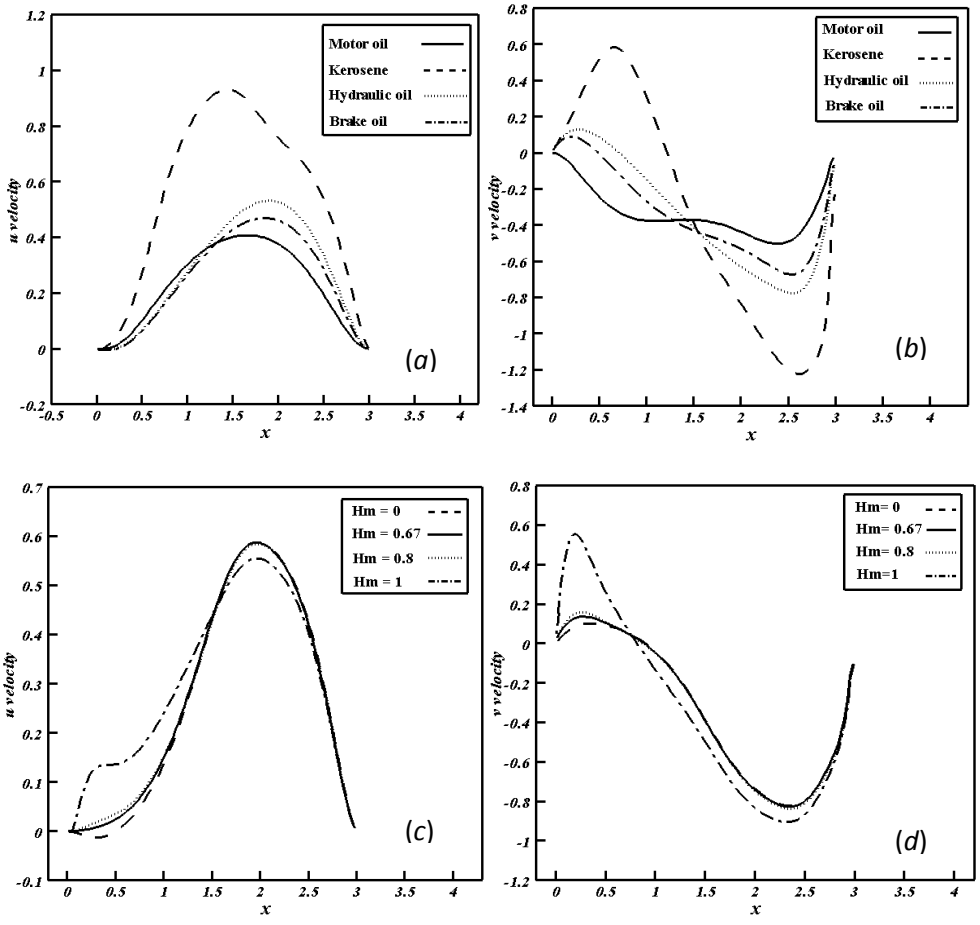

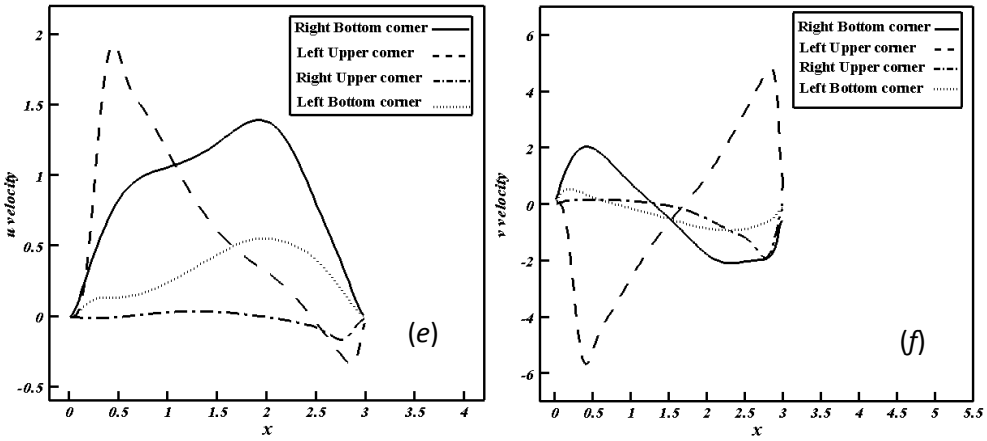

Fig. 9. *u* and *v* velocity profiles for each case. *(a, b)*: For Four different based handmade ferrofluids, *(c, d)*: For different Magnetic field intensities for kerosene based ferrofluid and *(e, f)*: For different positions of magnetic field source for kerosene based ferrofluid with a fixed intensity.

In figure 9, the *u* and *v* components of the velocity are plotted for: *a, b* different mediums, *c, d* different magnetic field intensities and *e, f* for different magnetic field source positions. As can be seen on figure 9-a and 9-b the maximum change in the velocity profiles is for the kerosene and the minimum is for the motor oil based ferrofluid.

In figure 9-c and 9-d the changes of the velocity profiles due to the increase of the magnetic field intensity is presented. And in cases 9-e and 9-f the effect of repositioning of the magnetic field source on the fluid flow is observed. In the left – upper and right – bottom corner positions, the lower vortex extends and occupies almost the whole cavity so the maximum changes would take place in these cases. This can also be seen on the velocity profiles, where the *v* velocity amplitudes are almost four times higher than the right-upper and left-bottom cases.

CONCLUSION

The enhanced Navier – Stokes equations of magnetic fluids are solved in the ventilated cavity geometry. The results for ferrofluids' flow are obtained for different handmade ferrofluids, magnetic field source positions and intensities. These results showed that for the case of kerosene-based ferrofluids, the best circulation behavior

is observed and the motor oil-based ferrofluids could tolerate the highest pressure gradient. So the usage of these new ferrofluids can be defined per their physical specifications for different environmental situations. Also the position of left – upper and right – bottom corners showed the maximum influences of the magnetic field on the flow. In the case of the right – upper corner position, influence of the field is the least. In the case of a left – bottom corner position, 2 main vortices will appear which makes this position the best for local circulation.

ACKNOWLEDGMENTS

Hereby, we take this chance to acknowledge the Karafarini center of the University of Yazd for the financial assists. Also we will thank the Standard organizations of Yazd for the laboratory preparations and assists.

REFERENCES

[1] F.R. Cunha, Y.D. Sobral, Characterization of the physical parameters in a process of magnetic separation and pressure- driven flow of a magnetic fluid, *Physica A*, 343 (2004) 36-64.

[2] A. Jafari, T. Tynja, S.M. Mousavi, P. Sarkoma, Simulation of heat transfer in a ferrofluid using computational fluid dynamics technique, *International Journal of Heat and Fluid Flow*, 29 (2008) 1197–1202.

[3] A.A. Golneshan, M. Lahonian, Diffusion of magnetic nanoparticles in a multi-site injection process within a biological tissue during magnetic fluid hyperthermia using lattice Boltzmann Method, *Mechanics Research Communications* ,38 (2011) 425– 430.

[4] Z. Parlak, T. Engin, Time-dependent CFD and quasi-static analysis of magnetorheological fluid dampers with experimental validation*, International Journal of Mechanical Sciences*, 64 (2012) 22–31.

[5] A. Kuzmina, M. Januszewskib, D. Eskinc, F. Mostowfic, J.J. Derksen, Simulations of gravity-driven flow of binary liquids in microchannels, *Chemical Engineering Journal*, 171 (2011) 646– 654.

[6] S.M. Snyder, T. Caderb, B. A. Finlayson, Finite element model of magnetoconvection of a ferrofluid*, Journal of Magnetism and Magnetic Materials*, 262 (2003) 269–279.

[7] D.A. Bompos, P.G. Nikolakopoulos, CFD simulation of magnetorheological fluid journal bearings, *Simulation Modeling Practice and Theory*, 19 (2011) 1035–1060.

[8] C.M. Chang, W.T. Cheng, W.J. Liu, H.W. Cheng, C.E. Huang, S.W. Du, Thermal flow of fluid with magnetic particles in the presence of magnetic field, *International Communications in Heat and Mass Transfer*, 37 (2010) 801–808.

[9] R. Ganguly, S. Sen, I. K. Puri, Heat transfer augmentation using a magnetic fluid under the influence of a line dipole, *Journal of Magnetism and Magnetic Materials,* 271 (2004) 63–73.

[10] S. Rhodes, X. He, S. Elborai, S.H. Lee, M. Zahn, Magnetic fluid behavior in uniform DC, AC, and rotating magnetic fields, *Journal of ELECTROSTATICS*, 64 (2006) 513-519.

[11] M.H. Chang, C. Chen, H. C. Weng, Stability of ferrofluid flow between concentric rotating cylinders with an axial magnetic field, *International Journal of Engineering Science*, 41 (2003) 103-121.

[12] T. Jue, Analysis of combined thermal and magnetic convection ferrofluid flow in a cavity, *International communication in heat and mass transfer*, 33 (2006) 846-852.

[13] C. Rinaldi, F. Gutman, X. He, A.D. Rosenthal, M. Zahn, Torque measurements on ferrofluid cylinders in rotating magnetic fields, *Journal of magnetization and magnetic materials*, 289 (2005) 307-310.

[14] J. Singh and R. Bajaj, Couette flow in ferrofluids with magnetic field, *Journal of magnetization and magnetic materials*, 294 (2005) 53-62.

[15] H. Montazery, Numerical analysis of hydrodynamic journal bearings lubricated with ferrofluid, *IMechE*, 222 (2007) 51-60.

[16] W. Wrobel, E. Fornalik-Wajs, J.S. Szmyd, Experimental and numerical analysis of thermo-magnetic convection in a vertical annular enclosure*, International Journal of Heat and Fluid Flow,* 31 (2010) 1019–1031.

[17] U. Ghia, KN. Ghia, CT. Shin, High-Re solutions for incompressible flow using the Navier–Stokes equations and a multi grid method, *J Comput Phys*, 48 (1982) 387–411.

[18] E.M. Wahba, Steady flow simulations inside a driven cavity up to Reynolds number 35,000, *Computers & Fluids*, 66 (2012) 85–97.

STUDIA UBB PHYSICA, Vol. 59 (LIX), 1, 2014, pp. 73-82
(RECOMMENDED CITATION)

MACROSCOPIC ANALYSIS OF THE INTERIORS OF TWO NEUTRON STARS

Ş. ONŢANU-CRĂCIUN[a], A. MARCU[a], N. MAGYAR[a]

ABSTRACT. In this paper we have studied the interiors of the neutron stars KS1731-260 and EXO 1745 248, comparing the models of Marcu & Ballai, 1994 and Pant, 2011 and applying them to the observational data of Guver et al, 2009 and 2011. The stars are treated in the approximation of static, spherically symmetric balls of electrically-neutral perfect fluid. We have calculated and plotted the pressure, density, adiabatic sound speed, gravitational acceleration and gravitational potential for each model and star and interpreted the results. Comparing with the model of Tolman, 1939, we have found anomalous behaviors of the gravitational acceleration and potential in the central regions of the stars, attributed to the mathematical assumption of infinite central density in the studied models.

Keywords: *General Relativity, neutron stars, perfect fluids*

INTRODUCTION

Owing to the nonlinearity of Einstein's Field Equations, there have been many attempts to obtain exact solutions of representing the interiors of static balls of perfect fluid in equilibrium, such as Tolman [1], Wyman [2], Kuchowich [3], Pant and Sah [4], D.N. Pant and N. Pant [5], Pant [6, 7], Pant [8], Delgaty, Lake [9], Lake [10], Tewari and Pant [11] and Maurya, Gupta [12]. In the first section we present the Einstein Field Equations for perfect fluids and, in short, the models of Marcu & Ballai, 1994 [13] and Pant, 2011 [14] and in the final section proceed to study the pressure, density, adiabatic sound speed, gravitational acceleration and gravitational potential of the interiors of two particular neutron stars of known mass and radius.

[a] *Babeş-Bolyai University, Faculty of Physics, 1 Kogălniceanu str., 400084 Cluj-Napoca, Romania*

THEORETICAL CONSIDERATIONS

In order to obtain a description of the interior of a neutron star in the perfect fluid approximation, one must solve the Einstein Field Equations for a ball of perfect fluid. The static, spherically symmetric metric in spherical coordinates is:

$$ds^2 = -e^{\nu(r)}c^2dt^2 + e^{\lambda(r)}dr^2 + r^2d\theta^2 + r^2\sin^2\theta d\varphi^2, \quad (1)$$

[1], where ν and λ are the field variables and functions of r only. The Einstein field equations for a nonempty spacetime are [1]:

$$R_{\mu\nu} - \frac{1}{2}g_{\mu\nu}R = \frac{8\pi G}{c^4}T_{\mu\nu}, \quad (2)$$

where $R_{\mu\upsilon}$ is the Ricci tensor, R is the scalar curvature and $T_{\mu\nu}$ is the energy-momentum tensor. The energy momentum tensor for a perfect fluid is defined as [1]:

$$T_{\mu\nu} = \left(\rho c^2 + p\right)u_\mu u_\nu + pg_{\mu\nu}, \quad (3)$$

where p denotes the pressure function, ρ denotes the density function and the u_μ are the 4-velocities:

$$g_{\mu\nu}u^\mu u^\nu = -1, \quad (4)$$

where $g_{\mu\nu}$ is the metric tensor. The field is static, so the only non-zero component of the 4-velocity is

$$u^0 = \frac{1}{\sqrt{g_{00}}}. \quad (5)$$

The gravitational field equations for a spherically symmetric ball of perfect fluid with pressure $p(r)$ and density $\rho(r)$ then reduce to [1]:

$$-e^{-\lambda}\left(\frac{\nu'}{r} + \frac{1}{r^2}\right) + \frac{1}{r^2} = \frac{8\pi G}{c^4}p(r) \quad (6)$$

$$e^{-\lambda}\left(\frac{\lambda'}{r} - \frac{1}{r^2}\right) + \frac{1}{r^2} = \frac{8\pi G}{c^2}\rho(r) \quad (7)$$

$$\frac{d}{dr}\left(\frac{e^{-\lambda}-1}{r^2}\right) + \frac{d}{dr}\left(\frac{e^{-\lambda}\nu'}{2r}\right) + e^{-\lambda-\nu}\frac{d}{dr}\left(\frac{e^{\nu}\nu'}{2r}\right) = 0 \quad (8)$$

where the prime denotes differentiation with respect to *r.* The solutions for $p(r)$ and $\rho(r)$ can be obtained from (6) and (7) after solving (8) for λ and ν. Marcu & Ballai, 1994 [13] and Pant, 2011 [14] each came to a different model for the interiors of static relativistic neutron stars in the perfect fluid approximation. In both articles, the authors apply certain transformations and assumptions on e^{ν} and $e^{-\lambda}$ such that equation (8) is integrable for one of them and then the other can be immediately found.

The model in [13] derives the solution in the classical way, but considers a more general energy-momentum tensor, which takes viscosity and electric charge into account. For the purpose of this paper, it has been simplified back to the case of a neutral perfect fluid. The simplified results are:

$$\frac{8\pi G}{c^4}p(r)=\frac{1}{r^2}-\frac{\tau(r)}{r^2}\left(\frac{2a\ln r+2b+2a}{a\ln r+b}+1\right) \tag{9}$$

$$\frac{8\pi G}{c^2}\rho(r)=\frac{2\tau(r)}{r^2}\frac{a\ln r+b+a}{a\ln r+b}-4Ce^{\frac{2b}{a}}\frac{a\ln r+b}{2a\ln r+2b+a}, \tag{10}$$

where:

$$a=\frac{1}{2R_*\sqrt{N}}(1-3N)$$

$$b=\frac{\sqrt{N}}{R_*}-\frac{\ln R_*}{2R_*\sqrt{N}}(1-3N)$$

$$C=(N-1)\left(\frac{2\sqrt{N}}{R_*}+a\right)R_*^{-2}e^{\frac{-2b}{a}}$$

$$N=1-\frac{2GM_*}{c^2R_*}\qquad \tau(r)=e^{-\lambda}=1+Ce^{2b/a}(2a\ln r+2b+a)^{-1}r^2$$

and M_* and R_* are the mass and radius of the star. All these constants are easily obtainable when one knows the mass and radius.

The Pant, 2011 model [14] considers the usual energy-momentum tensor of perfect fluids (3) and, making use of some arbitrary parameters, arrives at several classes of parameterized solutions. Solving (8) (see [14] for derivation), the expressions for the field variables yield:

$$e^{v}=C_1r^{a+b-2}+C_2r^{a-b-2}\qquad e^{-\lambda}=\frac{\left[Ar^{7-l}-4/(l-7)\right](C_1r^{2b}+C_2)}{(a+b)C_1r^{2b}+(a-b)C_2},$$

where:

$$C_1=\frac{(a-b-1)(1-2u)-1}{2bR_*^{a+b-2}}\qquad A=R_*^{l-7}\left[\frac{(1-2u)\left[(a+b)C_1R_*^{2b}+(a-b)C_2\right]}{C_1R_*^{2b}+C_2}+\frac{4}{l-7}\right]$$

$$C_2=\frac{(a+b-1)(1-2u)-1}{2bR_*^{a-b-2}}\qquad a=\frac{1-l}{2};\quad b=-\frac{1}{2}\sqrt{(1+l)^2-32};\quad u=\frac{GM_*}{c^2R_*}$$

and l is an arbitrary parameter. Setting $l=4.75$ and solving (6) and (7), the expressions for the density and pressure as a function of r are [14]:

$$\rho(r)=\frac{c^2}{8\pi G}\frac{1}{r^2}\left[1+\frac{\left(Ar^{2.25}+1.78\right)1.06C_1C_2r^{1.03}}{\left(2.359C_1+3.39C_2r^{1.03}\right)^2}+\frac{\left(3.25Ar^{2.25}-1.78\right)\left(C_1+C_2r^{1.03}\right)}{2.359C_1+3.39C_2r^{1.03}}\right] \quad (11)$$

$$p(r)=\frac{c^4}{8\pi G}\frac{1}{r^2}\left[\frac{\left(Ar^{2.25}+1.78\right)\left(1.359C_1+2.39C_2r^{1.03}\right)}{2.359C_1+3.39C_2r^{1.03}}-1\right]. \quad (12)$$

For e^{ν} to be strictly positive in the interior, we must have $C_1, C_2 \geq 0$ which imposes the following filtering condition on the parameter u, which varies from star to star due to its dependency on the star's mass and radius:

$$\frac{a+b-2}{a+b-1}\leq 2u\leq\frac{a-b-2}{a-b-1} \quad (13)$$

or, for $l=4.75$, $0.13325\leq u\leq 0.29079$. If the value of u for a particular star is not in this interval, it cannot be studied in the framework of the Pant model [14]. For $l=5$ one recovers [14] the Tolman IV [1] solution, which will be used as a reference in the computational calculations and the plots because of its elegant and very physically reasonable reults.

RESULTS AND DISCUSSION

We have studied the neutron stars KS1731-260 and EXO 1745 248 using the [13] and [14] models. In Table 1 we have listed their masses and radii, as well as checked the filtering condition (13) on the u parameter to see if they can be studied using the Pant model.

Table 1.

The considered stars, their masses and radii and the filtering condition for the Pant model

Name of star and source	M (M_Φ)	R (km)	Filter condition for Pant model	
			u	Verified?
KS1731-260 [15]	1.80	12.0	0.22	Yes
EXO 1745 248 [16]	1.40	11.0	0.19	Yes

We have obtained the density and pressure functions according to (9), (10) and (11), (12). In Figures 1 and 2 we have plotted the density functions of the [13] and [14] models, compared with the shape predicted by the Tolman IV solution [1]. Figure 2 is scaled at 1/4 in order to better see the slopes at low depth. In Table 2 we have listed the surface density for each star and each model and compare the results with the Tolman model. Unfortunately, to our knowledge, there are no

direct observational estimates of these quantities. The average densities (mass over volume) of KS1731-260 and EXO 1745 248 are $4.95*10^{17}$ kg/m^3 and $4.99*10^{17}$ kg/m^3 respectively.

Table 2.

The surface densities

Neutron star	**Surface Density (kg/m^3)**		
	Marcu & Ballai model	Pant model	Tolman IV
KS1731-260	$1.65*10^{17}$	$1.57*10^{17}$	$1.97*10^{17}$
EXO 1745 248	$1.66*10^{17}$	$1.63*10^{17}$	$2.13*10^{17}$

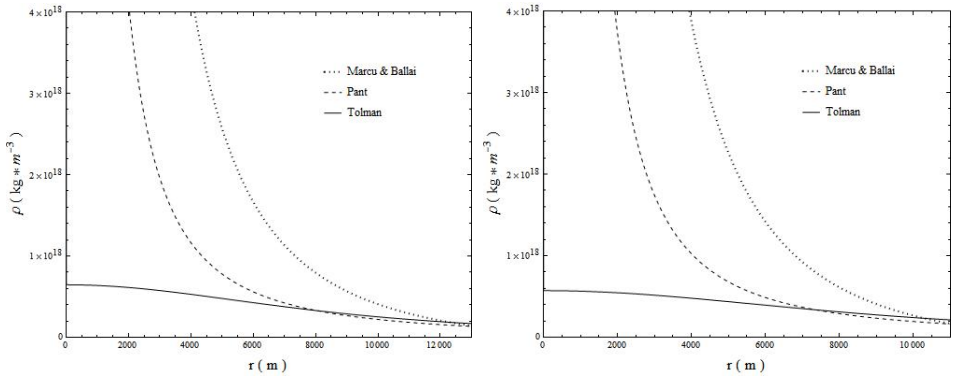

Fig. 1. Density in kg/m^3 as a function or r for KS1731-260 (left) and EXO 1745 248(right).

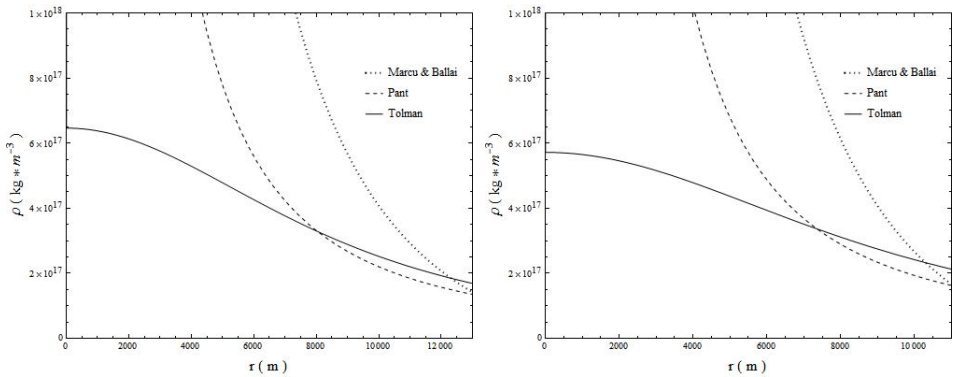

Fig. 2. Density in kg/m^3 as a function or r for KS1731-260 (left) and EXO 1745 248(right) at ¼ scale

In Figures 3 and 4 we have plotted the pressure functions at normal and 1/10 scale, respectively. We see that all three models are well behaved, in that the surface pressures are zero, in accordance to the assumption that the star is surrounded by vacuum.

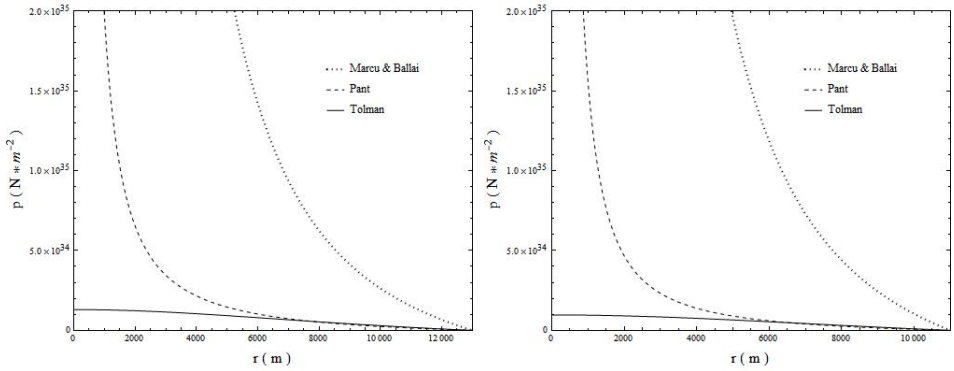

Fig. 3. Pressure in Pa as a function or r for KS1731-260 (left) and EXO 1745 248(right).

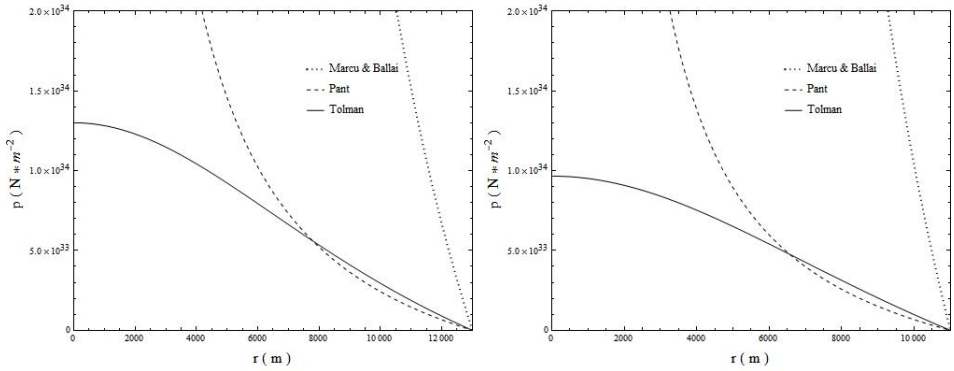

Fig. 4. Pressure in Pa as a function or r for KS1731-260 (left) and EXO 1745 248(right) at 1/10 scale

We have seen that the [13] model predicted a steeper rise of the density from the surface inwards than the one predicted by the Pant model. It is to be expected that the pressures will behave accordingly (steeper slope of pressure in the [13] model), and we have seen that this is the case.

We have then calculated and plotted the adiabatic sound speed as

$$v_s^2 = \frac{1}{c^2}\frac{dp}{d\rho} \quad \rightarrow \quad v_s = \frac{1}{c}\left(\frac{dp}{d\rho}\right)^{1/2}. \tag{14}$$

Figure 5 represents the adiabatic sound speed as a function of r, in units of *c* (the speed of light in vacuum) as obtained from (14). In all three models we have found the adiabatic sound speed to be everywhere smaller than *c*, as expected.

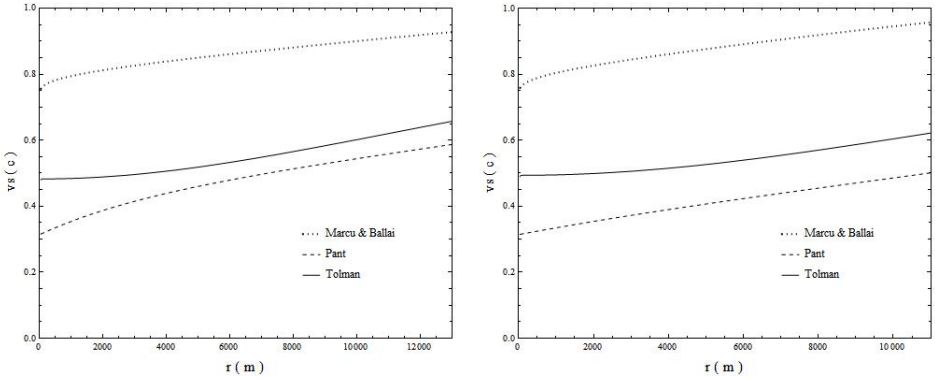

Fig. 5. Adiabatic sound speed in units of c as a function of r for KS1731-260 (left) and EXO 1745 248(right).

Afterwards, noting that this is the static case, we use a Poisson-type equation to calculate and plot the gravitational acceleration and potential. We also get the surface values for the gravitational acceleration and compare them with Tolman IV and the Newtonian case and list them in Table 3. The gravitational acceleration and potential, do not have tractable analytical expressions, so the plots were done numerically.

Table 2.

Surface gravitational acceleration

Neutron star	$\mathbf{g}_0 = -\frac{\mathbf{GM}}{\mathbf{R}_*}$ **(m/s^2)**	**Surface gravitational acceleration (m/s^2)**		
		Marcu & Ballai	Pant	Tolman
KS1731-260	-1.99*10^{16}	-3.22*10^{12}	-5.67*10^{13}	-4.74*10^{12}
EXO 1745 248	-1.69*10^{16}	-2.98*10^{12}	-2.58*10^{13}	-3.78*10^{12}

We note that there is a difference of 2-4 orders of magnitude between the results of Newtonian theory and those of GR. In Figure 6 we have plotted the gravitational accelerations according to the three models.

The negative values of the gravitational acceleration show that it points inwards, as expected. Also as expected, the Tolman reference is very well behaved However, due to the assumption of infinite central density, the [13] model goes to minus infinity at the center. Even more anomalous is the [14] model, in which the sign of the gravitational acceleration changes.

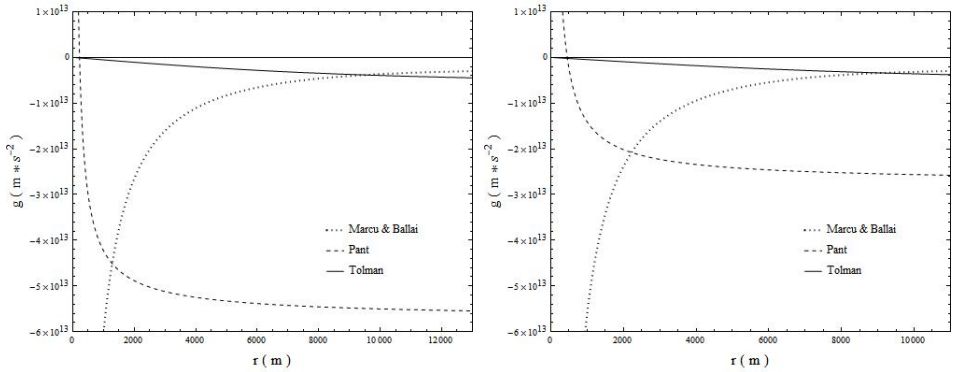

Fig. 6. Gravitational acceleration as a function of r for KS1731-260 (left) and EXO 1745 248(right).

The plots in Figure 7 represent the gravitational potential as a function of radius. The gravitational potential is zero in the center in all three models, because we have chosen the center of the star as the floor level, i.e. the bottom of the potential well. The abrupt slope of the Marcu & Ballai potential near the center is attributed to the presumption of infinite central density, but is not physically unreasonable. The Pant potential becomes negative in a region near the center of the star. The tempting conclusion is that if a particle should be able to travel through the (presumed) perfect fluid of the star, its position would stabilize inside a shell around the center. This is, however, the same anomaly as the one for the gravitational acceleration, and is also attributed to the mathematical assumption of infinite central density.

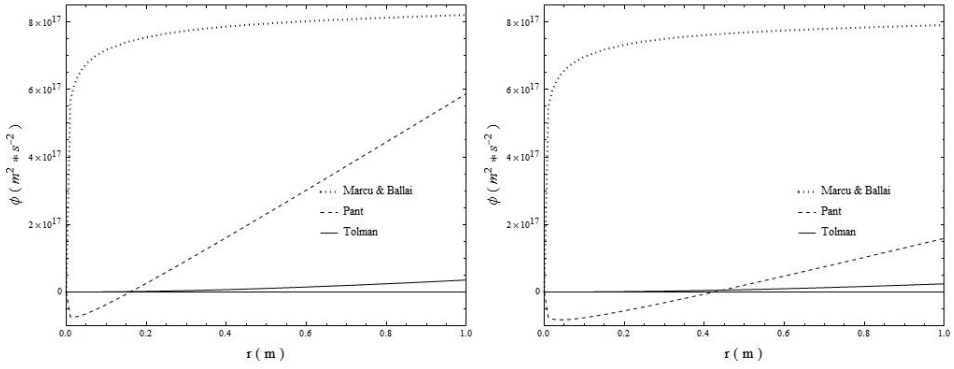

Fig 7. Gravitational potential as a function of radius for KS1731-260 (left) and EXO 1745 248(right).

CONCLUSIONS

We have applied the [13] and [14] models to study the interiors of the neutron stars KS1731-260 and EXO 1745 248. The central pressure and density singularities have led to anomalies in the gravitational acceleration and potential functions. The [13] model is more well-behaved in the interior region of the star in that the gravitational acceleration and potential do not change sign. Both models do, however, behave well in the exterior regions. To our knowledge, there are no direct observational estimates of the calculated quantities, the only possibility being to try to predict them using various models. The exact nature of the matter in the innermost regions of neutron stars is still unknown to science, so perhaps strange behaviors of the physics in those regions should not be totally ruled out. The adiabatic sound speed functions are also well behaved, as they are everywhere smaller than *c*.

ACKNOWLEDGEMENTS

This work is supported by a grant of the Romanian National Authority of Scientific Research, Program for Research - Space Technology and Advanced Research - STAR, project number 72/29.11.2013. Ş. Onțanu-Crăciun is partially supported by a Research Excellence scholarship for 2013-2014 of the Babeş-Bolyai University, Cluj-Napoca.

REFERENCES

[1]. R.C. Tolman, “Static solutions of Einstein’s field equations for spheres of fluid,” Physical Review, vol. 55, no. 4, p. 364 (1939).
[2]. M. Wyman, “Radially symmetric distributions of matter,” Physical Review, vol. 75, no. 12, p. 1930 (1949).
[3]. B. Kuchowicz, “General relativistic fluid spheres. I. New solutions for spherically symmetric matter distributions,” Acta Physica Polonica, vol. 33, p. 541, (1968).
[4]. D.N. Pant and A. Sah, “Class of solutions of Einstein’s field equations for static fluid spheres,” Physical Review D, vol. 26, no. 6, p.1254 (1982).
[5]. D.N. Pant and N. Pant, “A new class of exact solutions in general relativity representing perfect fluid balls,” J. Math. Phys., vol. 34, no. 6, p. 2440 (1993).
[6]. N. Pant, “Uniform radial motion of sound in a relativistic fluid ball,” Astrophysics and Space Science, vol. 240, no. 2, p. 187 (1996).
[7]. N. Pant, “Some new exact solutions with finite central parameters and uniform radial motion of sound,” Astr. and Sp. Science, vol. 331, no. 2, p. 633 (2011).

[8]. D.N. Pant, “Varieties of new classes of interior solutions in general relativity,” Astrophysics and Space Science, vol. 215, no. 11994 p. 97 (1994).
[9]. M.S.R. Delgaty and K. Lake, “Physical acceptability of isolated, static, spherically symmetric, perfect fluid solutions of Einstein’s equations,” Computer Physics Communications, vol. 115, no. 2-3, p. 395 (1998).
[10]. K. Lake, “All static spherically symmetric perfect-fluid solutions of Einstein’s equations,” Physical Review D, vol. 68, no. 10, (2003).
[11]. B.C. Tewari and M. Pant, “New parametric classes of exact solutions in general relativity and polytropic nature fluid ball with constant sound speed,” Astrophysics and Space Science, vol. 332, no. 2, p. 409 (2011).
[12]. S. K.Maurya and Y.K. Gupta, “A family of physically realizable perfect fluid spheres representing a quark–stars in general relativity,” Astrophysics and Space Science, vol. 337, issue 1, p. 151 (2012).
[13]. S. Ballai, Al. Marcu, “Some Exact Solutions of Charged Fluid Spheres in General Relativity”, Studia UBB, Physica, XXXIX, 2, p.91 (1994).
[14]. N. Pant, “Varieties of Pametric Classes of Exact Solutions in General Relativity Representing Static Fluid Balls”, ISRN Astronomy and Astrophysics, vol. 2011, id 749396, 2011.
[15]. F. Ozel, A. Gould, T. Guver, “The Mass and Radius of the Neutron Star in the Bulge Low-Mass X-ray Binary KS 1731-260”, ApJ, 748, p. 5 , (2012).
[16]. F. Ozel, T. Guver, D. Psaltis, “The Mass and Radius of the Neutron Star in EXO 1745-248“, ApJ, 693, p. 1775 (2009).

STUDIA UBB PHYSICA, Vol. 59 (LIX), 1, 2014, pp. 83-90
(RECOMMENDED CITATION)

STRUCTURAL AND MAGNETIC PROPERTIES OF THE $Mn_{50}Al_{46}Ni_4$ ALLOY

S. MICAN[a*], R. C. GAVREA[a], B. V. NEAMŢU[b], M. COLDEA[a] AND V. POP[a]

ABSTRACT. In this work the structural and magnetic properties of the $Mn_{50}Al_{46}Ni_4$ alloy were investigated. Differential Thermal Analysis (DTA) measurements pointed out the formation of the metastable τ phase around 480 ºC and its decomposition into the stable γ_2 and β-Mn(Al) phases at 850 ºC. X-ray Diffraction (XRD) investigations show that all of the samples are phase mixtures. The τ phase was found along with the ε' phase only in the as-cast sample and the ones annealed at 470°C, a fact which was confirmed by $M(T)$ measurements which showed two transitions at 445 K and 628 K, which correspond to the ferromagnetic ε' and τ phases, respectively. The samples annealed at 710 and 850 ºC showed a single magnetic phase behavior with lower Curie temperatures of 418 K (Al_2Mn_3) and 434 K (ε'-type phase) respectively. A maximum τ phase concentration of 43% was found for the sample annealed at 470 ºC for 5 h. The close values of the theoretical and experimental effective magnetic moments confirm the existence of the ε' and τ phases in these alloys.

Keywords: *Differential thermal analysis, Mn-Al alloys, annealing, crystal structure, magnetic properties.*

INTRODUCTION

Previous studies have shown that in the Mn-Al system a metastable phase (the tetragonal $L1_0$ or τ phase) with remarkable magnetic properties can be obtained, the most stable composition being $Mn_{54}Al_{46}$ [1-3]. It was also revealed that the disordered hexagonal closed-packed antiferromagnetic ε phase (T_N = 97 K) transforms to intermediate ordered orthorhombic ferromagnetic ε' phase (B19) at an elevated temperature, followed by the transformation of the ε' phase into the metastable

[a] *Babeş-Bolyai University, Faculty of Physics, 400084, Cluj-Napoca, Romania*
[b] *Technical University of Cluj-Napoca, Materials Science and Engineering Department, RO-400641, Cluj-Napoca, Romania*
* *Corresponding author e-mail: sever.mican@ubbcluj.ro*

ferromagnetic τ phase [4]. Electronic band structure calculations performed for $Mn_{50}Al_{50}$ pointed to an increase of the Mn magnetic moment from $\mu_{\varepsilon'} = 1.88\ \mu_B$ for the ε' phase to $\mu_\tau = 2.37\ \mu_B$ for the τ phase [4]. It has been noted that the addition of small percentages of carbon enhances the stability and saturation magnetization of the τ phase along with the magnetic moment of the Mn atoms [2]. However, the addition of carbon decreases both the Curie temperature and anisotropy field [5]. In the τ phase of the MnAl system, the Mn and Al atoms are situated in alternative planes at $c/2$ distances. In the case of the $Mn_{54}Al_{46}$ alloy 4% of the Mn atoms occupy the Al *2e* sites. The Mn atoms in the same plane are coupled ferromagnetically, but the magnetic interaction between the Mn atoms from adjacent planes is antiferromagnetic [1]. This leads to a decrease of the magnetization per formula unit [1]. For this composition, only 46% of Mn atoms contribute to the magnetization. In order to decrease the weight of this antiferromagnetic interaction to the magnetic characteristics of the MnAl system, we prepared the $Mn_{50}Al_{46}Ni_4$ alloy, taking into account that the Ni magnetic moment in different alloys and compounds is smaller than the one corresponding to Mn. Furthermore, in the metallic systems based on Ni and Al a partial filling of the Ni 3*d* band was observed due to the hybridization with the Al 3*sp* states [6], so that the antiferromagnetic interaction would be greatly reduced. The addition of Ni could also enhance the stability of the τ phase without a pronounced reduction of the Curie temperature. It is worth mentioning that in $Mn_{60-x}Al_{40}Ni_x$ thin films a maximum in both saturation magnetization and coercive field was obtained for Ni content around 5% [7].

EXPERIMENTAL DETAILS

The $Mn_{50}Al_{46}Ni_4$ ingot was prepared by induction melting of the starting components under a purified Ar atmosphere. High purity Mn (99.99 wt.%), Al (99.999 wt%) and Ni (99.99 wt.%) were used as starting materials. The sample was melted repeatedly in order to ensure homogeneity. The water-cooled sample holder ensured a rapid cooling of the alloy after melting. The weight loss of the final material was found to be less than 1 %. The samples were wrapped in tantalum foil, sealed in quartz tubes and annealed in an inert Ar atmosphere at temperatures between 470 and 850 ºC for different times. After annealing, the sealed samples were quenched in water. The crystalline structure of the alloys was analyzed at room temperature by using a Brüker D8 Advance diffractometer with Cu Kα radiation. Differential thermal analysis (DTA) was employed to study the structural transformations and phase transitions in the temperature range 100-900 ºC under Ar atmosphere with a temperature ramp rate of 20 ºC/min. The magnetization and magnetic susceptibility were measured with Weiss-type magnetic balance in a temperature range of 300-800 K.

RESULTS AND DISCUSSIONS

The DTA measurement for the as-cast $Mn_{50}Al_{46}Ni_4$ alloy is shown in Fig. 1. The DTA curve shows two endothermic peaks at 180 ºC and 350 ºC, which were identified as corresponding to the two ferromagnetic-paramagnetic transitions of the ε' (low T_c) and τ phases (high T_c), respectively [3, 4]. A low exothermal peak can be seen around 480 ºC, which can be attributed to the formation of the τ phase. The exothermal maximum at 720 ºC was identified as corresponding to the formation of the Al_2Mn_3 intermetallic compound, while the minimum at 850 ºC in the DTA curve denotes the decomposition of the alloy into the stable but nonmagnetic γ_2 (Al_8Mn_5) and β-Mn(Al) phases, in good agreement with the Mn-Al binary phase diagram [3].

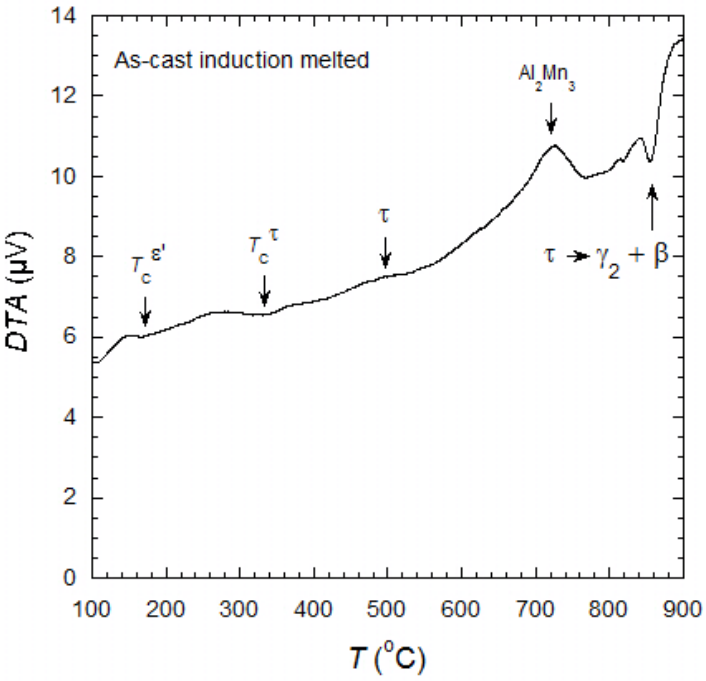

Fig. 1. DTA curve for the as-cast $Mn_{50}Al_{46}Ni_4$ alloy.

As a consequence of the DTA investigation, the thermal annealing of the as-cast sample was performed at different temperatures and for different annealing times. We chose to anneal the samples at 470, 720 and 850 ºC. The X-ray diffraction (XRD) patterns of the as-cast and annealed samples are shown in Fig. 2.

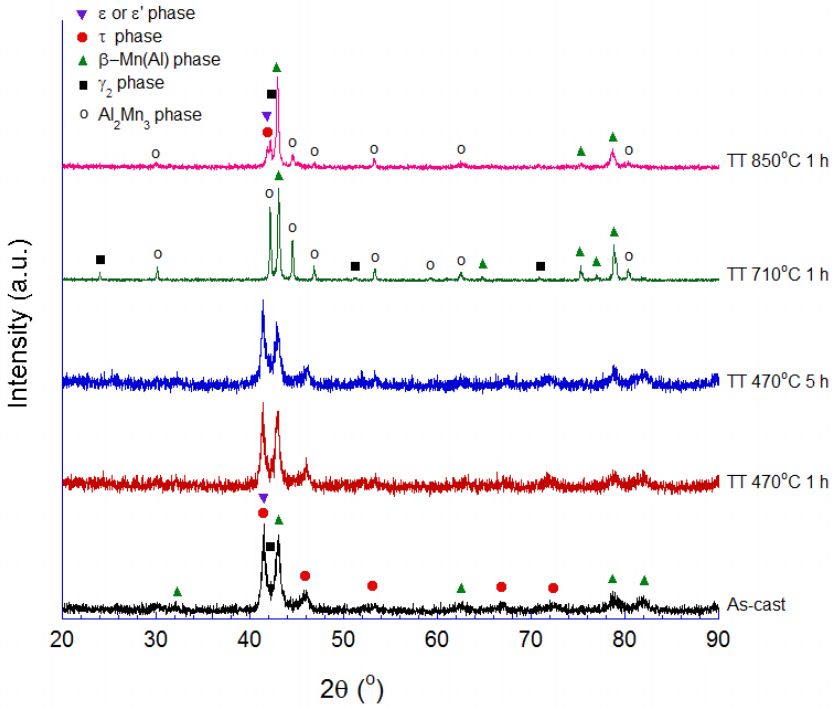

Fig. 2. XRD patterns for the $Mn_{50}Al_{46}Ni_4$ alloy after annealing at different temperatures.

The XRD pattern of the as-cast sample shows the presence of a mixture of phases, namely, the ferromagnetic τ phase, the ferromagnetic ε' phase (or antiferromagnetic ε phase) and the nonmagnetic β-Mn(Al) phase. Because the ε' phase is an ordered ε phase [3, 4], the XRD peaks of these two phases superimpose, making it impossible to discern between the two in the diffraction pattern. However, magnetic measurements (see Fig. 3) confirm the formation of the ε' phase in our samples, which leads us to believe that it is possible for just a small quantity of ε phase to be present in our compounds. Following annealing at 470 ºC for 1 h, there is no change compared to the as-cast sample, probably due to the low energy supplied to the sample during annealing. However, after annealing at 470 ºC for 5 h, we can see that the intensity of the XRD peaks corresponding to the β-Mn(Al) phase decreases, pointing to the formation of the τ phase. Annealing at 710 ºC for 1 h leads to the formation of the Al_2Mn_3 intermetallic compound, along with the minority β-Mn(Al) and γ_2 (Al_8Mn_5) phases. After annealing at 850 ºC we can see that the alloy decomposes into the β-Mn(Al), respectively Al_2Mn_3 and γ_2 phases. Also, the presence of the τ and ε' minority phases was also evidenced in this sample.

From the *M*(*T*) curves shown in Fig. 3 one observes the existence of two magnetic transitions at 445 K and 628 K for the as-cast sample, which correspond to the ferromagnetic ε′ and τ phases, respectively. The presence of the two magnetic phases is confirmed by the XRD patterns (Fig. 2). The same behavior was found for the samples annealed at 470 ºC for 1 and 5 h respectively. The τ phase represents only about 35% for the as-cast sample and the sample annealed at 470 ºC for 1 h, however for the sample annealed at 470 ºC for 5 h, the τ phase content increases to 43%.

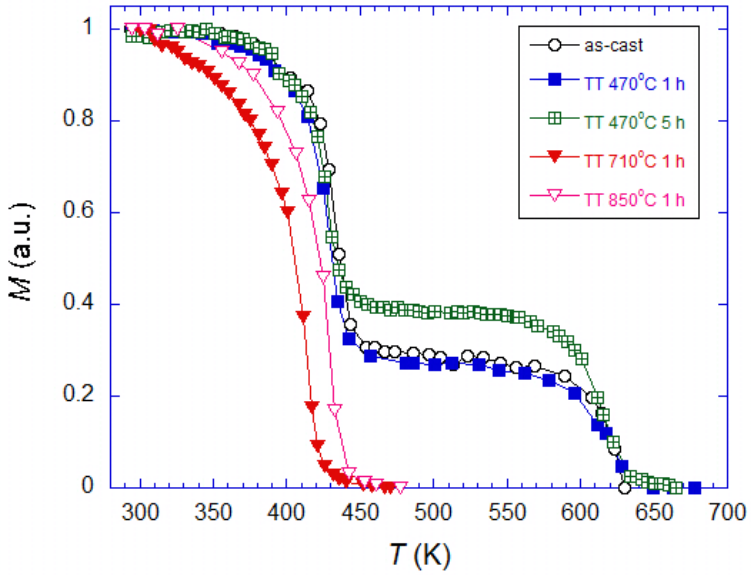

Fig. 3. Temperature dependence of the magnetizations (relative values) of the $Mn_{50}Al_{46}Ni_4$ alloy after annealing at different temperatures.

This confirms the fact that the τ phase starts to form at this temperature, in agreement with DTA measurements. The samples annealed at 710 ºC and 850 ºC for 1 h show a single magnetic phase behavior. For the sample annealed at 710 ºC, the transition occurring at 418 K corresponds to the Al_2Mn_3 intermetallic compound. The transition at 434 K found in the sample annealed at 850 ºC could be attributed to an ε'-type phase. This behavior is in agreement with the XRD investigations.

The temperature dependences of the reciprocal susceptibility for the as-cast $Mn_{50}Al_{46}Ni_4$ alloy and for the sample obtained after annealing of this alloy at 470 ºC for 5 h are shown in Fig. 4.

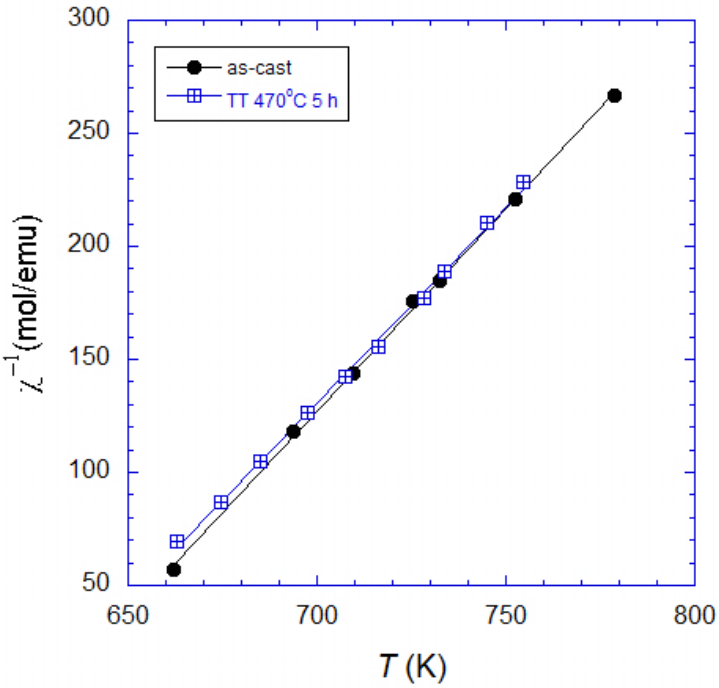

Fig. 4. Reciprocal susceptibility versus temperature curves of the $Mn_{50}Al_{46}Ni_4$ alloy. The lines represent the Curie-Weiss fit of the experimental data.

The experimental data fits the Curie-Weiss law $\chi=C/(T-\theta)$ with the parameters given in Table 1. The average experimental Mn moment in the ordered state was calculated taking into account the concentrations $c_{\varepsilon'}$ and c_τ of the ε' and τ phases and the theoretical values of Mn moments in the two phases [4], according to the relation $\mu_{exp} = c_{\varepsilon'}\,\mu_{\varepsilon'} + c_\tau\mu_\tau$. Close values of the μ_{teor} and μ_{exp} values confirm the existence of the ε' and τ phases in the investigated $Mn_{50}Al_{46}Ni_4$ alloy. So far, the maximum obtained τ phase content represents only 43% of the whole sample. Ongoing experimental work is currently being conducted to obtain, through adequate thermal treatments, the τ phase as a majority phase and to determine its main magnetic characteristics.

Table 1.

The effective magnetic moments μ_{eff}, the spins *S,* of the Mn atoms, the τ phase content c_τ, the average theoretical and experimental Mn moments in the ordered state μ_{teor} and μ_{exp}, the paramagnetic Curie temperatures θ, and the Curie temperatures T_C, of the τ phase of the $Mn_{50}Al_{46}Ni_4$ alloy.

Sample	μ_{eff}/f.u (μ_B)	μ_{eff} /Mn (μ_B)	S_{Mn}	c_τ (%)	μ_{teor} (μ_B)	μ_{exp} (μ_B)	θ (K)	T_C (K)
As-cast $Mn_{50}Al_{46}Ni_4$	2.11	2.98	1.07	35	2.14	2.06	629	624
$Mn_{50}Al_{46}Ni_4$ annealed at 470 ºC for 5 h	2.15	3.04	1.1	43	2.2	2.09	624	635

CONCLUSIONS

The structural and magnetic properties of the $Mn_{50}Al_{46}Ni_4$ alloy were investigated. DTA investigations pointed to the formation of the τ phase around 480 ºC and its decomposition at 850 ºC, in agreement with the Mn-Al binary phase diagram. XRD investigations have shown that all of the samples are phase mixtures. All of the samples were ferromagnetic at room temperature. The τ phase was found along with the ε' phase only in the as-cast sample and the ones annealed at 470°C. This is also confirmed by thermomagnetic measurements, which showed two magnetic transitions at 445 K and 628 K corresponding to the ferromagnetic ε′ and τ phases, respectively. The τ phase concentration was found to be around 35% for the as-cast sample, however this value increased to 43% after annealing at 470 ºC for 5 h. The samples annealed at 710 and 750 ºC showed a single magnetic phase behavior with lower Curie temperatures of 418 K and 434 K, which were attributed to the Al_2Mn_3 phase and an ε'-type phase respectively. The close values of the experimental and theoretical Mn magnetic moments in the ordered magnetic state confirm the presence of the ε′ and τ phases in the investigated $Mn_{50}Al_{46}Ni_4$ alloy. The maximum obtained τ phase concentration was 43%, however, ongoing experimental work is currently being conducted to obtain the τ phase as a majority phase in these compounds.

ACKNOWLEDGEMENTS

This work was supported by the Romanian Ministry of Education and Research, Grant PN-II-ID-PCE-2012-4-0470, No. 73/2.09.2013.

REFERENCES

[1]. H. Kono, *J. Phys. Soc. Jpn.*, 13, 1444-1451 (1958).
[2]. A. Sakuma, *J. Phys. Soc. Jpn.*, 63, 1422-1428 (1994).
[3]. T.E. Prost, " PhD Thesis: Magnetic Properties Study of the Mn-Al System with Additions of B or C and Mechanical Milling Techniques", University of Nebraska – Lincoln, 2012.
[4]. J.H. Park, Y.K. Hong, S. Bae, J.J. Lee, J. Jalli, G.S. Abo, N. Neveu, S.G. Kim, C.J. Choi, J.G. Lee, *J. Appl. Phys.*, 107, 09A731 (2010).
[5]. Z.W. Liu, C. Chen, Z.G. Zheng, B.H. Tan, R.V. Ramanujan, *J. Mat. Sci.,* 47, 2333-2338 (2012).
[6]. V. Rednic, M. Coldea, S.K. Mendiratta, V. Pop, M. Neumann, L. Rednic, *J. Magn. Magn. Mater.,* 321, 3415 (2009).
[7]. M. Matsumoto, A. Morisako, J. Ohshima, *J. Appl. Phys.,* 69, 5172-5174 (1991).

STUDIA UBB PHYSICA, Vol. 59 (LIX), 1, 2014, pp. 91-97
(RECOMMENDED CITATION)

MEASUREMENT OF THERMAL NEUTRON CROSS-SECTION FOR THE ^{174}Yb(n, γ)^{175}Yb NUCLEAR REACTION BY USING ISOTOPIC NEUTRON SOURCE

GHEORGHIEŞ OANA[a], LIVIU DĂRĂBAN[a*]

ABSTRACT. In this work, we produced radioisotopes by the nuclear reaction ^{174}Yb(n,γ)^{175}Yb, using neutron facilities with isotopic neutron sources. The thermal neutron cross-section for the reaction ^{174}Yb(n, γ)^{175}Yb reaction was measured using the activation method with ^{56}Mn as a monitor. ^{174}Yb was one of the investigated isotopes in order to clarify the differences between the values of the effective cross-sections for this reaction determinate by different authors.

Keywords: *resonance neutrons, cross sections, isotopic neutron sources*

1. INTRODUCTION

For a quantitative description of neutron reactions the thermal neutron cross-section is used. It will be considered a parallel neutron flux density of incident particles by intensity I_0, which cross perpendicular to a thin layer of material, with thickness dx and surface S, which has n identical nuclei in unit volume. We assumed that the nucleus considered as a scattering center has a effective area σ, in which if a particle beam get there occurs a process of interaction, as a result of which it is removed from the stream by absorption or the changing direction of the motion. The cross-section has the dimensions of an area and the unit of measurement is 10^{-24} cm^2 = 1 barn (1 b).[1] The neutron isotopic sources having a constant neutron flux density were used to determine the effective electron temperature in cross section of various nuclear reactions as in articles [1-3]. The knowledge about the effective thermal neutron cross-section and resonance integral of ^{174}Yb has great a importance for studies on interactions of neutrons with materials and other fundamental research, as

[a] *Babeş-Bolyai University, Faculty of Physics, 1 Kogălniceanu str., 400084 Cluj-Napoca, Romania*
* *Corresponding author: liviu.daraban@phys.ubbcluj.ro*

well as for producing therapeutic radioisotopes such as ^{175}Yb via the neutron activation method. Of all this we have dealt with the nuclear reaction ^{174}Yb(n, γ)^{175}Yb in agreement with the article [1] to determine a value of σ = 126,5 ± 6,6 b relative to a monitor ^{55}Mn.

2. EXPERIMENTAL

2.1. Neutron irradiation facility

The neutron facility contains two isotopic neutron sources of ^{241}Am-^{9}Be and ^{239}Pu-^{9}Be type generating a neutron flounce of $6{,}6 \cdot 10^{7}$ n/s. The paraffin block slows down the neutrons through the multiple collisions with hydrogen atoms. The irradiation channels are placed at 3,5 cm from the central channel containing the two sources (Fig.1). The 3,5 cm thickness of paraffin is optimal for the neutron moderation for point sources, established to test cadmium.

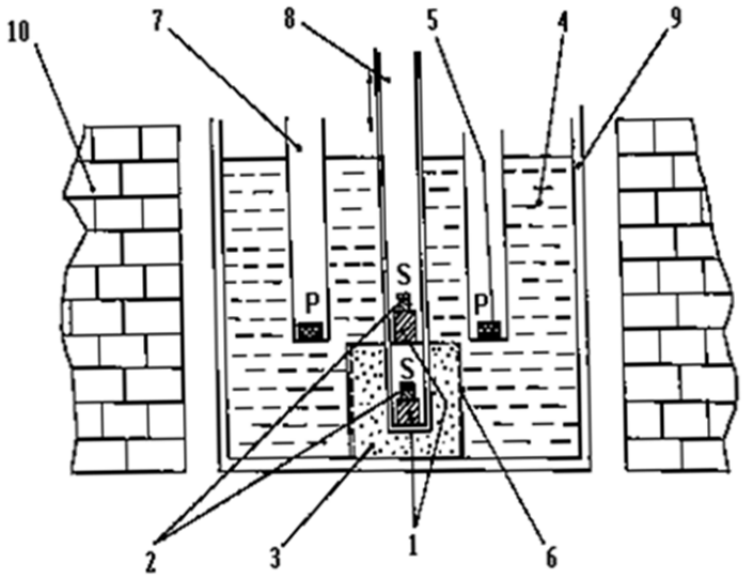

Fig. 1. The irradiation block containing the Am-Be and Pu-Be neutron sources. 1) Am-Be source, 2) Pu-Be source, 3) Borate paraffin, 4) Pure paraffin for the thermalisation, 5) Sample for irradiation, 6) Cd protection, 7) Channel for irradiation, 8) Central channel for irradiation with fast neutron, 9) Fe-walls of paraffin ensemble, 10) Borated paraffin bricks for protection.

2.2. Samples preparation

We have prepared two types of cylindrical samples for irradiation: Yb_2O_3 with mass m = 0,1665 g, which is the sample studied, a sample of MnO_2 flow monitor with standard mass of 0,174 g and a box of cadmium to be able to do differential measurements using cadmium ratio method. It is known that a leaf of cadmium with thickness of 1 mm can absorb 10^6 neutrons/s with energy E_n< 0,4 eV. That is why all our measurements were twin: a sample without Cd cover irradiated by the total number of neutrons, of all energies (after steaming through the 3,5 cm paraffin, 60% are below 0,4 eV). And the second irradiation sample with Cd-box which means it is irradiated with thermal and epithermal neutrons passing through Cd sample, so the energy is E_n> 0,4 eV.

3. THERMAL NEUTRON CROSS-SECTION DETERMINATION

Irradiation have been made 30 days, one by one each sample without the Cd and then with Cd, knowing that the neutron flow is absolutely steady. Unknowing the neutron flux density was used the method of Mn comparator at neutron cross-section determination.

3.1. Efficiency calibration of the analyzer

For gamma activity acquisition we used a spectrometer with a semiconductor detector type HPGe Canberra, running at 3,5 kV, equipped with a multichannel analyser with 4096 channels and a Genie 2000 software. The detector is surrounded by a shield of lead NZ type 138, designed to stop the environmental range to photons reaching the detector, so that the low activity of radionuclides can be measured [4,10].

The energy efficiency of the installation for gamma spectrometry was determined according to the methodology described in the work of Lavi and Alfassi [9], by using a calibration source prepared in the laboratory, made from ThO_2 in secular equilibrium with its daughter radionuclides, (Fig.1) with an absolute activity of 1087.4 Bq.

This is a procedure used by HPGe detector type Canberra GC1519 which establishing links between the radiation energy range and number of channels. After identifying the energies using standard sources, efficiency value is calculated taking into account the probability of each decay energy. This value is needed for the calibration of detector efficiency, as in the following formula [4]:

$$\varepsilon = \frac{N}{(\varepsilon_g \cdot t \cdot \Lambda \cdot p)} \quad (1)$$

where *N*- is the peak area, *t* – is the acquisition time of the spectrum, *Λ*- is the absolut activity of the calibration source and ε_g is the geometrical efficiency, and *p* is the probability.

The efficiency is calculated from each peak area, from gamma spectrum presented in Fig. 2. The curve of efficiency is in agreement with [4] and the other cases of works for this type of detector.

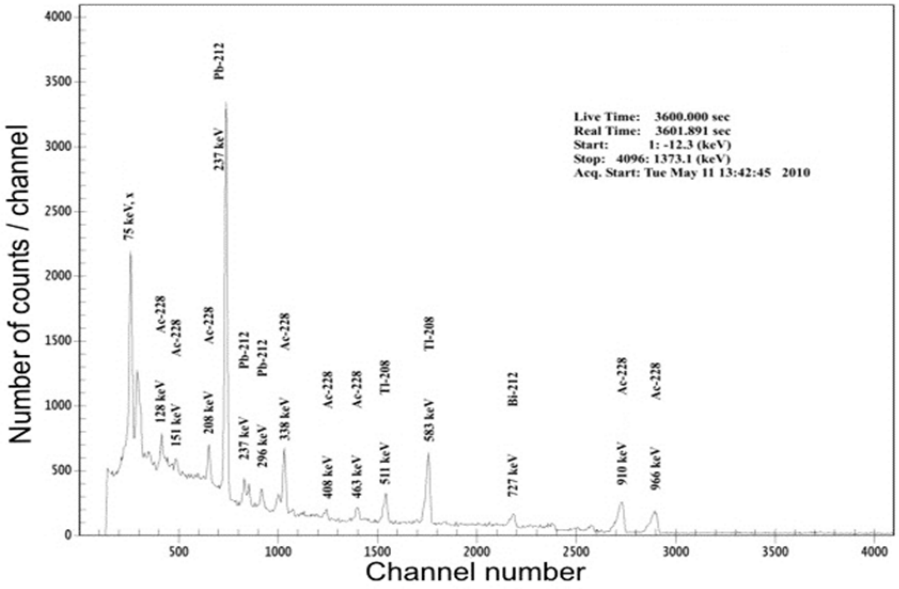

Fig. 2. The gamma calibration spectra with ThO_2

3.2. Neutron cross section determination

The thermal neutron cross-section for the reaction $^{174}Yb(n, \gamma)^{175}Yb$ has been determined relative to that for the ^{55}Mn (n, γ)^{56}Mn reaction. The thermal neutron cross section $\sigma_{0,x}$ for an (n, γ) reaction being investigated is calculated as [1]:

$$\sigma_{0,x}\sigma_{0,s} = [\sigma_{0,s}] \cdot \left[\frac{r_x - r_{Cd,x}/F_{Cd,x}}{r_s - r_{Cd,s}/F_{Cd,s}}\right] \cdot \left(\frac{G_{th,s}}{G_{th,x}}\right) \cdot \left(\frac{g_s}{g_x}\right) \quad (2)$$

where x index denotes the ^{174}Yb(n, γ)^{175}Yb reaction being investigated and s denotes the ^{55}Mn (n, , γ)^{56}Mn monitor reaction. σ_0 is thermal neutron cross-section and F_{Cd} is the cadmium transmission correction factor for epithermal neutrons. G_{th} is the thermal neutron self-shielding factor. According with [1] paper the reaction rates, *r* and r_{Cd} are determined by:

$$r = \frac{A_{sp}^{-} \cdot F_g \cdot M}{\theta \cdot N_A \cdot \gamma \cdot \varepsilon_p} \quad \text{and} \quad r_{Cd} = \frac{A_{sp}^{+} \cdot F_g \cdot M}{\theta \cdot N_A \cdot \gamma \cdot \varepsilon_p} \tag{3}$$

with $$A_{sp}^{-} = \left[\frac{N_p/t_c}{w \cdot S \cdot D \cdot C}\right]_{bare} \text{ and } A_{sp}^{+} = \left[\frac{N_p/t_c}{w \cdot S \cdot D \cdot C}\right]_{Cd}$$

where A_{sp}^{-} and A_{sp}^{+} are specific activities obtained after a bare and Cd covered isotope irradiation, N_p is net number of counts under the full-energy peak collected during measuring live time, t_c, w is weight of irradiated element, $S = 1 - e^{-\lambda t_{irr}}$ is saturation factor with being the decay constant, λ and irradiation time, t_{irr}. $D = e^{-\lambda t_d}$ is decay factor with being the decay time, t_d, and $C = \frac{1-e^{-\lambda t_r}}{\lambda t_r}$ is the measurement factor correcting for decay during the measuring true (real) time, t_r. M is atomic weight,θ is isotopic abundance, N_A is Avogadro's number, λ is absolute gamma-ray emission probability, ε_p is full-energy peak detection efficiency for measured γ-ray energy, and F_g is correction factor for gamma ray attenuation done in [3].

After each radiation the samples were measured with a high-resolution gamma spectrometer. The gamma spectrum of ^{56}Mn and ^{175}Yb obtained by activation are shown in the following figures (Fig.3 and 4).

We read every spectrum the peak area.

Table 1.

Peak area for different energies of ^{175}Yb and ^{56}Mn

No.	E (keV)	Isotope	A (peak area)	Detector efficiency (%)	The probability desintegrations (%)	Neutron cross-section σ (b)
1	114,2	^{175}Yb	9561	40	1.88	146
1*	844,8	^{56}Mn	5972	4.57	99	13.2

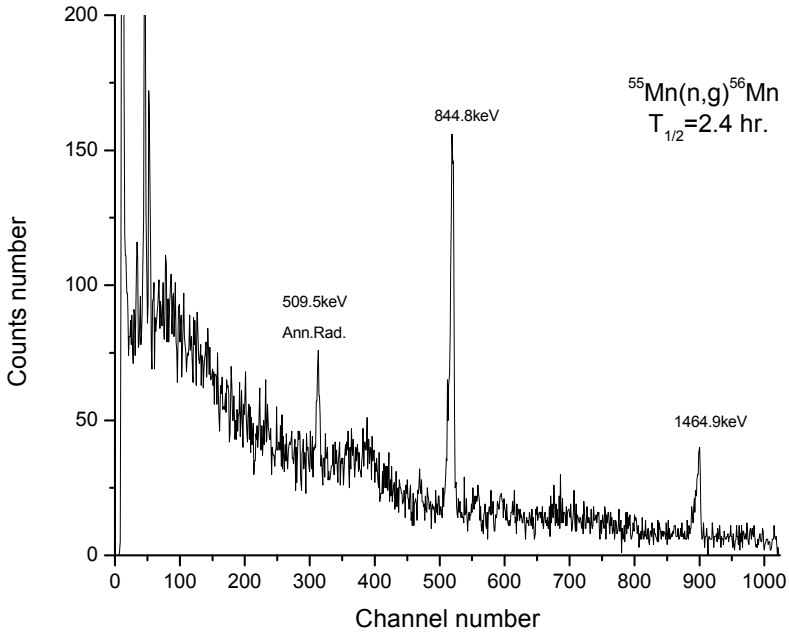

Fig. 3. Gamma spectrum of ^{56}Mn used as monitor

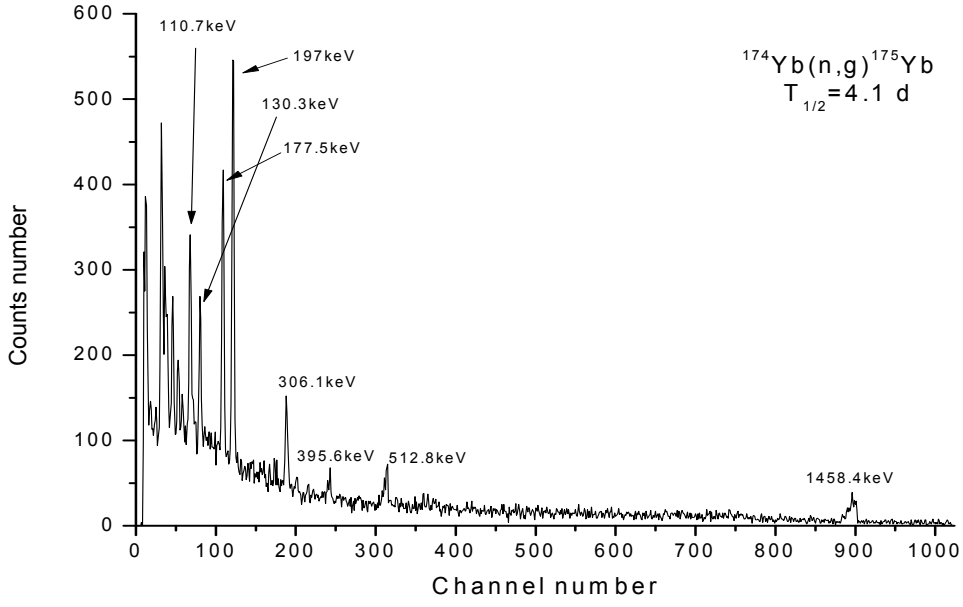

Fig. 4. Gamma spectrum of ^{175}Yb radioisotope

In conclusion performing calculations with formula (2) for these peaks we obtain σ = 146 barns the cross section for ^{174}Yb(n,γ)^{175}Yb reaction. Our value is in good agreement compared to that of other authors, and we find a good consistent with each other according to table 4 of [1] paper.

REFERENCES

[1] Mustafa Karadag, Haluk Yucel, *Measurement of thermal neutron cross-section and resonance integral for the ^{174}Yb(n,γ)^{175}Yb reaction by the cadmium ratio method*, Nuclear Instruments and Methods in Physics Research B 266 2549–2555, (2008).

[2] Nguyen Van Do, Pham Duc Khue, Kim Tien Thanh, Le Truong Son, Guinyun Kim, Young Seok Lee, Youngdo Oh, Hee-Seok Lee, Moo-Hyun Cho, In Soo Ko, Won Namkung, *Thermal neutron cross-section and resonance integral of the ^{186}W(n,γ)^{187}W reaction*, Nuclear Instruments and Methods in Physics Research B vol. 266, pp.863-871,(2008).

[3] M.S. Uddin, M.H. Chowdhury, S.M. Hossain, Sk.A. Latif, M.A. Islam, M.A. Hafiz, S.H. Mubin, A.K.M. Zakaria, S.M. Yunus, S.M. Azharul Islam, *Thermal neutron capture cross sections for the ^{152}Sm(n,γ)^{153}Sm and ^{154}Sm(n,γ)^{155}Sm reactions at 0.0536 eV energy*, Nuclear Instruments and Methods in Physics Research B 266 4855–4861,(2008).

[4] B. Biro, L. Dărăban, V. Simon, *Monitoring of Thermal Neutron Flux of Isotopic Sources by Activation Method*, Studia UBB Physica, Vol. 58 (LVIII), 1, pp. 5-12, (2013).

[5] Haluk Yucel, M. GuraynBudak, Mustafa Karadag, *Measurement of thermal neutron cross section and resonance integral for the^{170}Er(n, γ)^{171}Er reaction by using a ^{55}Mn monitor*, Physical Review C76, 034610 (2007).

[6] Mustafa Karadaga, Haluk Yucel, *Thermal neutron cross-section and resonance integral for ^{164}Dy(n,γ)^{165}Dy reaction*, Nuclear Instruments and Methods in Physics Research A 550 626–636,(2005).

[7] Nguyen Van Do, Pham Duc Khue, Kim Tien Thanh, Bui Van Loat, Md.S. Rahman, Kyung Sook Kim, Guinyun Kim, Youngdo Oh, Hee-Seok Lee, Moo-Hyun Cho, In Soo Ko, Won Namkung, *Thermal neutron cross-section and resonance integral of the ^{98}Mo(n,γ)^{99}Mo reaction*, Nuclear Instruments and Methods in Physics Research B 267 462–468, (2009).

[8] M.G. Budak,H. Yucel, M. Karadag, M. Tan, *Experimental determination of effective resonance energies for the (n,γ) reactions of ^{71}Ga, ^{75}As, ^{164}Dy*, Annals of Nuclear Energy 35 1433–1439, (2008).

[9] N. Lavi, Z.B. Alfassi, Appl. Radiat. Isotopes 61, 1437–1441 (2004).

[10] Mustafa Karadaga, Haluk Yucel, Mustafa Tan, Atilla Ozmen, *Measurement of thermal neutron cross-sections and resonance integrals for ^{71}Ga(n,γ)^{72}Ga and ^{75}As(n,γ)^{76}As by using ^{241}Am-Be isotopic neutron source*, Nuclear Instruments and Methods in Physics Research A 501 524-535,(2003).